Sediment Dynamics in Shallow-Bay Ship Channels

Final Report

Prepared by

Jens Figlus and Joshua Joubert

Department of Ocean Engineering, Texas A&M University / TEES

Tim Dellapenna, Scott Sudduth, Nicholas Wellbrock, Nathalie Jung, and Richard Schenk

Department of Marine and Coastal Environmental Science, Texas A&M University at Galveston

Prepared for

U. S. Army Corps of Engineers – Galveston District (SWG) with funding provided under Cooperative Ecosystem Studies Unit (CESU) agreement No. W912HZ-17-2-0023 to Texas A&M Engineering Experiment Station (TEES)

August 2022

Table of Contents

Table of Figures

Table of Tables

Acknowledgements

This work was supported by the U. S. Army Corps of Engineers – Galveston District (SWG) with funding provided under Cooperative Ecosystem Studies Unit (CESU) agreement No. W912HZ-17-2-0023 to Texas A&M Engineering Experiment Station (TEES). The authors would like to thank Patrick Kerr (USACE SWG), Coraggio Maglio (USACE SWG), Michael Ritz (USACE SWG), Paul Hamilton (USACE SWG), Jennifer McAlpin (USACE ERDC), Lori Brownell (Houston Port Authority), and Richard Ruchhoeft (Houston Port Authority) for their support, guidance, and feedback throughout the course of the study.

1 Introduction

This report details TAMU/TEES deliverables related to the project entitled: “Sediment dynamics in shallow-bay ship channels”. This project is a task under Coastal Ecosystem Studies Unit (CESU) agreement No. W912HZ-17-2-0023 between the U.S. Army Corps of Engineers (USACE) and Texas A&M Engineering Experiment Station (TEES) entitled “In-Situ Measurements of Physical Forces and Biological Parameters in Coastal and Estuarine Systems, Galveston District”. The TAMU/TEES tasks that are part of this project include a data gap analysis, field data collection, and sediment trend analysis for a portion of Galveston Bay containing the Houston Ship Channel (HSC) and adjacent Bayport Ship Channel (BSC) to help assess the problem of heightened sedimentation at the Bayport Flare and provide background information to aid the design of mitigation measures to limit these shoaling issues.

1.1 Background and Motivation

The HSC is one of the busiest waterways in the United States (U.S.) with over 9,000 deep-draft and 200,000 barge transits per year in segments 1-6 (Figure 1-1). The U.S. Coast Guard Port and Waterway Safety Assessment (PAWSA) assigned the HSC the highest baseline risk level for economic loss and assigned an unacceptable baseline risk for HSC’s channel dimension and configuration, safety, potential for discharges, and volume of ship traffic. Existing channel depths, widths, and configurations cause inefficiencies for shallow and deep-draft vessels. Average vessel size and traffic volume at the HSC continue to increase, leading to thousands of hours of delays for vessels transiting the HSC. With projected increases in trade volume and vessel size, more delays can be expected.

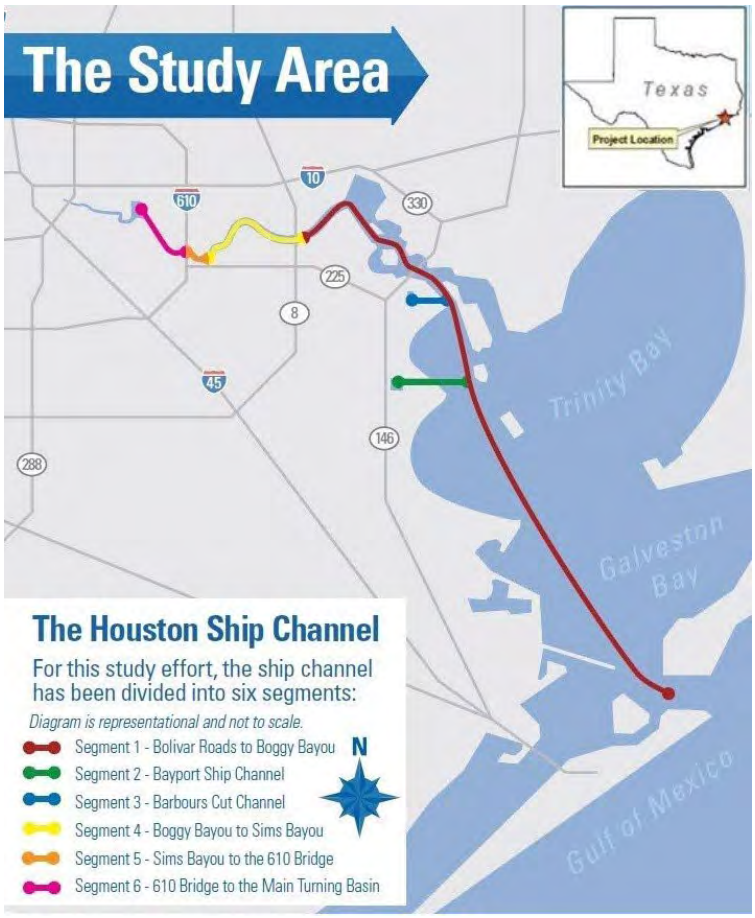

Figure 1-1: Map of the Houston Ship Channel (HSC) split up into six segments. Segment 2 is the Bayport Ship Channel (BSC). Source: USACE.

SWG is responsible for coastal infrastructure and navigation projects along the entire Texas coast, including 700 miles of coastline and 1,000 miles of channels, of which 270 miles are deep-draft. The USACE developed a dredged material management plan (DMMP) detailing placement of dredged material from the HSC. Placement opportunities that were evaluated included a suite of upland confined placement areas (PA), beneficial use (BU) sites, and offshore placement at the existing Ocean Dredged Material Disposal Site (ODMDS No. 1). Figure 2 gives an overview of existing and proposed PA/BU sites. The limited capacity of existing environmentally acceptable dredged material placement area and beneficial use sites (PA/BU) is a problem requiring immediate attention. Current PA/BU capacity is insufficient for future needs of the system (segments 1-6). Extensive shoaling in various ship channel segments (i.e., HSC, BSC, BBC) is a major concern to be addressed as this further exacerbates the problem of limited PA/BU capacity for future O&M requirements.

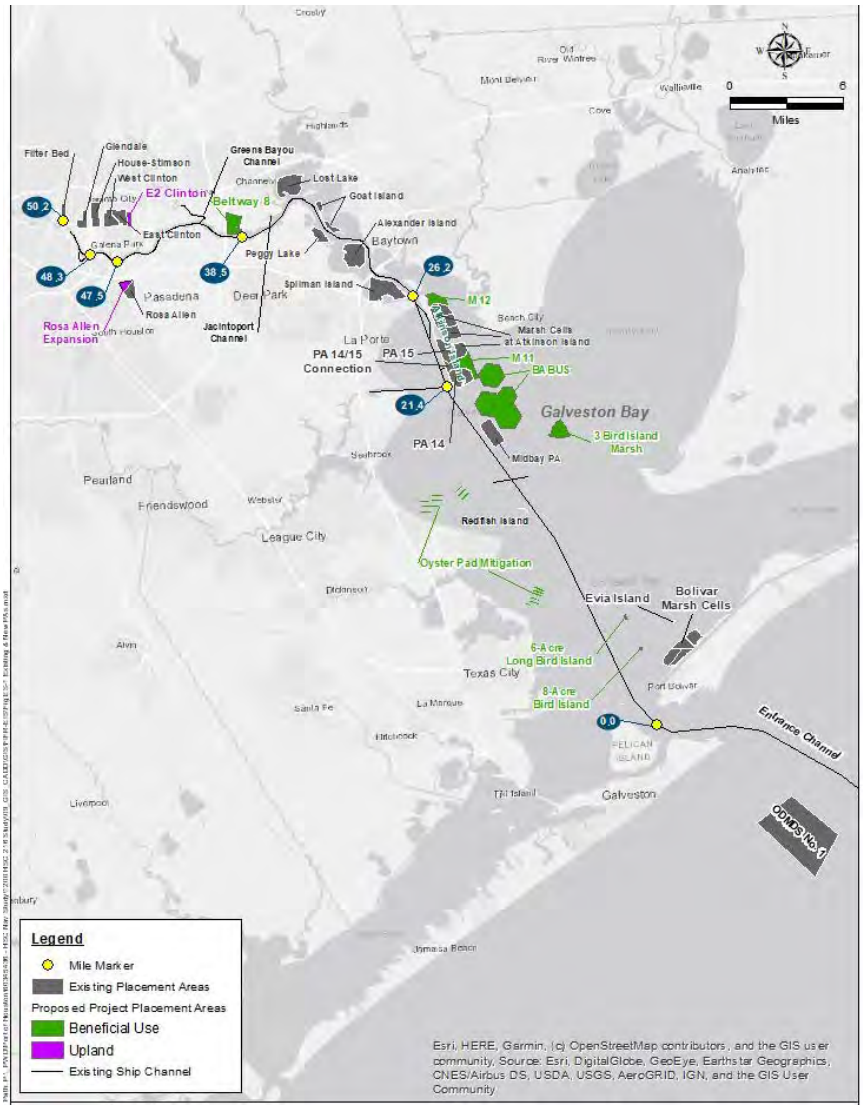

Figure 1-2: Existing and proposed placement locations for the HSC system. Source: USACE.

Historical dredging records indicate the Bayport Flare is a major sink; it is a large, deep area where the velocity drops sufficiently for material to settle. The fundamental problem leading to the shoaling is believed to be the broad circulation pattern combined with the large amount of traffic in the reach. Sediments are continuously suspended by passing ships, and then carried with the circulating currents until they settle in the relatively quiescent deep sections, the depths of which are subsequently maintained by dredging.

Other processes may contribute to the high episodic shoaling near the flares of the BSC and the BBC channel, and in the HSC between the BSC and the Midbay placement area. These may include

wind wave driven movement of sediment, salinity wedge transitions, turbidity maxima, density currents, shoreline or channel slope erosion from ship wakes and prop wash, channel geometry changes, or other yet to be identified causes.

Numerical model simulations of hydrodynamics and sediment transport are necessary to better understand the shoaling processes and optimize the design of potential shoaling attenuation structures. The data collection outlined in this report is intended to provide background information to validate numerical modeling efforts and aid in decision making related to potential mitigation design options. Field data of currents, waves, water levels, salinity, bed properties, suspended sediment, and sediment movement in the project area are critical in calibrating numerical model simulations needed to investigate design alternatives.

1.2 Objectives and task overview

The objective of this effort is to study the causes of chronic and episodic shoaling near the flares of the Bayport and Barbour's Cut ship channels (BSC & BBC), and in the Houston Ship Channel primarily focused between the Barbour's Cut and Red Fish Island by means of a comprehensive field data collection effort.

Figure 1-3 gives an approximate outline of the proposed shoaling study area, but vessel-borne measurements outside of the framed area at critical numerical model boundary locations where major watershed contributions enter Galveston Bay (i.e., Clear Creek / Clear Lake, Dickinson Bayou, Lower San Jacinto River, Trinity River, and Cedar Bayou) were also conducted. In-situ data collection is intended to gain a better understanding of the composition, size distribution, and dynamics of bed and suspended sediments, as well as to characterize hydrodynamic conditions and salinity variations driving sediment transport. Prior to in-situ data collection, a data gap analysis was performed to identify available and useful historic information on bed sediment, suspended sediment, salinity, and hydrodynamics (waves, currents, water levels) in the project area.

Figure 1-3: Approximate outline of proposed shoaling study area. Source: USACE.

The tasks included in the scope of work are as follows:

1. Data gap analysis to identify existing relevant data on sediment characteristics and movement as well as hydrodynamic and salinity conditions in the project area that can inform numerical modeling and mitigation design efforts.
2. Bed sediment data collection and analysis in the project area.
3. Suspended sediment concentration measurements and analysis.
4. Collection and analysis of hydrodynamic data on waves, currents, and water levels as well as salinity and temperature (CTD) data relevant to the project area.
5. Sediment trend analysis (STA) based on available and collected data to empirically determine sediment transport pathways in the project area.

The collected data and deliverables associated with the above tasks are detailed in the following report sections.

2 Data Gap Analysis

A summary of existing hydrodynamic (water level, wave, and current information), salinity, and sediment-related data (grab samples, cores, suspended concentration measurements) relevant to the project area is provided in this section. This includes existing data sets from Galveston Bay as well as existing information on sediment sources from tributaries. These data sources are listed in the following subsections.

2.1 Historic surface sediment data

Several sources of surface sediment data were located and include information from grab samples and cores collected in previous research efforts.

Dellapenna Lab (TAMUG)

Dellapena et al. (2006) report on one core collected in Trinity Bay in 1999 by Mead Allison but no grain size data were analyzed as part of that study. Figure 2-1 shows the location of the core sample. In addition, Dellapenna et al. (2021; 2020) and Du et al. (2019) collected post Hurricane Harvey (2017) cores as detailed in a later section on the current sediment sampling efforts where the same locations were sampled again.

John Anderson Lab (Rice University)

The only cores shown from John Anderson's work in Galveston Bay are 4 borings collected around 2002. They include grain size distributions at the surface. All results are documented by Rodriguez et al. (2005). The right panel in Figure 2-1 shows the locations of these core samples (red circles) along with other historic core sample locations by the USACE, most of which are included in the Texas Sediment Database (TxSed) detailed next.

Texas Sediment (TxSed) Database

The TxSed database (https://cgis.glo.texas.gov/txsed/) includes 109 cores and surface samples with actual grain size data accessible (passing sieve #200 or sediment fractions). Figure 2-2 shows locations of these data within the general project region grouped by decade. Figure 2-3 displays a

subset of data from Figure 2-2 where only the more recent available surface grab samples (sediment fraction data) from TxSed are shown.

USACE cores

Available USACE cores are documented in TxSed. Figure 2-4 shows the USACE cores with diamond symbols sorted by decade together with the more recent surface grab sample locations from Figure 2-3. These cores typically only include the fraction of near-surface sediment passing the #200 sieve and no detailed grain size distributions.

Other potential sources of recent surface sediment grain size information have been suggested. These include the Galveston Bay National Estuary Program, the Harris County Subsidence District, and USACE maintenance dredging records. However, no viable surface sediment grain size data were found based on these sources.

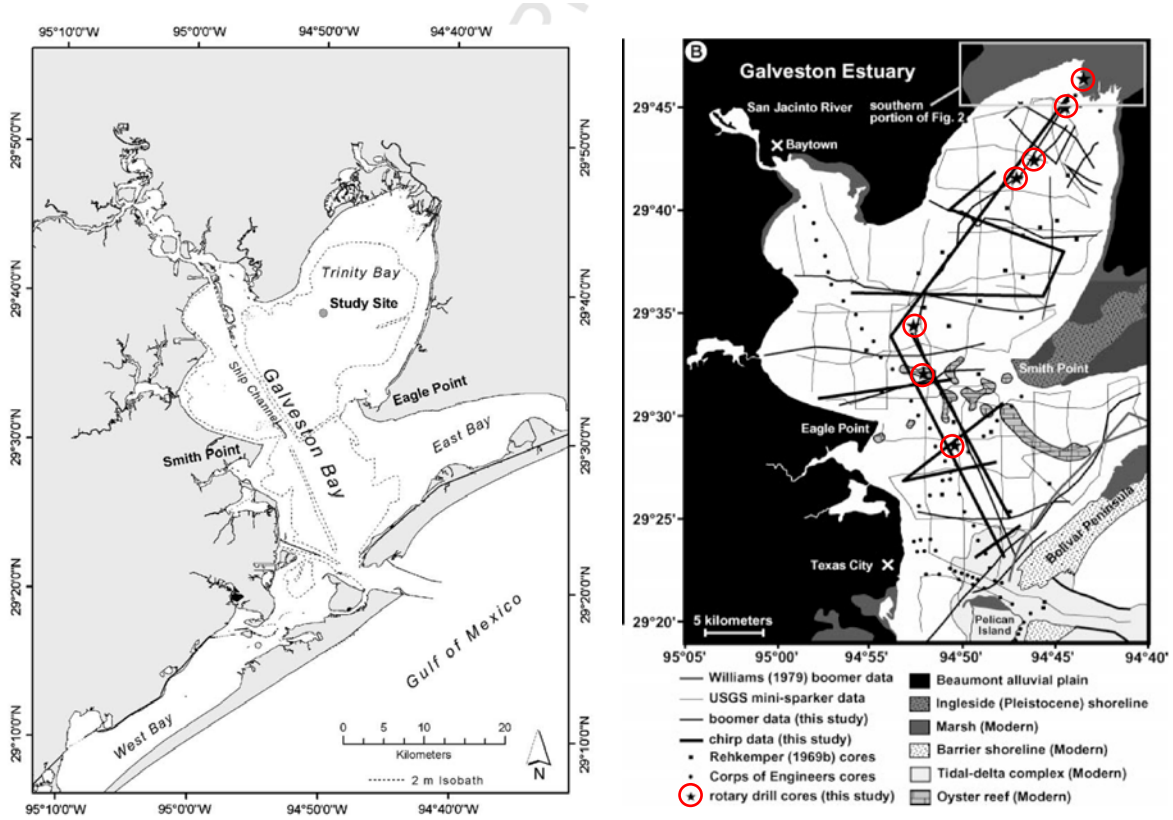

Figure 2-1: Left panel: Study site location of sediment core collected by TAMUG (Dellapenna Lab, Mead Allison) in Trinity Bay in 1999. Source: Dellapenna et al. (2006). Right panel: Locations of sediment cores collected by the Rice University John Anderson lab in 2002. Source: Rodriguez et al. (2005).

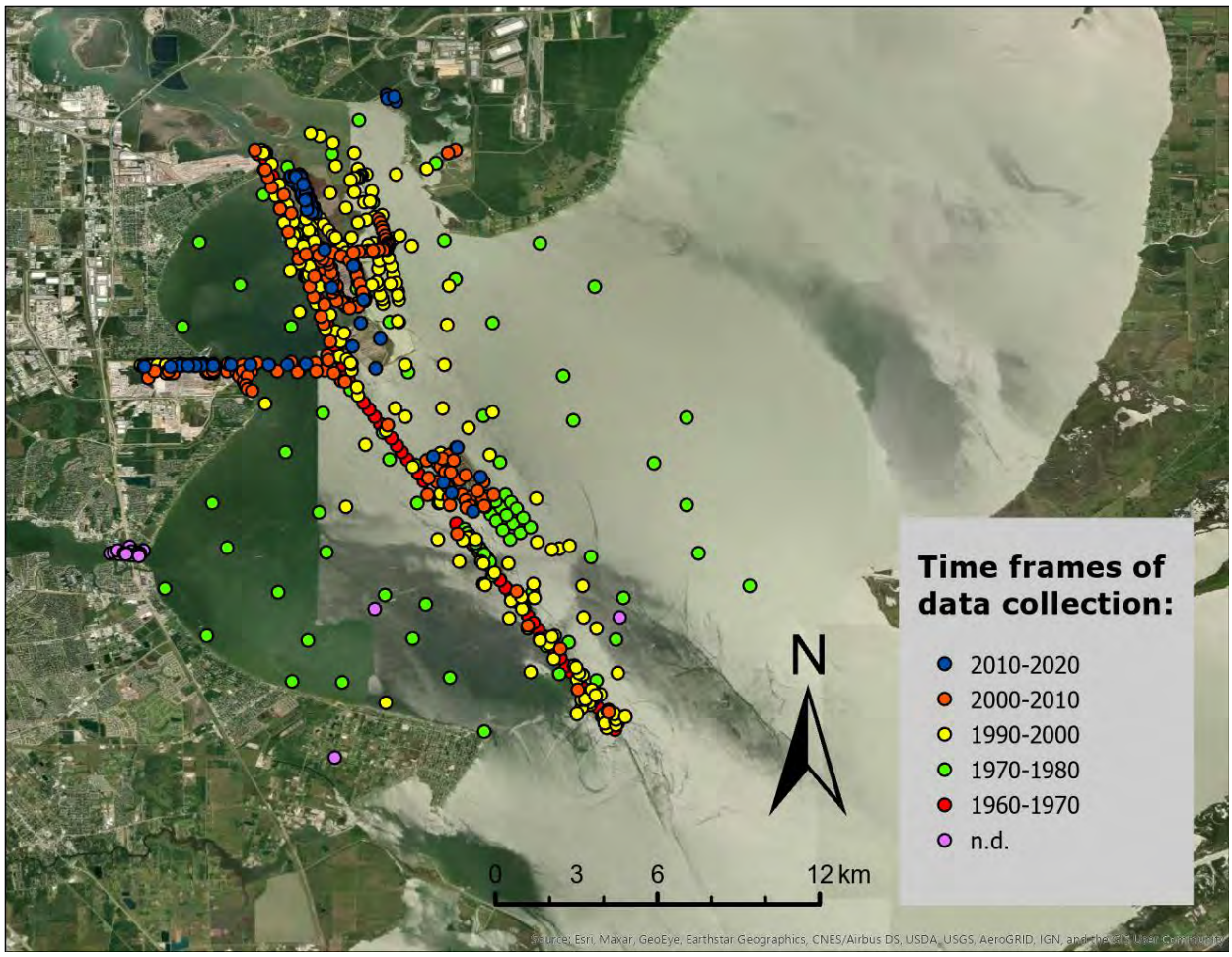

Figure 2-2: Historic bed sample locations in the general project area from TxSed with available data on bed grain size (passing #200 sieve or sediment fractions). Sample dates are indicated by color code.

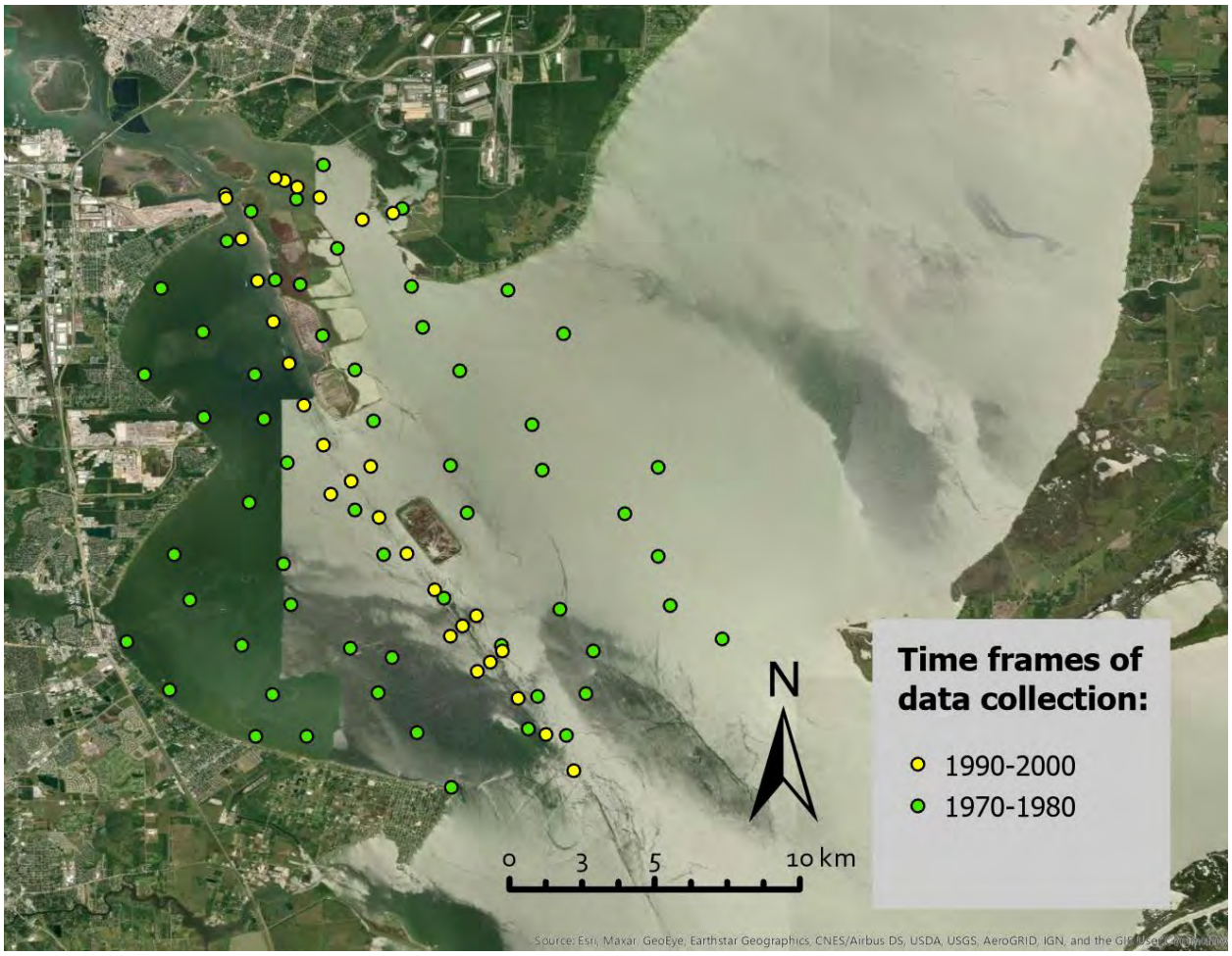

Figure 2-3: Most recent and available surface grab sample locations from the TxSed database.

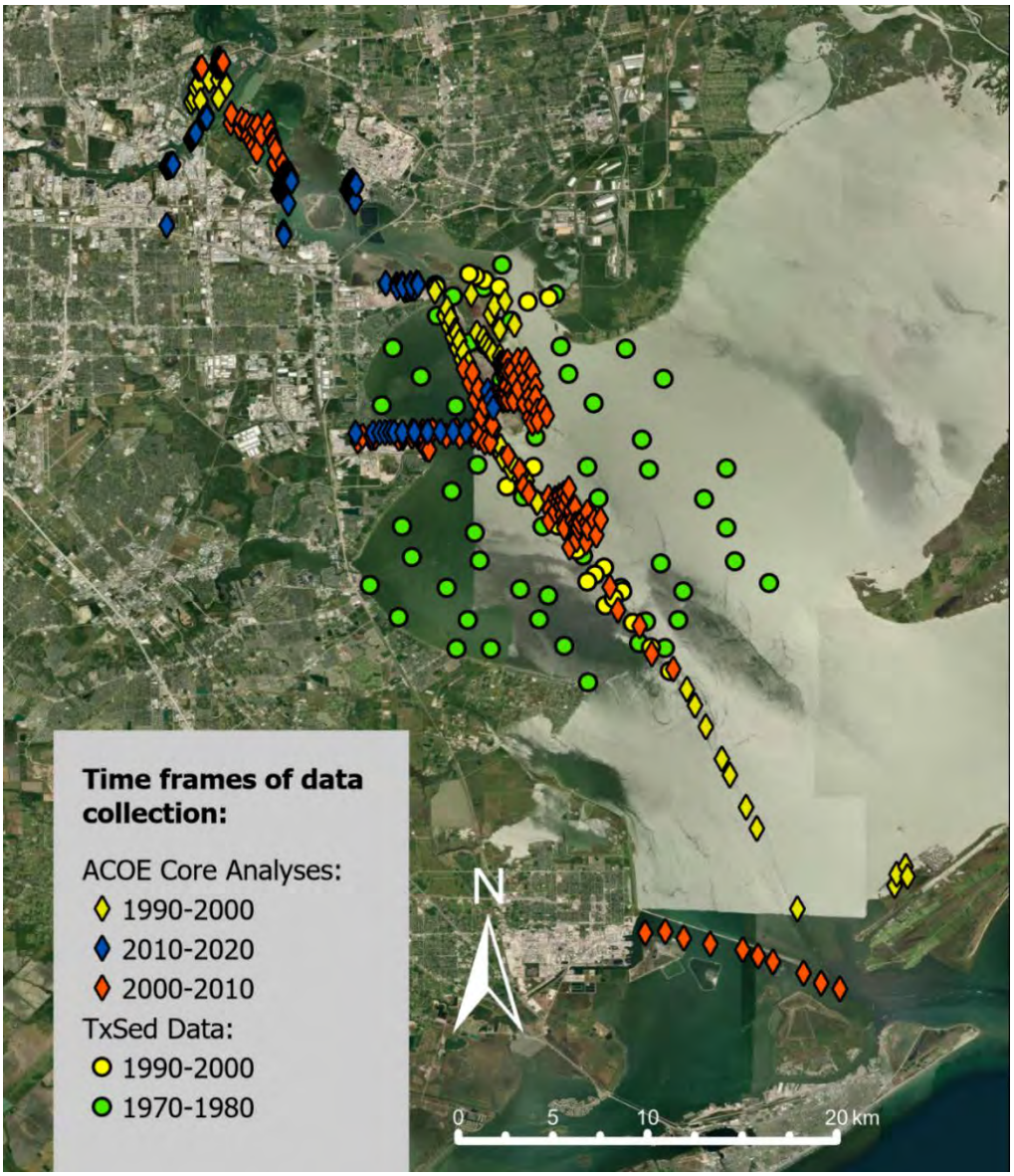

Figure 2-4: Locations of available relevant USACE core (diamonds) and recent TxSed surface (circles) sediment samples grouped by decade.

2.2 Tributary influx and salinity information

Current and historic data on water elevation (continuous stage data) and water discharge is available from several U.S. Geological Survey (USGS) stream gauges (https://txpub.usgs.gov/txwaterdashboard/). Figure 2-5 displays a screenshot from the USGS website with circles indicating locations of available stream gauges. These data can be used to some extent to track water inflow into the bay but they do not provide information on sediment influx. Figure 2-6 includes a Texas Water Development Board CTD (conductivity, temperature, depth) station

location in Trinity Bay where a 5-year time series is available. Other potential data sources such as the Harris County Flood Control District, San Jacinto River Authority, and National Marine Fisheries have been suggested but no relevant flux information could be found from these sources. The Dr. Dellapenna Lab at TAMUG has produced several publications related to sediment and contaminant influx and dynamics in Galveston Bay (Dellapenna et al., 2006,; 2020, 2022; Al Mukiami et al., 2018) including Hurricane Harvey contributions to sediment influx. In addition, two sites with CTD instruments in West Bay (WB) and East Bay (EB), respectively, collected hourly data for approximately one year in 2018. Figure 2-6 includes the locations of these stations. Extensive numerical modeling efforts of Galveston Bay salinity, sedimentary processes, and hydrodynamics have been completed by Dr. Du with the Dr. Kyeong Park Lab at TAMUG. Several resulting publications detailing the modeled information are available (Du and Park, 2019; Du et al., 2019, 2019a, 2019b, 2020).

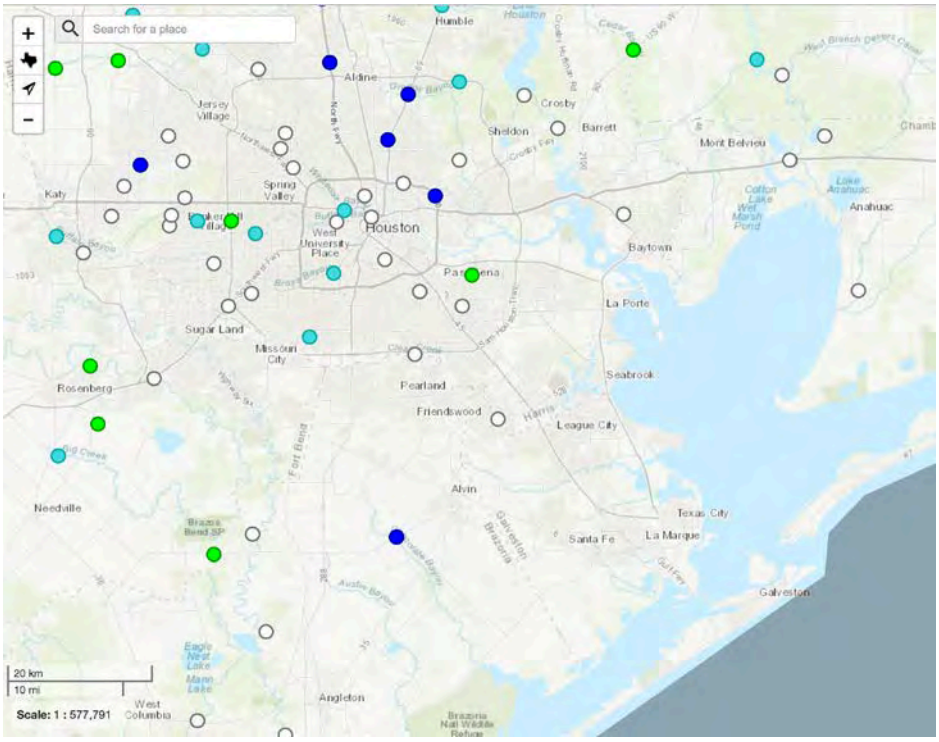

Figure 2-5: Locations of USGS stream gauge stations with data on continuous water levels, and flow rate. Colors indicate flow conditions at the time of the snapshot.

Source: https://txpub.usgs.gov/txwaterdashboard/.

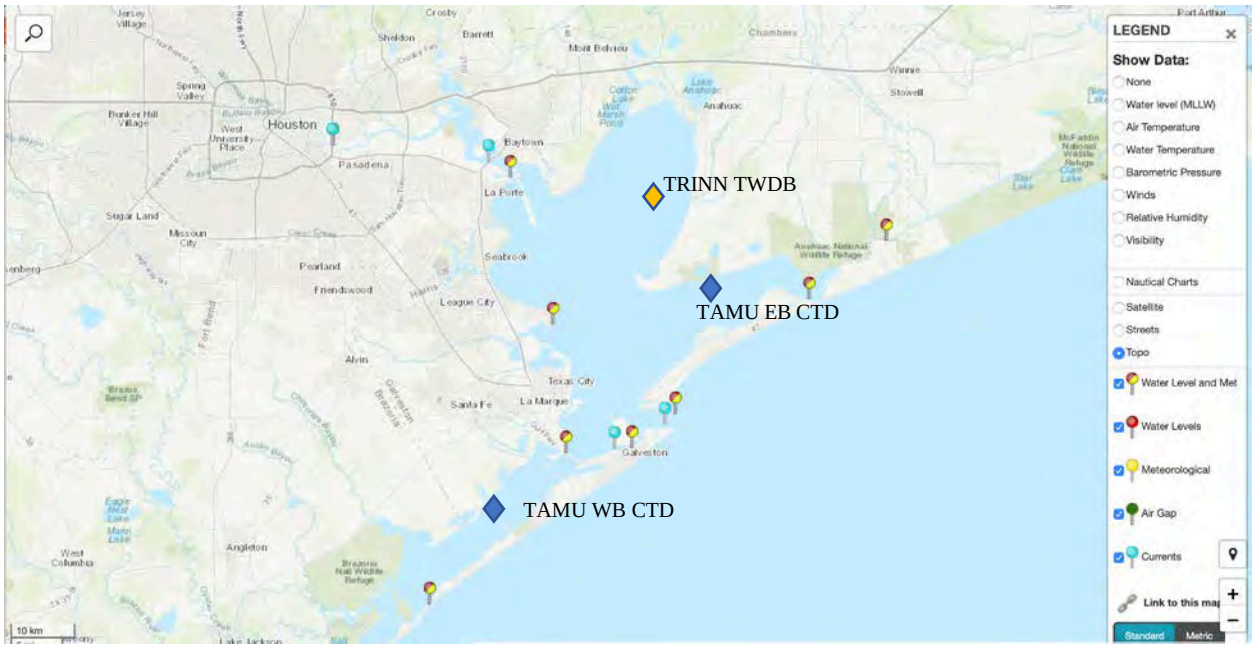

Figure 2-6: Locations of available current and historic hydrodynamic and salinity data in Galveston Bay. The base map includes stations accessible through the NOAA Tides and Currents portal (https://tidesandcurrents.noaa.gov/map/) where water level and meteorological stations are displayed as red/yellow circles and stations with current velocity information are displayed with light blue circles. The two blue diamonds indicate locations of TAMU CTD data and the orange diamond indicates the location of the TWDB station.

2.3 Wave and current hydrodynamic field data

Figlus Lab (TAMU)

A 10-month data set (three 17-minute bursts per hour at 2 Hz sampling frequency) on water free-surface elevation and 3D flow velocity were collected in 2017 and 2018 during and after construction of a new embankment around placement area PA10 south of Atkinson Island. Water depth at the measurement site ranged from 1.5 to 2.5 m on average. Figure 2-7 includes the measuring location labeled “TAMU PA10”. A current field measurement campaign with pressure gauges and acoustic Doppler velocimetry instruments near wetland edges is underway with 4 stations (1 in East Bay behind the Bolivar Peninsula and 3 in West Bay) being monitored for 2 weeks every 3 months. The campaign started in 9/2021 and is supposed to end by 11/2022. Four sets of these data have been collected and include high-resolution water surface elevation and flow velocities at sampling rates up to 16 Hz.

USACE

Current flow velocity data are available for intermittent time intervals since 2009 at the Bolivar Roads entrance to Galveston Bay and at the West End of the Galveston Harbor Channel between 2017 and 2021 (both station locations are included in Figure 2-6).

Two major in-situ measurement campaigns using AWAC (Acoustic Wave and Current) and Acoustic Doppler Velocimeter (ADV) instruments have been conducted recently. Locations are shown in Figure 2-7. The AWAC campaign measured velocity, salinity, and suspended sediment concentrations at 4 locations intermittently over 5 months in 2011 and it also included concurrent measurements of flow velocity and sediment load at the San Jacinto and Trinity river outlets (Figure 2-7). The ADV campaign measured free surface elevation, velocity, and suspended sediment concentration over 3 days in May 2012.

Other short-term measurements

URS completed a 1-month study in 2010 including bathymetry, velocity transects, suspended sediment and sediment samples, as well as CTD profiles along the Galveston ship channel entrance. Multiple short-duration point measurements of velocity profiles, salinity and temperature near Mid-bay Island, Texas City Dike to Bolivar and near San Leon were made by UT Austin in 2013.

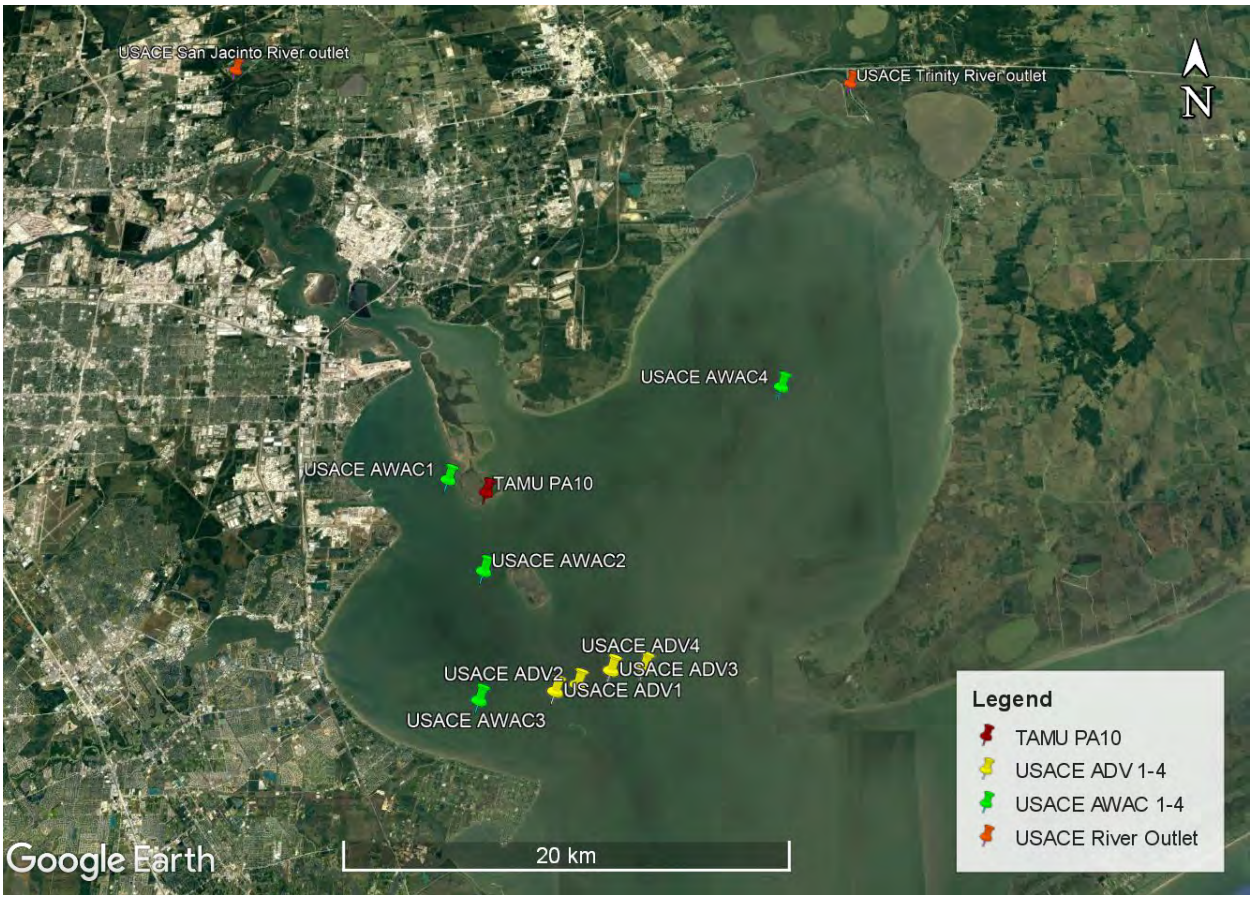

Figure 2-7: Locations of historic fixed-point wave and current measurements as well as river outlet flow and sediment load measurements.

The main take-away from the investigated datasets is that recent comprehensive synoptic measurements in the immediate project vicinity are lacking. While the historic data may help to identify sediment pathways to some extent, the data collection efforts as part of this project provide a more detailed and up-to-date view of ongoing sedimentation processes and pathways.

3 Bed Sediment

3.1 Sediment sampling

Several measuring campaigns spaced relatively close in time were conducted to collect bed sediment samples within the project region. Beginning in late September 2021, a series of cruises were conducted to collect sediment samples. Initially, a series of rocket cores were collected to obtain both sediment samples and core x-radiographs to determine bed changes since Hurricane Harvey. Five vibra cores were collected to determine decadal to centennial time scale sedimentation rates, and lastly a series of cruises were conducted to collect grab samples for the Sediment Trend Analysis (STA). The sampling plan was developed considering the data availability outlined in the data gap analysis. The gap analysis revealed that there is no recent synoptic dataset covering the area of interest, which is why a bed surface sampling grid for synoptic grab samples has been established in the general area around the Bayport flare (total of 131 sample points spaced approximately 500 m apart). Additional vibra-cores and gravity cores complete the bed sediment sampling efforts. The three sets of geological samples are explained further here:

Grab samples in San Jacinto Bay: a grid with 500 m spacing (a total of 131 samples) to determine grain size distributions from each site and to form the basis for the Sediment Trend Analysis (see Section 7.4.3).

Vibra-cores: each ranging from 2-3 m long to determine history of change in sediment size distributions; five cores were collected, four in the grab sample grid and one east of Atkinson Island. Geochronologies and age models were developed for each core using $^{210}Pb_{xs}$ (see Section 7.4.4).

Gravity cores (rocket cores or push cores): 10 gravity cores were collected at the same sites as samples collected after Hurricane Harvey around the bay; each core had x-radiographs shot to determine changes since Harvey, grain size distributions of the surface of cores to determine changes in texture (see Section 7.2.4).

Table 3-1 lists details of the various bed sampling campaigns conducted as part of this project. Figure 3-1 shows the location of all sediment samples detailed in Table 3-1 as well as locations of samples collected in previous efforts related to Hurricane Harvey deposits into Galveston Bay.

Table 3-1: Bed sediment sampling campaigns in 2021/22.

Date	No. of samples	Type of sample	Location
9/24/2021	5	vibra cores	San Jacinto Bay (Scott Bay)
10/08/2021	10	gravity cores	Lower Galveston Bay and East Bay
10/15/2021	26	grab samples	Lower San Jacinto Bay and east side of Atkinson Island
11/12/2021	28	grab samples	San Jacinto Bay and Bayport Flare
03/10/2022	38	grab samples	San Jacinto Bay and Bayport Flare
7/15/2022	39	grab samples	San Jacinto Bay and Bayport Flare

All surface grab samples have been analyzed for grain size distribution statistics. The primary system used was a Malvern Mastersizer 2000. The Malvern uses laser diffraction to determine grain size distributions. Triplicate measurements of sample grain size distributions for each sample site were produced and then averaged. Grain size distributions and statistics were then exported and compiled. Grain size analyses results and statistics, including mean size, mode, skewness, standard deviation (sorting), D_{25}, D_{50}, D_{75}, D_{90}, % clay, % silt, % sand, and dominant grain size class are provided. Summary tables are given in Appendix A. Maps detailing the distribution of sediment fractions and of the most important bed sediment statistical parameters are used to provide a sense of the spatial distribution of sediment characteristics. Figure 3-2 shows a map of the percentage of clay fraction and Figure 3-2 shows the spatial distribution of the median grain diameter as examples. Additional parameter maps can be found in Appendix A. These data are useful in understanding the composition of the bed in the project area, to identify potential sources of bed sediment, to confirm numerical model setups, to perform sediment transport modeling, to design mitigation structure foundations, and to perform an STA.

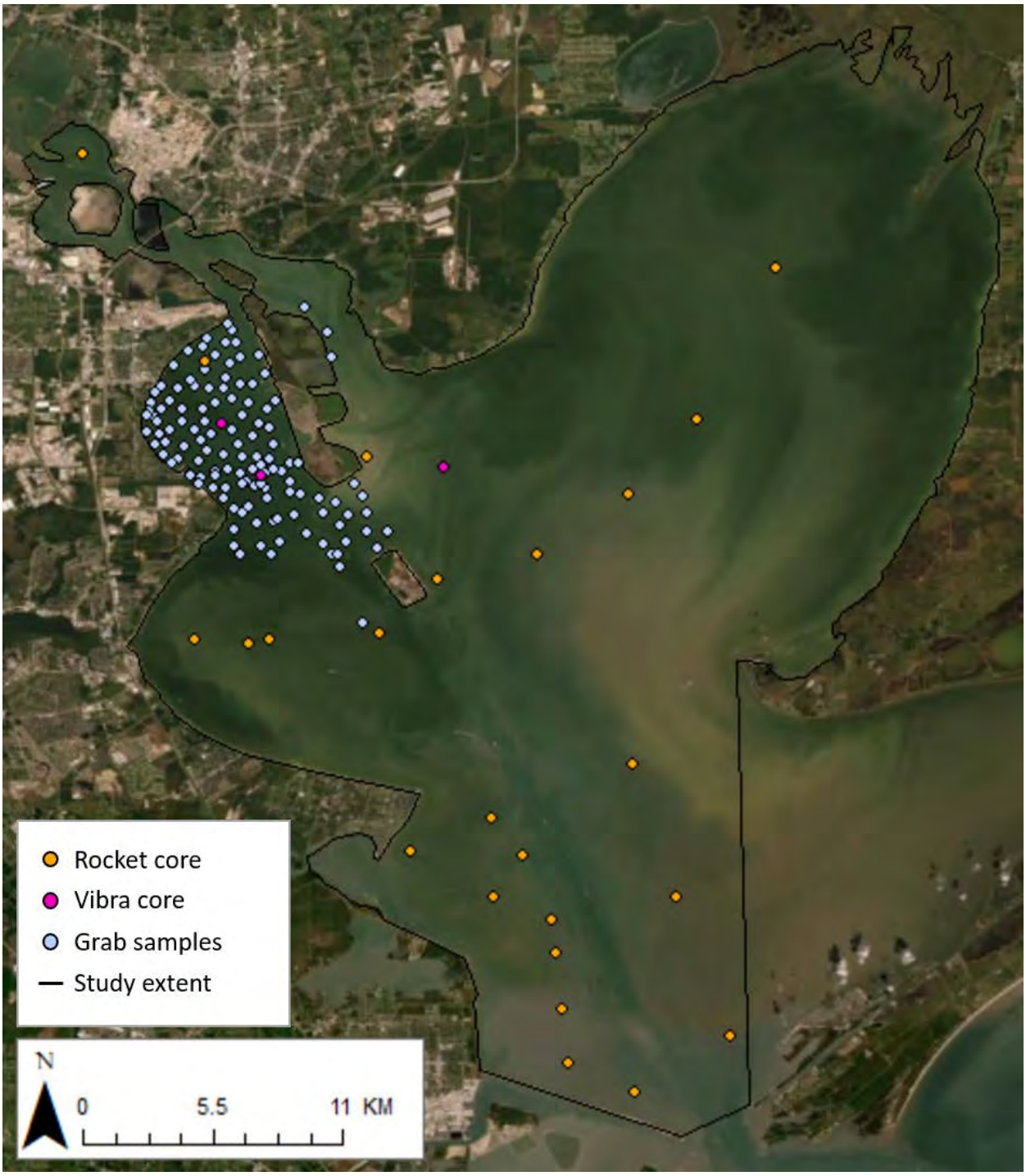

Figure 3-1: Locations of all sediment samples detailed in Table 3.1 and prior efforts. Samples are color-coded based on type (orange: rocket cores; magenta: vibra cores; blue: grab samples).

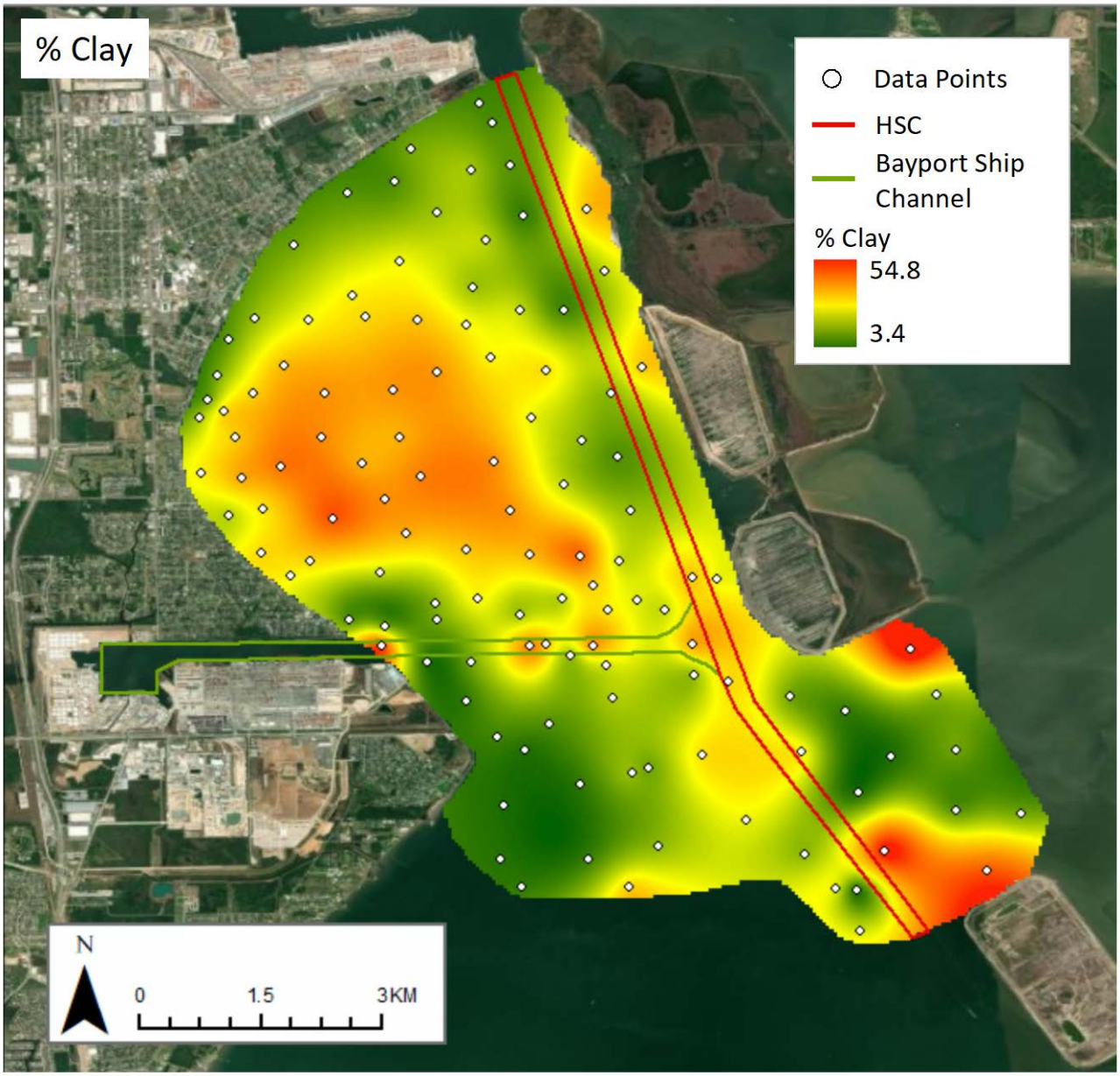

Figure 3-2: Map of clay percentage in the project area.

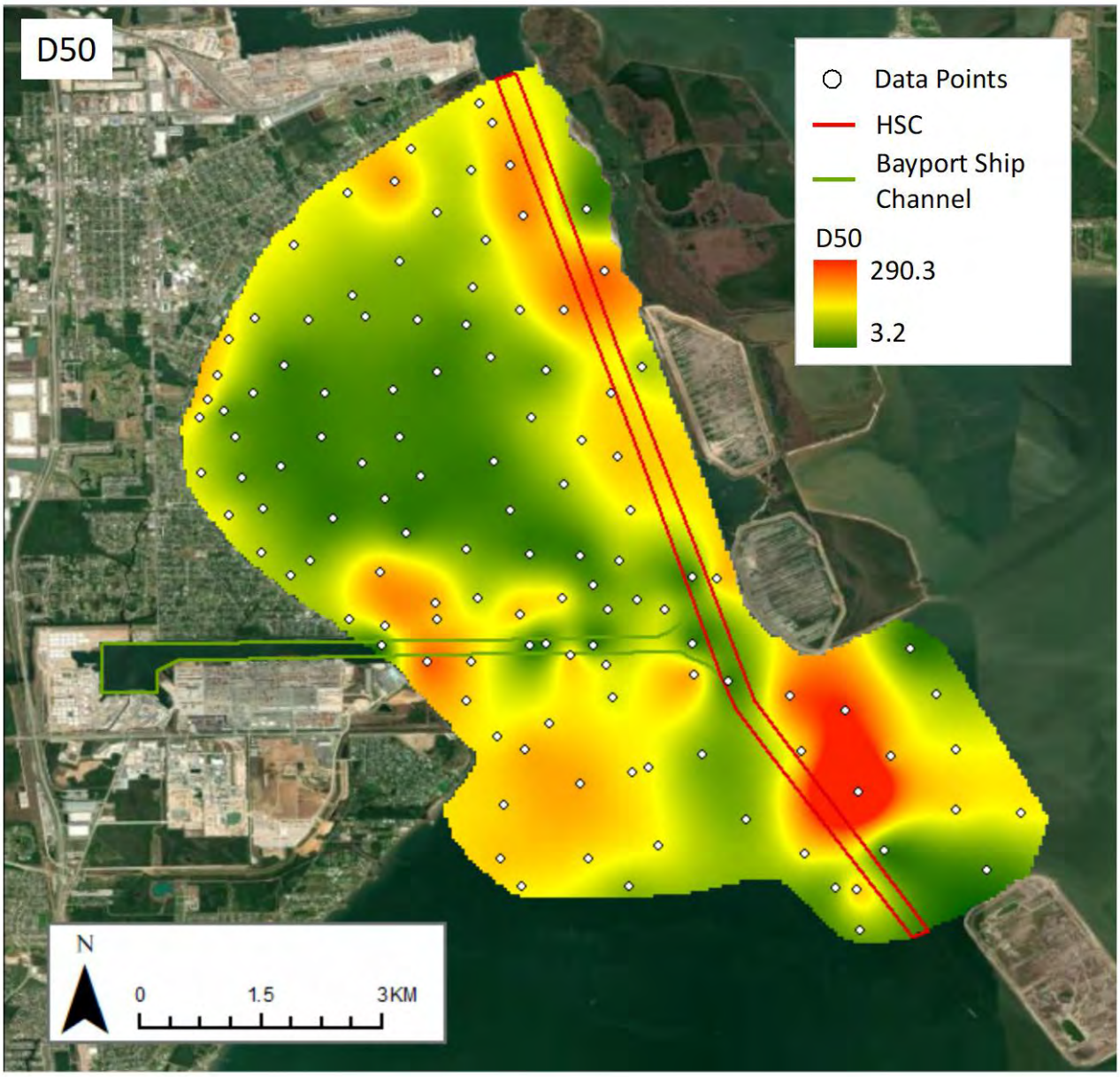

Figure 3-3: Map of median grain diameter (D50 in μm) in the project area.

3.2 Critical bed shear stress

Critical bed shear stress is the shear stress required to mobilize bed sediments. How sediment becomes mobilized varies greatly depending on whether the sediment can be assumed to be cohesive or non-cohesive. For example, quartz grained sediments, like sands, are non-cohesive. Where clays and some silts, which have intermolecular forces and pore pressures acting between

particles, are generally cohesive. Sediment analysis of surface grab samples detailed in Section 3.1 above shows that d_{50} ranges from 0.0061 mm to 0.1426 mm around the study area, indicating that particle size ranges from fine sands to clays. Therefore, sediments in the study area are likely to be a mix of cohesive and non-cohesive.

3.2.1 Non-cohesive sediments

A first order approach to determining critical shear stress is to estimate it based on particle size. For non-cohesive material, Cao et al. (2006) developed an explicit formulation to determine a critical Shield's parameter to a given sediment grain size. Figure 3-4 shows this relationship, where red lines indicate the range of d_{50} sediment sizes seen within the study area.

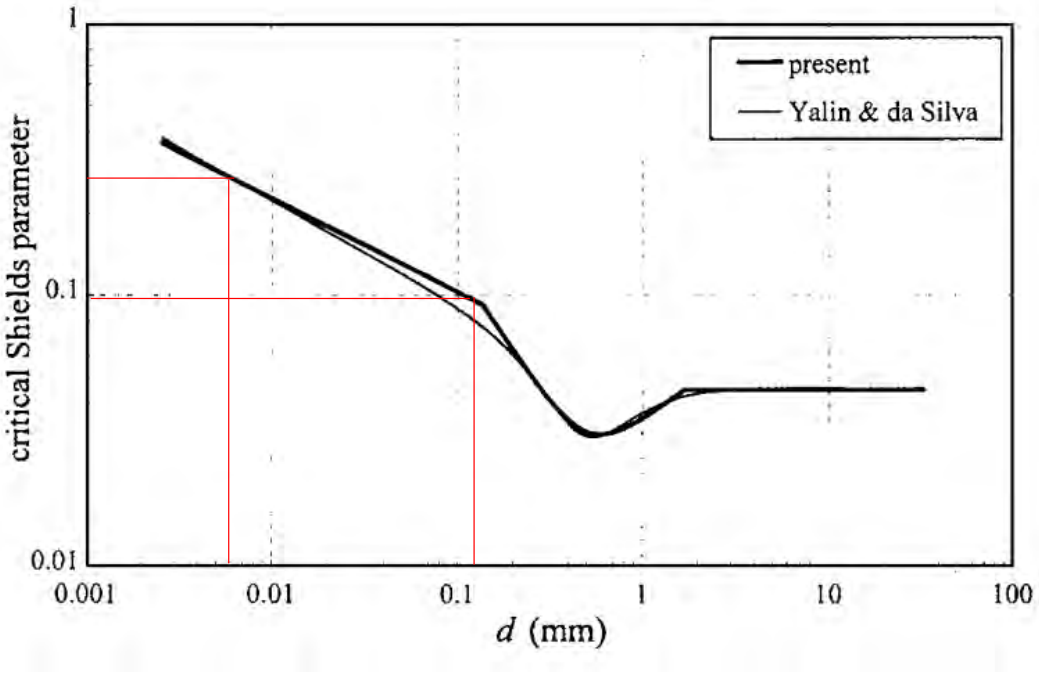

Figure 3-4: Critical Shields parameter as a function of grain size (Cao et al. 2006).

From Figure 3-2 we can assume a logarithmic relationship between critical Shields parameter (θ_c) and particle diameter (d_{50}):

Minimum particle diameter (d_{50}) in sample – 0.0061 mm

Maximum particle diameter (d_{50}) in sample – 0.1426 mm

Assuming linear (logarithmic) relationship between θ_c and d_{50}:

$$\log(\theta_c) = m * \log(d) + c \quad (3\text{-}1)$$

where m = -0.267, c = -1.261. Using the critical Shields parameter, we can determine a critical shear stress (τ_c) required for incipient bedload sediment transport:

$$\tau_c = \theta_c(\rho_s - \rho)g(d_{50}) \quad (3\text{-}2)$$

where ρ_s and ρ are the density of sediment and water, respectively.

3.2.2 Cohesive sediments

From ADV measurements near the bed, Salehi and Strom (2012) determined a Shield's parameter of 0.1 to be a good representative for fine cohesive sediments in the San Jacinto Estuary. Using (3-2), a direct relationship between d_{50} and critical shear stress is determined. For calculations in sediment data accompanying this report, a sediment particle density of 2650 kg/m^3 (s = 2.65) is assumed. Sediment statistics and critical shear stress values for each collected sample are provided as a separate spreadsheet to accompany this report. It needs to be noted here that this approach of estimating critical bed shear stress is rather crude since it does not incorporate some of the physics responsible for mobilizing mixed sediments. Thus, the provided values should be considered a first approximation only.

4 Hydrodynamics

Hydrodynamic field data consisting of water level fluctuations and flow velocities have been collected using multiple methods and instruments. Fixed-instrument deployments were carried out using bottom-mounted pods containing combinations of pressure transducers (PT) and tilt current meters (TCM). Acoustic Doppler current profilers (ADCP) were also placed on the bed in the area of interest, recording velocity profiles over the entire water column (ADCP). Pressure transducers are integrated with the ADCP to provide water surface fluctuation information in addition to the velocities. Vessel-mounted ADCP measurements were also completed along 27 transects throughout the project area at specific times in the tidal cycle. These measurements provide velocity readings over the depth of the water column along the vessel travel path. In addition, the collected acoustic data from the vessel runs are used to estimate suspended sediment concentrations (SSC). The product of velocity and SSC provides an estimate of instantaneous sediment flux across the specified transect length. Flux estimates are further discussed in Section 5.3. Hydrodynamic data from fixed and vessel-mounted measurement campaigns are detailed in the following sections.

4.1 Fixed instrument deployment

Several fixed location instruments were deployed over a 2-week period in April 2022 spanning a full spring tidal cycle. Strong south-easterly winds kept water levels in the project area significantly higher than predicted tide levels alone and added significant wave energy to the region. Figure 4-1 shows a wind rose from Morgan's Point (Station No. 8770613), the closest NOAA meteorological station to the study area, where Figure 4-2 illustrates increased water levels above predicted levels over most of the deployment due to this sustained southwesterly wave activity.

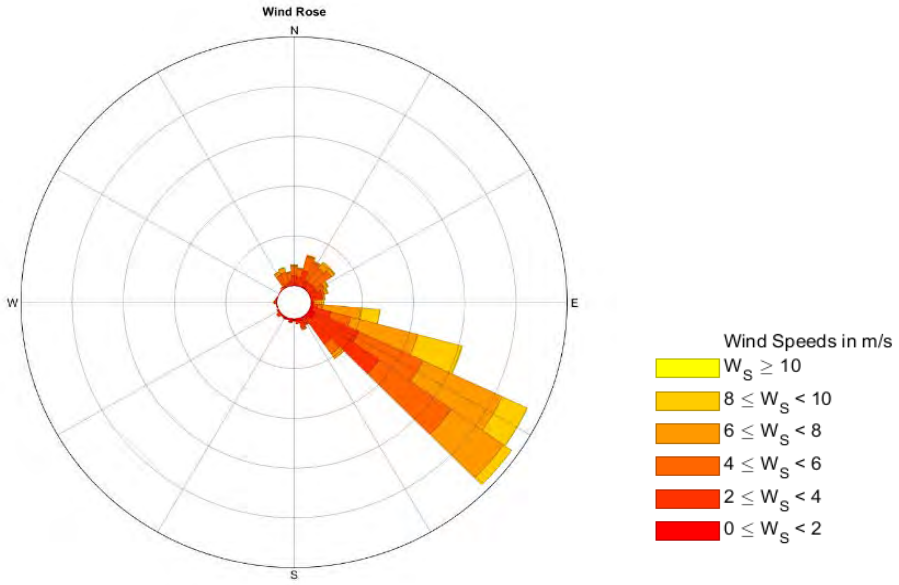

Figure 4-1: Wind rose for Morgan's Point/ Barbour's Cut over fixed deployment in April 2022. Each cell shows direction the wind is coming from. Data sourced from NOAA Station No. 8770613.

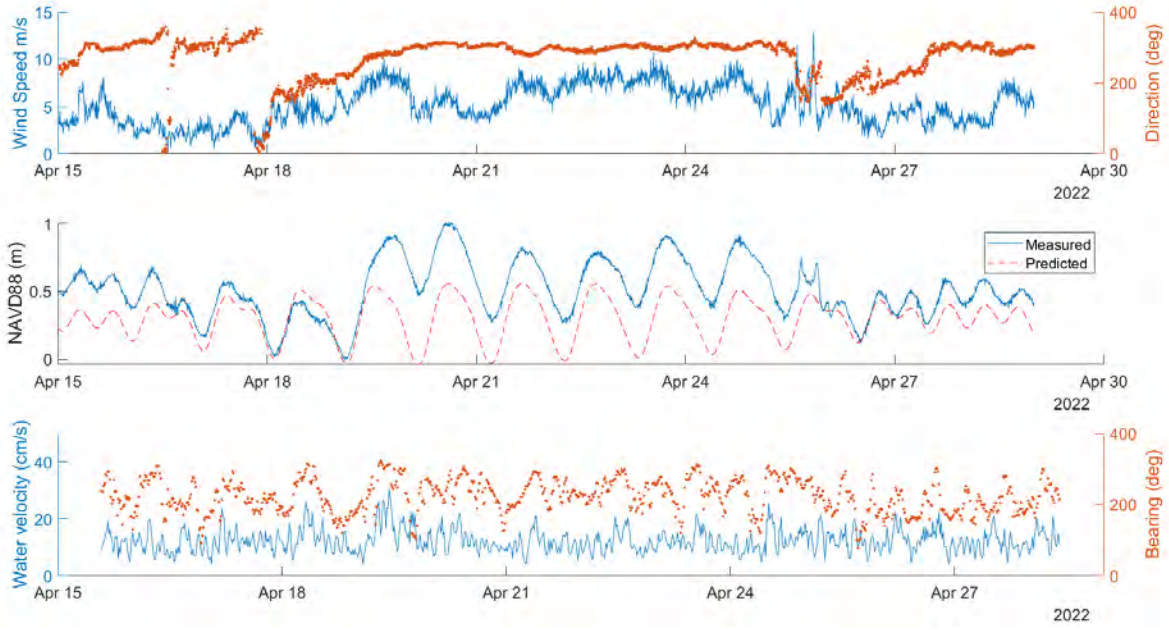

Figure 4-2: Wind speed and direction at Morgan's Point NOAA station 8770613 (top), measured (ADCP PT) and predicted (Morgan's Point) water levels (middle), and measured (ADCP) bottom current speed and direction (bottom) over the entire deployment period from 15 – 28 April, 2022.

Seven pressure transducers (PT) (5 RBR SoloD and 2 SoloD|Wave) capable of recording water pressure up to 16 Hz in water depths of up to 20 m were used during the deployment period. Each pressure sensor was paired with a TCM to record near-bed velocity in addition to the water free-surface fluctuations. TCM instruments recorded velocity and bearing continuously at 1 Hz. In addition, a bottom mounted ADCP (Aquadopp Profiler 2 MHz) with built in pressure transducer and attached Optical Backscatter Sensor (OBS) was deployed during the same period. The ADCP recorded ADV burst data at 2 Hz for 2048 samples every 20 minutes and recorded a velocity profile at the end of each burst cycle, averaged over 30 seconds at a sampling rate of 24 Hz. A map showing fixed deployment locations is given in Figure 4-3, with geographical coordinates given in Table 4-1 and a summary of sampling methods and accuracies for each instrument provided in Table 4-2. Time series plots for all fixed instruments are given in Appendix B.

Figure 4-3: Locations of fixed instruments deployed 15-28 April 2022. Yellow pins indicate TCM and RBR pressure transducer pairs. The red pin indicates a bottom mounted ADCP.

Table 4-1: Geographical locations for each fixed instrument deployment.

Name	Latitude	Longitude
TC1	29.665038°	-94.981322°
TC2	29.644115°	-95.001524°
TC4	29.606281°	-94.976611°
TC5	29.598029°	-94.935820°
TC7	29.604930°	-94.957269°
ADCP2	29.618584°	-94.964433°

Table 4-2: Sampling methods, elevations and accuracies for each fixed instrument.

Instrument type	Sampling method	Sampling Rate	Measurement Elevations	Accuracy
PT	Continuous	TC2: 2 Hz, 16 Hz for all others	Assumed at bed	± 0.05% of reading
TCM	Continuous	1 Hz	10 cm above bed	± 2 cm/s ± 2% of reading
ADCP Burst	Point measurement, 1m bin size	2 Hz Burst over 2048 samples, every 20 min	Instrument 0.23 m above bed, blanking distance 0.1 m	± 0.5 cm/s ± 1% of reading
ADCP Profile	Averaged velocity profile, 0.1 m bin size	2 Hz averaged over 30 seconds, every 20 min	Instrument 0.23m above bed, blanking distance 0.1m	± 0.5 cm/s ± 1% of reading

The measured near-bottom current velocities during the entire deployment (15 – 28 April, 2022) are summarized using current rose plots for select instruments in Figure 4-4. Current speed is indicated by color and direction from which the current originates is indicated by the respective frequency of occurrence in each bin.

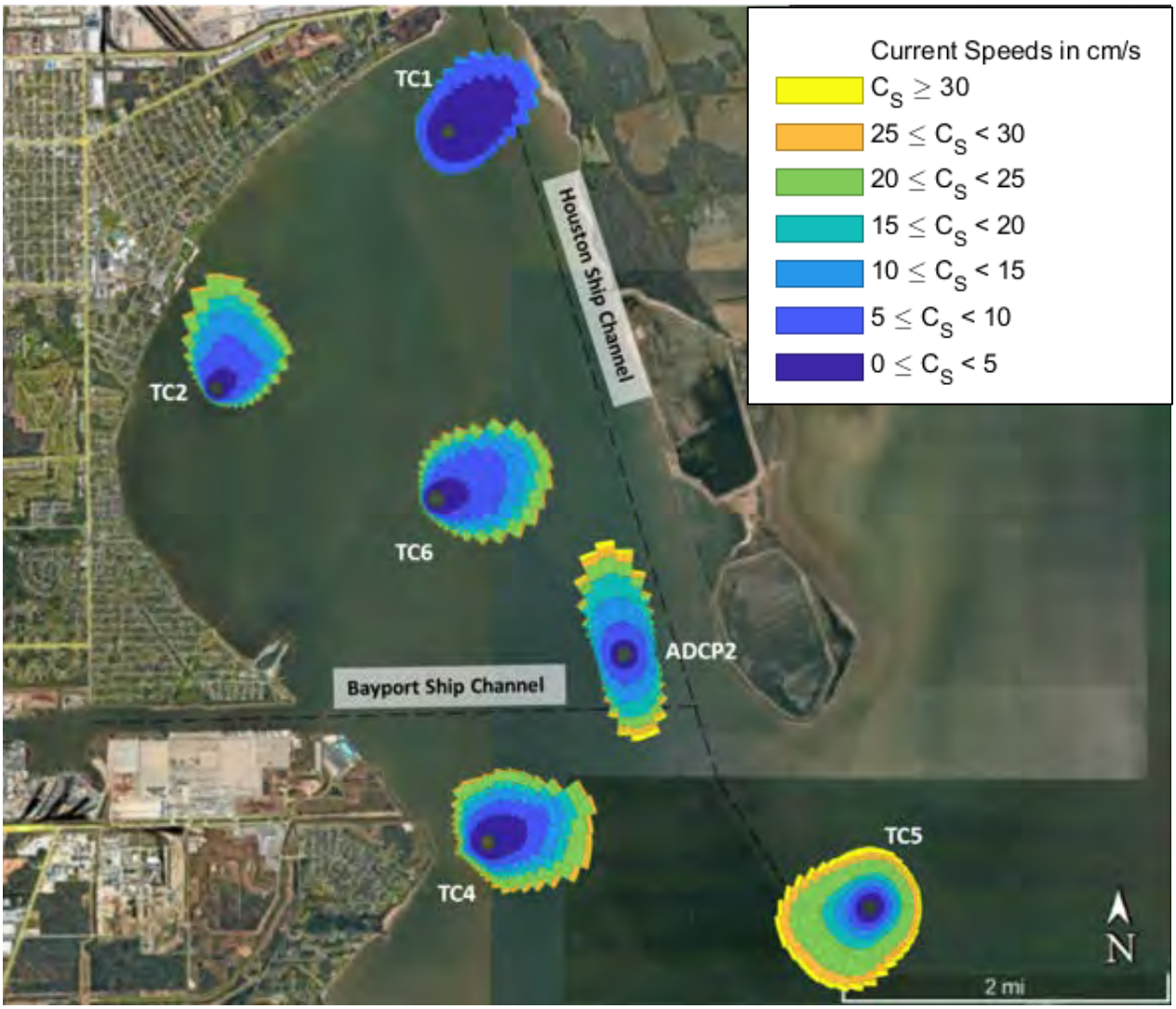

Figure 4-4: Bottom current velocity roses for select instruments over the entire deployment period from 15 – 28 April 2022.

4.2 Vessel-mounted measurements

Vessel-mounted ADCP measurements of current profiles were conducted using a TAMU-owned system consisting of a Nortek Signature 1000 ADCP combined with a GNSS heading compass and positioning system mounted on a moon pole attached to a TAMUG research vessel as depicted in Figure 4-5. The Signature 1000 is a 1000-kHz, low form factor, 5-beam system capable of generating high-resolution 3D velocity profiles throughout the water column. The maximum profiling range is 30 m with a maximum number of cells of 128 (cell size 0.2 – 2 m). Velocity resolution is down to 0.1 cm/s with a minimum accuracy of +/- 0.3 cm/s. The maximum sampling

rate is 14 Hz. Depth measurements are collected at a maximum sampling rate of 2 Hz with a vertical resolution of 0.001 m. As the vessel moves along scanning transects through the water, current data is visualized in real time via computer screen onboard the vessel as a first check for quality control. The data are stored on the instrument's data logger and a field computer. Post-processing and visualization of the raw 3D current profile and positioning data is done using the Nortek visualization tool and MATLAB.

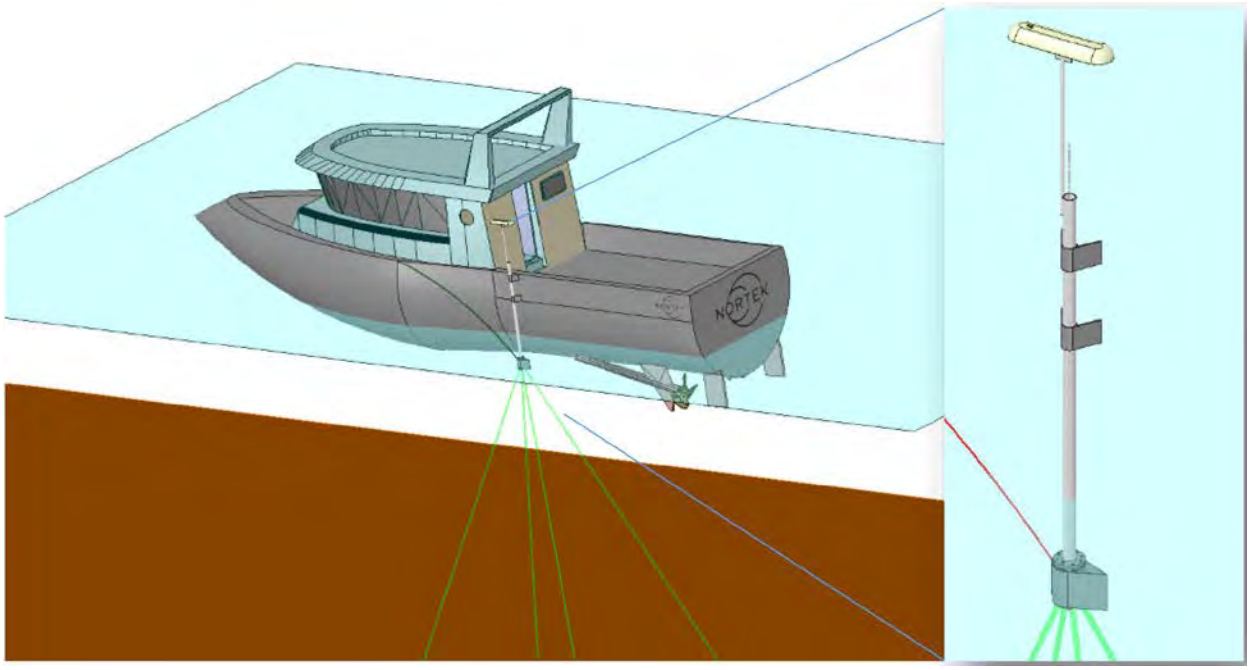

Figure 4-5: Schematic of the Signature 1000 ADCP and heading compass system setup. Shown is the side-mounted option used for this project where a moon pole is bracketed to the vessel hull with the ADCP on the bottom end (water) scanning downward and the GNSS heading compass at the top (air).

Operating vessel speed was kept between 3 and 6 knots to guarantee maneuverability while at the same time avoid excessive wake formation and bubble entrainment that could lower the quality of the collected current data. The ADCP scans cover the entire water column pointing downward starting from about 2 feet below the water surface. To avoid interference from passing vessel wakes, data collection was stopped to allow other vessels to pass and then resumed after residual wake motions had died down. Transects across channel entries and open water boundaries of the project area are helpful to characterize hydrodynamics and estimate related sediment fluxes. Transects

were collected across most major tributary entries into Galveston Bay and inside the shallow sections of the immediate project area. Transect paths are detailed in Figure 4-6. Table 4-3 lists names, beginning and end coordinates for each transect. An example track showing measured velocities is given in Figure 4-7, with figures of tracks and velocities for all remaining runs shown in Appendix C.

Figure 4-6: Locations of all 27 vessel tracks for VM ADCP data collection runs.

Table 4-3: Start and end coordinates for VM ADCP runs.

Name	Latitude Start	Longitude Start	Latitude End	Longitude End
20220201_BayportChannel_Ebb_Data	29.613928	-94.992955	29.612821	-94.950124
20220201_FHB1_Ebb_Data	29.697113	-95.000428	29.697268	-95.001187
20220201_FHB2_Ebb_Data	29.696533	-94.999782	29.699893	-94.996053
20220201_MorgansPoint1_Ebb_Data	29.683740	-94.985963	29.684853	-94.988606
20220201_MorgansPoint2_Ebb_Data	29.682164	-94.978691	29.670363	-94.988559
20220201_SanJacBay1_Ebb_Data	29.669399	-94.989903	29.652916	-94.969151
20220201_SanJacBay2_Ebb_Data	29.648442	-94.966101	29.656333	-95.000887
20220201_TrinityBay_Ebb_Data	29.696725	-94.733022	29.701401	-94.733380
20220210_AtkinsonIslandSouth_Flood_Data	29.614982	-94.951217	29.586199	-94.927120
20220210_BayportChannelNorth_Flood_Data	29.625858	-94.957191	29.622461	-94.995733
20220210_BayportChannelSouth_Flood_Data	29.623027	-94.996208	29.615052	-94.951378
20220210_BluewaterAtoll_Flood_Data	29.587028	-94.926662	29.601182	-94.979979
20220210_BuffaloBayou1_Ebb_Data	29.764241	-95.079350	29.763674	-95.077775
20220210_SanJacBay3_Flood_Data	29.637239	-95.014203	29.642488	-94.963040
20220419_SanJacBay4_Flood_Data	29.645796	-94.964213	29.634136	-95.010548
20220419_SanJacBay5_Flood_Data	29.632230	-95.006841	29.627038	-94.993775
20220419_SanJacBay6_Flood_Data	29.626468	-94.992802	29.613047	-94.951992
20220419_SanJacBay7_Flood_Data	29.612913	-94.952200	29.605149	-94.982623
20220419_SanJacBay8_Flood_Data	29.605159	-94.982657	29.609923	-94.986422
20220421_Kemah_1_Ebb_Data	29.548669	-95.021381	29.549117	-95.020826
20220421_Kemah_2_Ebb_Data	29.549112	-95.020825	29.549067	-95.020763
20220421_Kemah_3_Ebb_Data	29.548866	-95.020251	29.549298	-95.021530
20220421_Kemah_4_Ebb_Data	29.549300	-95.021557	29.549928	-95.024669
20220421_Kemah_5_Ebb_Data	29.549899	-95.024542	29.549261	-95.024641
20220421_Kemah_6_Ebb_Data	29.549479	-95.024767	29.549875	-95.015063
20220421_Kemah_7_Ebb_Data	29.549925	-95.015068	29.547106	-95.015503
20220421_Kemah_8_Ebb_Data	29.547097	-95.015562	29.548710	-95.021352

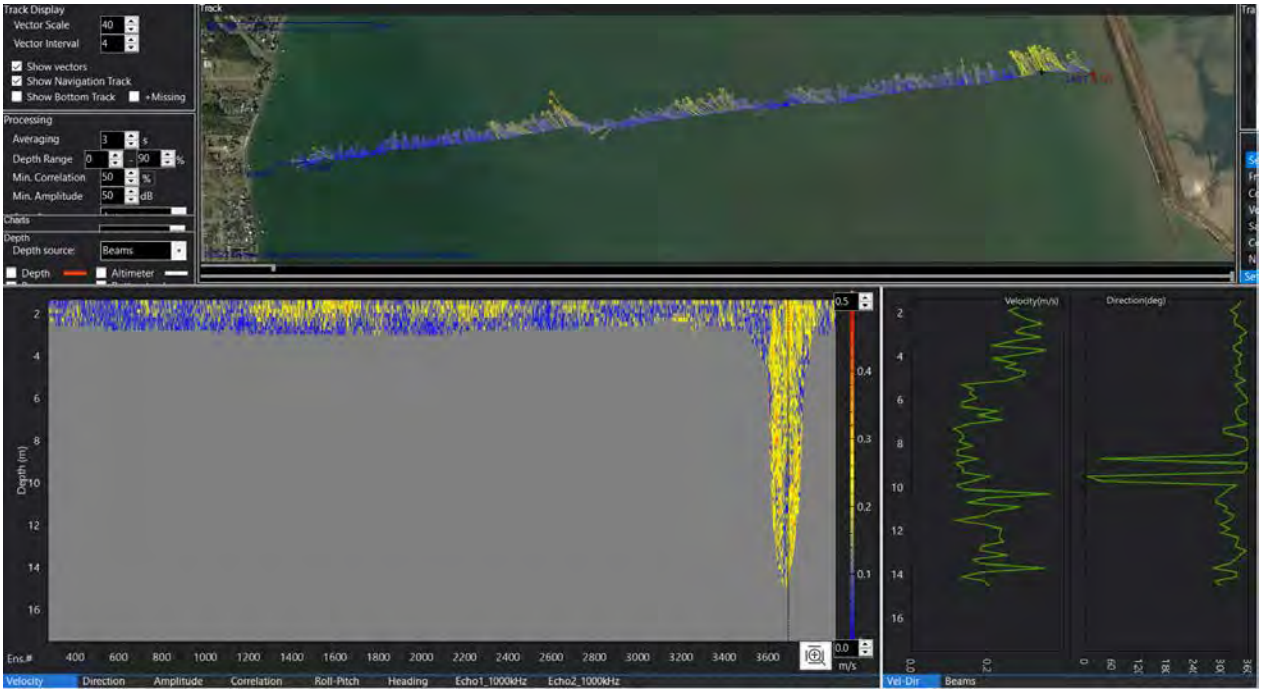

Figure 4-7: Vessel track and velocities for 20220210_SanJacBay_3_Flood run.

5 Suspended Sediments and Fluxes

Suspended sediment measurements and flux estimations are accomplished through a combination of in situ water sampling, acoustic measurements from vessel-mounted ADCP transects, and optical backscatter measurements during fixed instrument deployment. Fluxes are then estimated as the product of measured velocities and suspended sediment concentrations. Additionally, tributary contributions of water and sediment to the project area are estimated from published drainage basin sizes and estimated tributary stage curves.

5.1 Water samples

Several water samples were collected between February and April 2022, at various locations and tidal stages. Each sample was taken at approximately 2 ft below the water surface and filtered to determine the total mass of suspended sediment within each sample, which was then turned into a suspended sediment concentration (SSC). Water sample locations, times and sediment concentrations can be seen in Table 5-1.

Table 5-1: Water sample locations, times, and SSC.

Sample Name	Lat	Long	Date	Time	Water Depth	Tidal phase	SSC (mg/L)	Error (mg/L)
SFH B-1	29.68467	-94.99973	2/1/2022	10:50 AM	5.5 ft	Ebb	48.3	0.0
SJB-1	29.65177	-94.96857	2/1/2022	12:50 PM	17.6 ft	Ebb	19.7	2.3
TB-1	29.69785	-94.73457	2/1/2022	2:50 PM	5.8 ft	Ebb	5.5	0.5
BB-1	29.76472	-95.08425	2/10/2022	9:38 AM	24.4 ft	Slack after Ebb	35.6	1.8
SJR-1	29.78728	-95.06492	2/10/2022	10:10 AM	27.6 ft	Almost slack after ebb	28.5	1.5
BB-2	29.74148	-95.10525	2/10/2022	10:26 AM	33 ft	Almost slack after ebb	10.8	0.6
OP-4	29.49777	-94.84614	2/14/2022	11:46 AM	12 ft	Slack after ebb	12.7	0.2
BPF	29.61753	-94.96474	4/28/2022	12:00 PM	14 ft	Almost slack after ebb	20.5	-

5.2 Acoustic measurements

An inbuilt echosounder feature on the Signature1000 used for VM runs was used to infer suspended sediment concentrations. This optional feature uses the center transducer of the instrument, fixed at 1000 kHz to return high resolution reflection intensities to detect suspended sediment, biomass, or fish. The echosounder was run with a cell size of 0.06 m, and a blanking distance of 0.1 m. An example echogram from echosounder backscatter is shown in Figure 5-1.

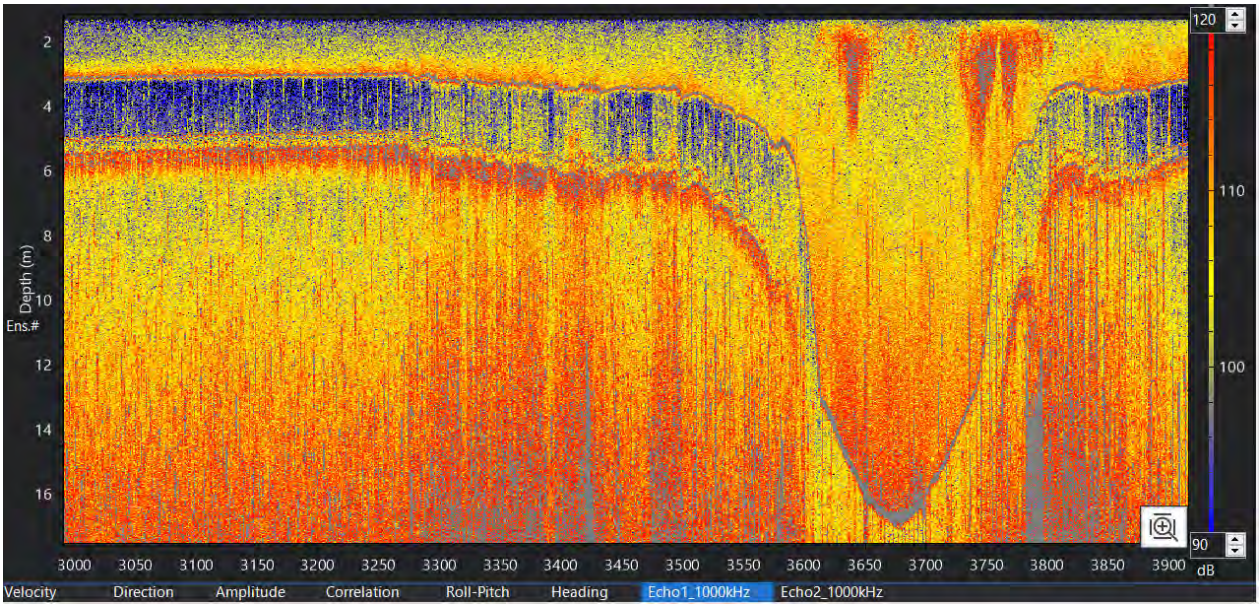

Figure 5-1: Echogram of a section of 20220210_SanJacBay3_Flood_Data, ranging from 90 to 120 dB.

Using echosounder backscatter (SCB), suspended sediment concentration (SSC) can be expressed as:

$$\log(SSC) = 0.1 \times (SCB) + C \qquad (5\text{-}1)$$

where *C* is a constant specific to the instrument and site conditions. This constant was determined by taking background concentrations measured from water samples (Section 5.2) and comparing them to background readings from echosounder data using the equation above. For all runs, a *C* value of -8.63 was used.

5.3 Optical measurements

As part of the fixed instrument deployment, the Aquadopp ADCP had an Optical Backscatter Sensor (OBS) attached. This device faced parallel to the bed and took a single point measurement at an approximate elevation of 0.23 m above the bed. This instrument measured at the same burst frequency of the ADCP (2 Hz for 2048 samples every 20 min) and returned an output analog voltage signal. The OBS voltage signal was translated to SSC using a turbulence chamber. The device was placed in a bucket of water with a known volume and changes in output signal were recorded as known quantities of sediment were added to the bucket incrementally. The bucket was stirred continuously to maintain consistent turbulent conditions and keep sediment in suspension. The results of the calibration are given in Figure 5-2. This calibration curve was used to determine SSC measured by the OBS. A portion of the deployment timeseries for SSC is given in Figure 5-3.

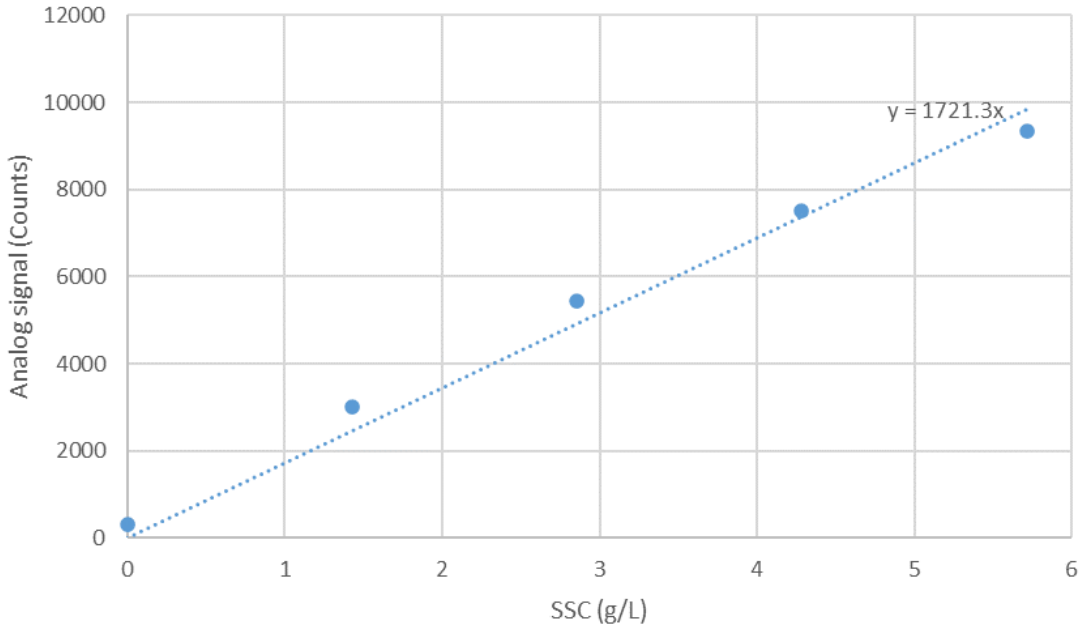

Figure 5-2: Calibration of OBS analog signal to SSC.

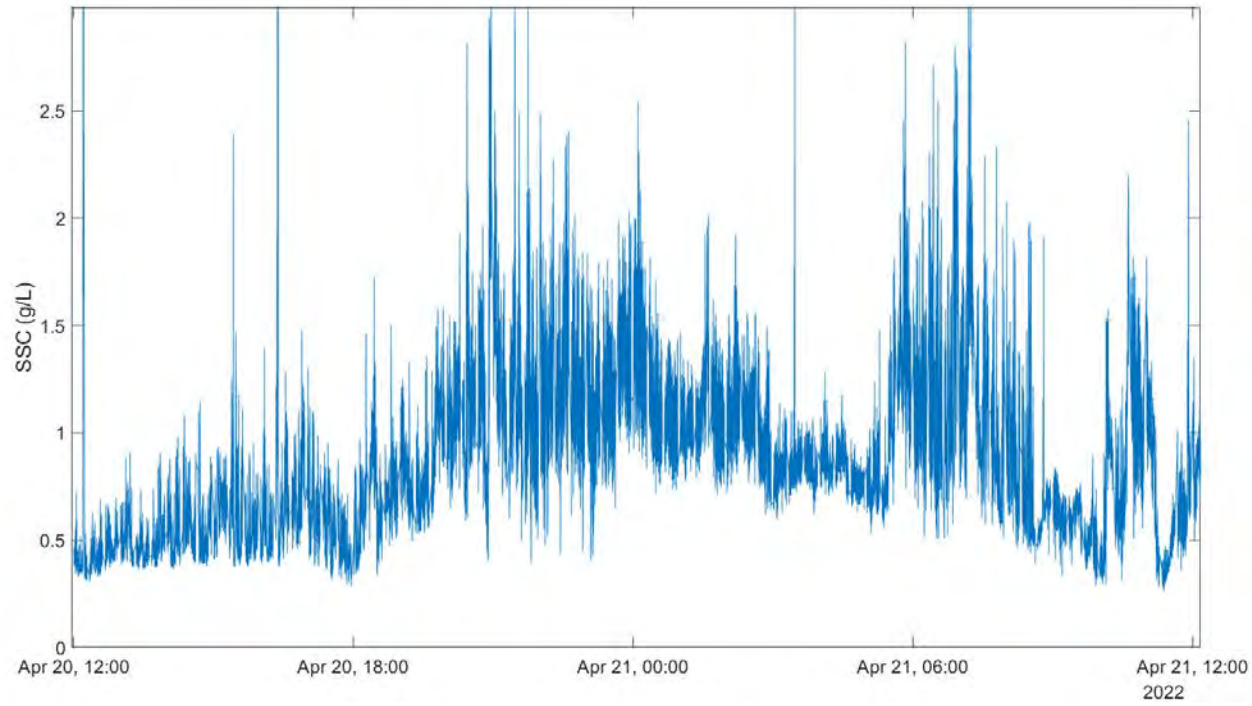

Figure 5-3 Timeseries of SSC over one day during the fixed instrument campaign.

5.4 Tributary contributions

The following summary provides quantification of water and suspended sediment fluxes (annual averages and in-situ measured) into Galveston Bay by various means including vessel-mounted ADCP and echo-sounder profiles collected as part of this project.

Based on previous work (Du et al., 2019; Dellapenna et al., 2006) of tributary inflows into Galveston Bay, average annual freshwater inflows were estimated from drainage basin sizes, total basin yields and various monitoring stations (Table 5-1). Dellapenna et al. (2006) also estimate an average annual sediment load of 4.2 x 10^6 metric tons/year from the Trinity River into Galveston Bay. Using this sediment flux and the freshwater inflow for the Trinity River, a representative average sediment concentration was determined to be 0.5 kg/m^3. Using a high-level assumption that this sediment concentration can be applied to all other tributaries, first-order approximations of sediment fluxes for all other tributaries were determined (Table 5-2). Note that differences in types of watersheds are not accounted for with this assumption. Locations of each tributary are shown via red arrows in Figure 5-4.

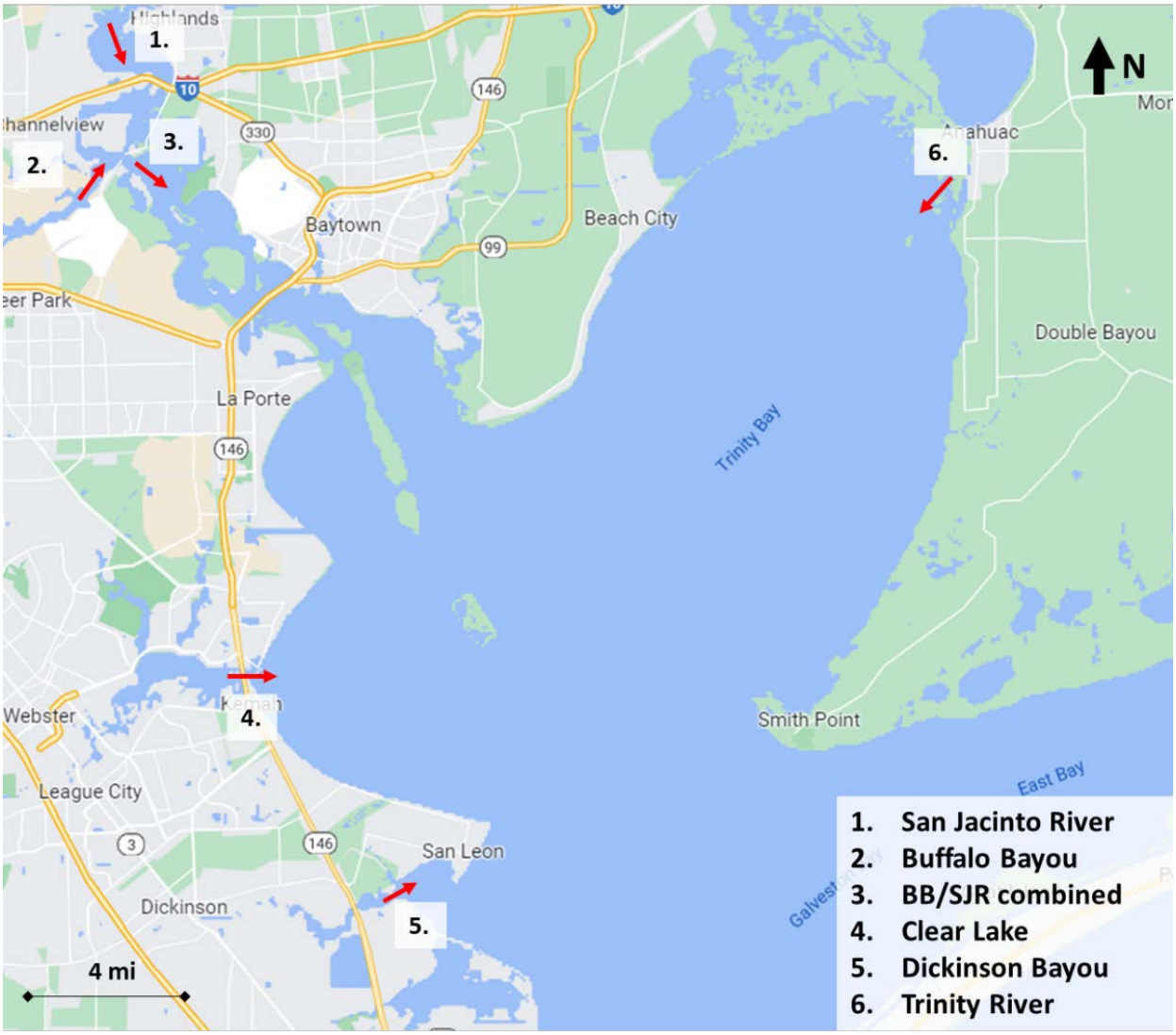

Figure 5-4: Locations of notable Galveston Bay tributaries.

Table 5-2: Freshwater inflows and resultant sediment fluxes for tributaries (Du et al. 2019).

Location	Water volume flux (m^3/s)	Sediment mass flux (kg/s)
Trinity River	271	134.13
Buffalo Bayou (BB)	14	6.93
San Jacinto River (SJR)	65	32.17
Clear Lake	67	33.35
Dickinson Bayou	34	16.88

From the estimated sediment mass fluxes given in Table 5-2, the average annual sediment load into Galveston Bay is estimated to be 7.05 x 10^6 metric tons. Du et al. (2019) found that a total sediment mass of 9.89 x 10^7 metric tons was placed into Galveston Bay by Hurricane Harvey, estimated from pre- and post-Hurricane Harvey analyses of sediment profiles and vibracores. This shows that sediment influx from Hurricane Harvey was equivalent to 14 years of average annual sediment load to the bay. Note that Du et al. (2019) found this value to be closer to 18 years, however this did not include influx from Clear Lake or Dickinson Bayou.

VM ADCP measurements outlined in Section 4-2 and Section 5-2 provided a 'point-in-time' reading of water volume discharges of these tributaries during ebb tides. Using echosounder backscatter from the instrument, SSC was inferred. This was used to determine a sediment mass flux through these tributaries, which is shown in Table 5-3 below. Since these measurements are 'point-in-time' and measured at different times/stages of tidal cycles, they cannot be compared one-to-one. Note that due to logistical and operational constraints, measurements near the Trinity River were taken near slack tide, where very low water flows were experienced.

Table 5-3: VM ADCP measurements of Galveston Bay tributaries.

Location	Water volume flux (m3/s)	Sediment flux (kg/s)	SSC (kg/m3)
Clear Lake (Ebb)	100.53	8.578	0.085
BB/SJR combined (Ebb)	83.43	0.869	0.010
Trinity River (Slack)	0.044	0.001	0.023

Sediment fluxes associated with freshwater inflows (based on average annual loads) are up to magnitudes larger than sediment fluxes measured on site during spring tidal conditions, due to the sediment concentrations for freshwater flows being a magnitude higher than for tidally induced flows. This difference is likely due to the large amount of sediment accumulated in the tributaries from runoff, which adds additional sediment to the system. Increased water flows are also expected with combined rainfall and tidal flows, leading to higher flow velocities and more erosion potential. Future field campaigns should include fixed as well as vessel-mounted velocity and SSC

measurements across all tributaries over multiple tidal cycles and flow conditions to determine more exact rating curves and sediment fluxes. Such measurements were outside the scope of this study.

6 Salinity and Sedimentation

6.1 CTD measurements

CTD measured profiles were collected using a SonTek CastAway probe at various locations along vessel tracks. Each measurement recorded profiles of conductivity, temperature, and depth readings. At each location, the continuously recording probe was cast over the side of the vessel as it descended vertically through the water column. These readings were used to determine the speed of sound in water, calculated by the CTD probe, used to aid in acoustic Doppler measurements.

A total of 18 CTD profiles were measured between 01 February and 28 April 2022, at various locations (Figure 6-1), tidal cycles, and water levels. Each profile measurement was automatically georeferenced via the integrated GPS sensor. The measured salinity and temperature profiles are given in Appendix D.

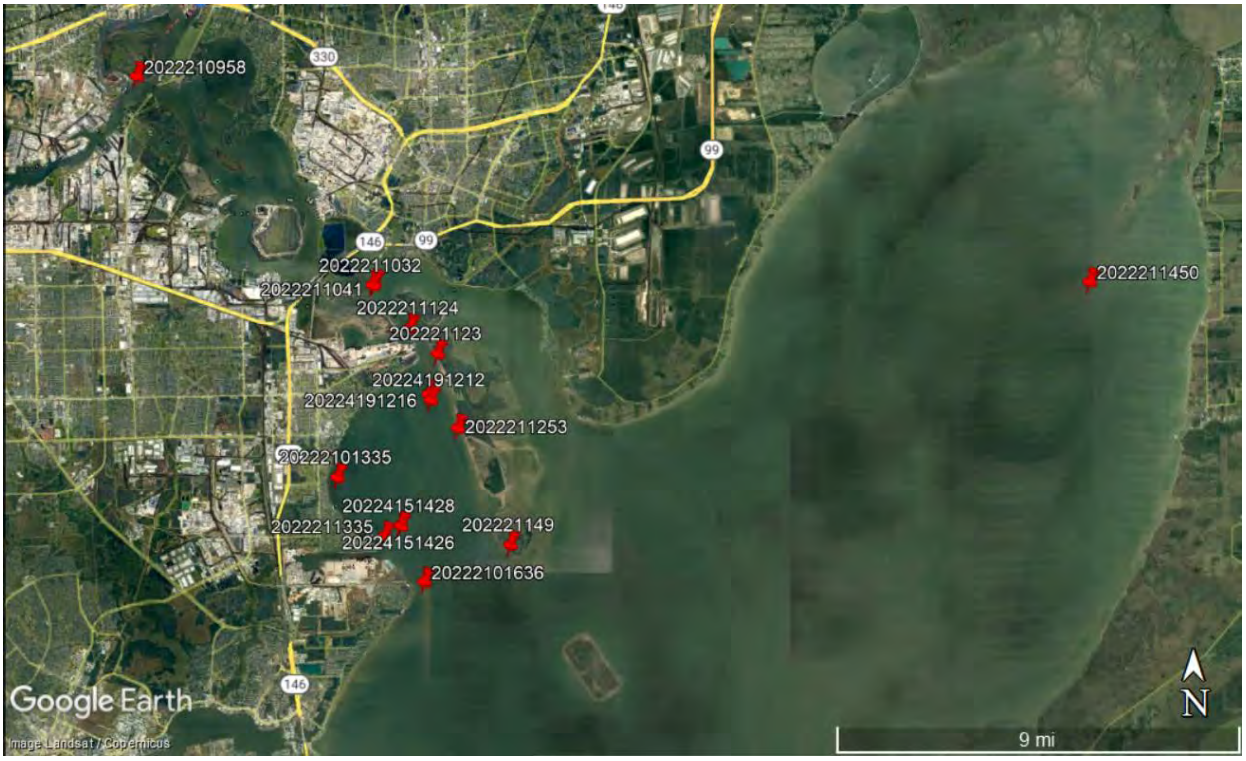

Figure 6-1: Locations of measured CTD profiles.

6.2 Settling column tests of salinity effects on sedimentation

Basic settling column experiments using bed sediment collected near the Bayport Flare at varying salinity levels have been carried out in the laboratory. While these tests cannot address all aspects driving flocculation since they are carried out under still water conditions, they do reveal the potential of the sediment particles to react with water at different salinity levels. This can provide a first-order look at the potential for enhanced flocculation driven by salinity changes. After being dried over 24 hours, a sieve analysis was conducted on the bed sediment collected to assess particle size distribution as shown in Figure 6-2. This distribution shows a median D_{50} particle diameter of approximately 120 µm and around 28% of sediment passing the No. 200 (75 µm) sieve.

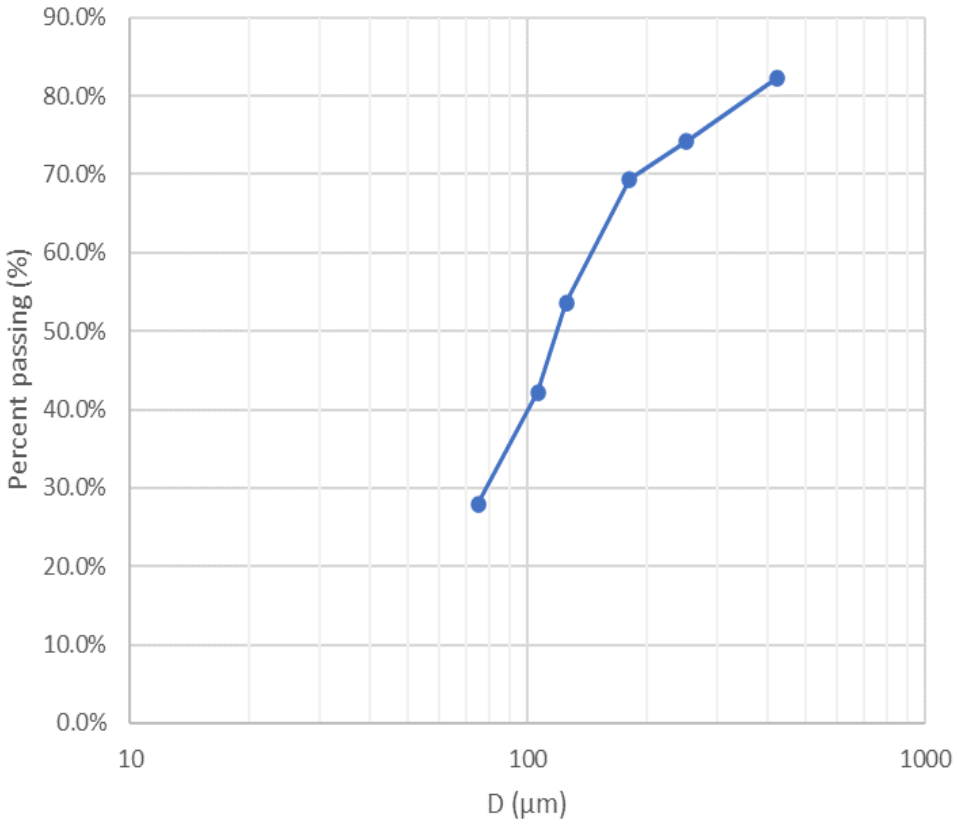

Figure 6-2: Sieve analysis results for Bayport Flare Sample.

Sediment finer than the No. 200 sieve was collected for use in the settling column tests, to prevent larger particles settling rapidly in the columns and influencing hydrometer readings. Four individual settling columns tests were conducted at constant temperature, each with different

salinities of 0, 2, 8 and 20 ppt. A specific gravity hydrometer was used to measure changes in specific gravity of the settling column over time. An initial zero reading with the hydrometer was taken before a 50 g sediment sample was added to each column and thorough mixing was conducted. Hydrometer readings were taken at 0, 0.25, 0.5, 1, 2, 4, 8, 15, 30, 60, 120 and 480 minutes for each column test, until each measurement matched the zero reading for each column. The results for each column test are shown in Figure 6-3. The 2 – 20 ppt tests show similar patterns with no discernable difference in flocculation seen. The 0 ppt test, however, shows an increase in finer particles (< 25 μm) compared to the other tests. This indicates the possibility of enhanced particle flocculation of these finer particles starting to occur above 0 ppt. Once 2 ppt of salinity are reached, no significant increase in particle flocculation above 2 ppt is observed. This is in line with findings from Wollast (1988) who found that enhanced flocculation occurs between salinities of 1 and 2.5 ppt.

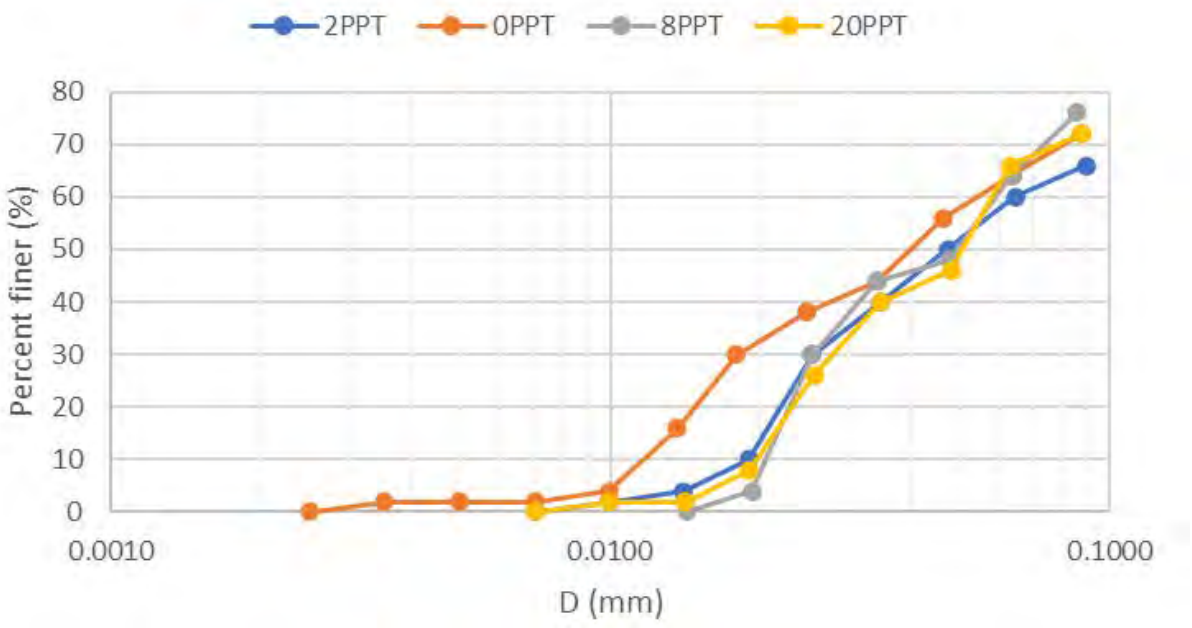

Figure 6-3: Hydrometer test results showing variations in grain size distribution for different levels of salinity.

Figure 6-4 shows the four different settling columns at approximately 1 hour after the start of the experiment. The 0 ppt test appears to be cloudier than the other three columns, indicating a higher proportion of fines still in suspension.

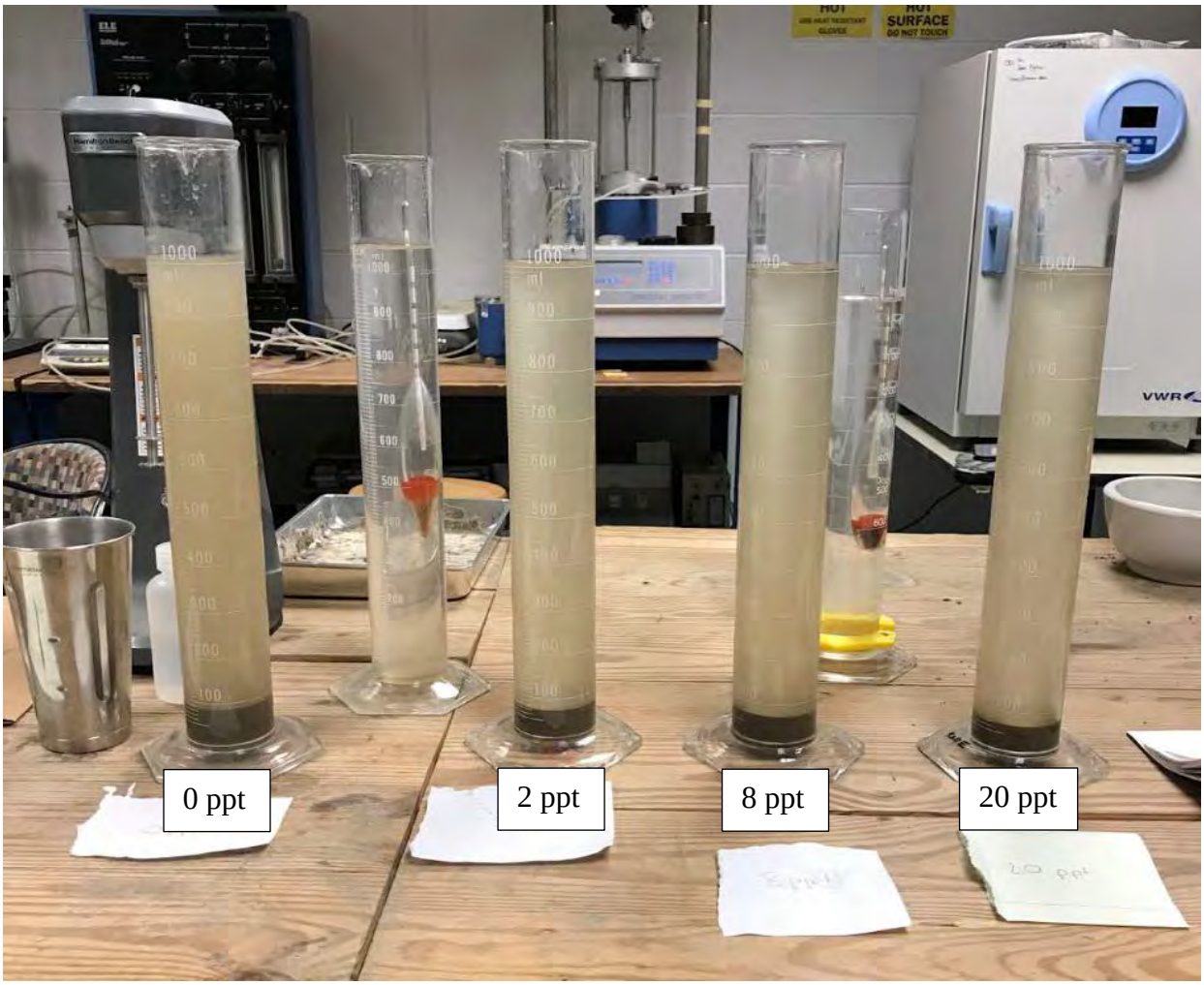

Figure 6-4: Settling columns of the four tests with increasing salinity levels from left (0 ppt) to right (20 ppt).

7 Sedimentological Study and Sediment Trend Analysis (STA)

7.1 Introduction to STA

The study area encompasses the Bayport Channel Flair which is the dredged channel junction between the Houston Ship Channel and the Bayport Channel, an area where there has been excessive channel siltation, requiring excessive channel dredging. This project is in support of an extensive numerical modeling and design study being conducted by the US Army Corps of Engineers and the Port of Houston (Figlus & Fuller, 2020; Figlus & Song, 2020). This study is providing the sedimentological input for calibration of the model. Included in this sedimentological input is the performance of a Sediment Trend Analyses (STA). The STA uses statistics generated from the grain size analyses of surface sediment to develop vector fields for sediment transport based on these statistics. This project will primarily focus on the validation of STA, which will be explored and reiterated upon based on the methodologies outlined in other prominent STA projects (Hughes, 2005; McLaren, 2016; McLaren et al., 2007; Poizot and Méar, 2010). A data gap analysis was also conducted to identify already available bed sediment data in the study area that can be used in conjunction with newly collected data to carry out STA.

STA is an empirical method that was first developed and published by McLaren and Bowles (1985), by which the behavior of sediment particles can be explained without regard to the process (McLaren, 2014). In theory, STA works by using changes in grain-size distribution parameters of bed sediment, since the size distribution of sediment can be used to determine the patterns of net transport and other dynamic properties of sediments based on five potential scenarios (McLaren & Bowles, 1985; McLaren et al., 2007). These scenarios show whether the trend of transport demonstrates dynamic equilibrium, net accretion, net erosion, or one of two total deposition sequences based on its grain size distributions, the relative probability of each particle size being transported between locations (McLaren & Hill, 2001). The grain-size distribution parameters are based on the values of mean, skewness, and standard deviation as originally described in Folk (1966), which are then compared to calculate a significance score to find dynamic transportation. There are a total of eight possible combinations of relative differences for these three parameters, only two of which can be used to determine the direction of sediment transport. See Hughes (2005) for a summary of these potential scenarios.

Furthermore, although STA has been successfully implemented in other studies, its usage is still limited and esoteric in nature. It is for this reason that this project will focus on informing the estimation, calibration, and validation of the STA method. Hence, it is hypothesized that by using STA, it was expected that the transportation vectors of sediment transport could be viably determined for the surface sediment of the surrounding Trinity Bay and San Jacinto Bay (SJB).

7.2 Study site background information relevant to STA

7.2.1 Galveston Bay overview

Galveston Bay is a turbid, shallow wave-dominated estuary, with the 3.25 km wide Bolivar Roads Inlet at its mouth. The entire Galveston Bay system, with a surface area of 1554 km^2, a mean depth of 2.46 m, and has a volume of 3.8 billion m^3 (Du et al. 2019, 2019a, 2019b), is the second-largest natural semi-enclosed estuary in the Gulf of Mexico and the seventh-largest in the United States. The Galveston Bay system contains five major sub-bays: Trinity Bay, Upper and Lower Galveston Bay, East and West Galveston Bays as well as several smaller tidal lakes, including Clear Lake, Taylor Lake, and Mud Lake (Figure 7-1).

With a tidal range of 0.5 – 0.7 m tidal, Galveston Bay is micro-tidal (Armstrong, 1982). The Texas coast experiences, on average, 20-30 cold fronts annually and on average a tropical storm makes impact once every 1.5 years (Roberts et al., 1987; Walker and Hammack, 2000). Given its small tidal range and shallow water depths, much of the water level changes are meteorologically driven primarily due the passage of cold fronts and offshore setup from southerly winds, with tidal enhancement (Solis and Powell, 1999; Ward, 1980). Wind-wave driven sediment resuspension in the bay, primarily driven by cold fronts, is dominant mechanism for sediment resuspension and transport (Carlin et al. 2016). Galveston Bay annually, receives a mean fluvial contribution of 350 $m^3\ s^{-1}$ from three major rivers, which are the Trinity River (mean discharge 271 $m^3\ s^{-1}$ in 1988-2017), San Jacinto River (mean discharge 65 $m^3\ s^{-1}$ in 2006-2017), and Buffalo Bayou (mean discharge 14 $m^3\ s^{-1}$ in 2000-2017; Du et al., 2019a). Tidal exchange with the Gulf of Mexico is low and has a mean turn overtime of 30-60 days but is dependent on both wind conditions and fluvial discharge into the bay (Solis and Powell, 1999; Rayson et al., 2016).

7.2.2 Galveston Bay subsidence and average sedimentation rates (pre-Harvey)

The greater Houston area has experienced elevated rates of land subsidence because of groundwater withdraw both for domestic as well as industrial uses (see Figure 7-1). This has resulted in up to 3 m of subsidence within the area of lower Buffalo Bayou since 1900 and 1.5-2.2 m within SJB and upper Galveston Bay (Coplin and Galloway 1999; HGSD 2013). Within the SJB, Al Mukaimi et al. (2018) found that sedimentation rates of 1.5 cm yr^{-1}, which is slightly lower than the subsidence rate. On geological timescales, estuaries are commonly considered ephemeral geomorphological features that exist during transgression (prolonged rising of sea level) where sediment fills the accommodation space created by RSLR (Weight et al., 2011). If sedimentation rates exceed the rate of accommodation space creation (surplus), the estuary will fill. As the estuary fills, the bayhead delta will prograde through the estuary and the system will transform into a river delta. Conversely, if the sediment supply cannot keep pace with RSLR (deficit), the estuary will deepen, and associated facies will transgress landward (Nichols, 1989). For estuaries to be maintained, equilibrium must exist between sediment supply, accommodation space, and RSLR (Bianchi and Allison, 2009; Day et al., 2013; Friedrichs and Aubrey, 1988; Friedrichs et al., 1990).

7.2.3 Cycling of suspended sediment within Galveston Bay

Dellapenna et al. (2022) estimated that the average sediment load for Galveston Bay is 5.45×10^6 tons of sediment. Dellapenna et al. (2006) estimated that for a typical year (e.g., 2000) that sediment resuspension due to the passage of meteorological fronts caused the resuspension of 17.9×10^6 tons of sediment, which is equivalent to 3.8 years of average Galveston Bay sediment load (Table 7-1) and that shrimp trawling between 1998 and 2001, on average, suspended 9.9×10^6 tons of sediment, the equivalent of 2.1 years of average Trinity River sediment load. Schmidt et al. (2021) estimated that in the winter/spring of 2020, that the average residence time of suspended sediment within mid and lower Galveston Bay ranged from 51-105 days. In addition, Dellapenna et al. (2022) found that Hurricane Harvey delivered 131.34×10^6 tons of sediment to Galveston Bay, equivalent to 23.9 years of the average sediment load to Galveston Bay. Collectively, these observations all suggest there is a great deal of suspended sediment transport within Galveston Bay, that the residence times of suspended sediment are relatively long and that the amount of sediment suspended and transported around the bay is multiple times higher than the average sediment load introduced to the bay.

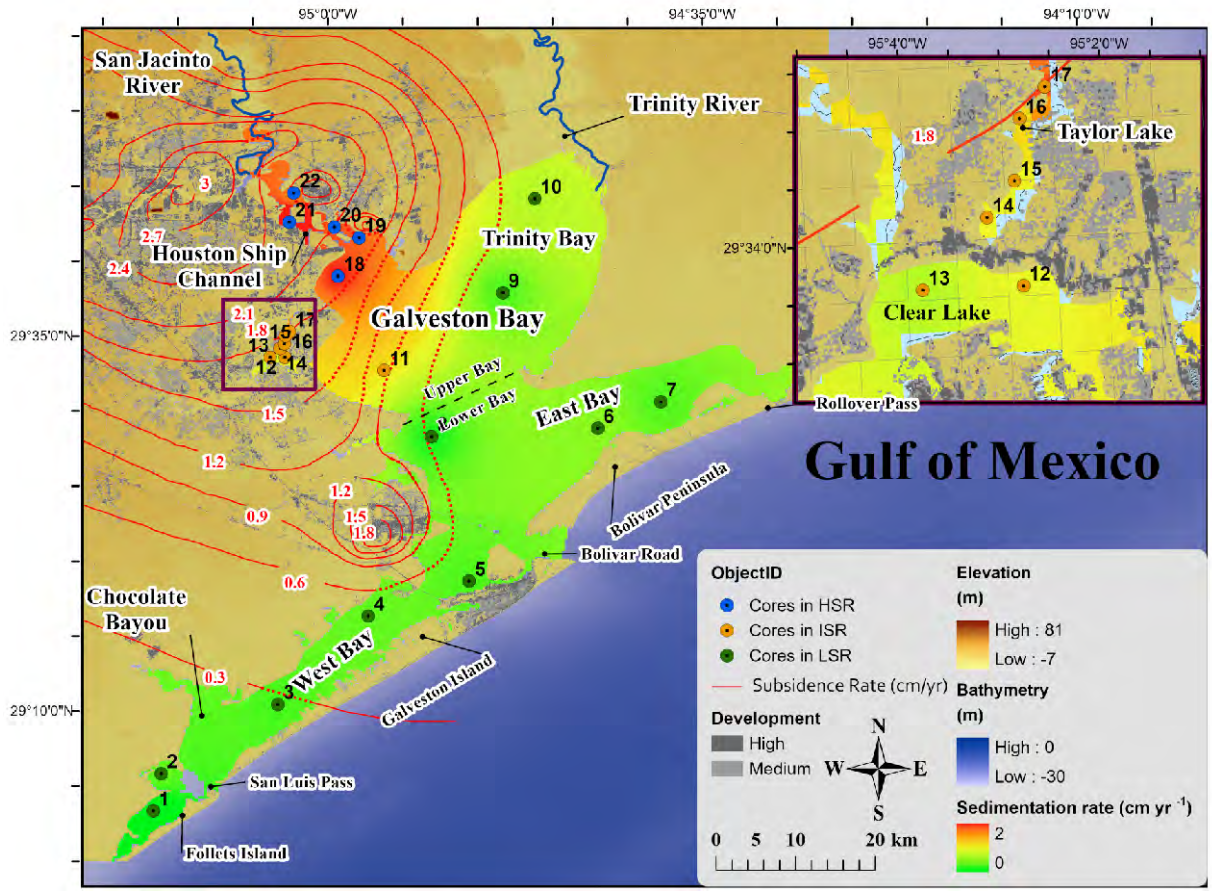

Figure 7-1: Galveston Bay subsidence and sedimentation rate map contour plot (red line) of subsidence (meters) between 1906 and 2000 (HGSD, 2008). The gray shaded area represents the Trinity River incised valley (Rodriguez et al., 2005). Note, the highest subsidence was within the San Jacinto Estuary and Buffalo Bayou, with subsidence of 2.5 – 3.0 m (~3 cm/yr) and sedimentation rates averaging 2 cm/yr indicating that although there were extremely elevated sedimentation rates, sedimentation did not keep pace with subsidence (from: Al Mukaimi et al., 2018a).

7.2.4 Hurricane Harvey

Hurricane Harvey (Harvey) struck the Texas coast 25-27 August 2017 and produced massive flooding of the Galveston Bay tributaries. The slow release of floodwaters from the Barker and Addicks Reservoirs, west of Houston, produced a 48-day flood across metro-Houston via Buffalo Bayou, through the San Jacinto Estuary, before flowing into Galveston Bay. Through the analyses of a series of 56 push cores collected across Galveston Bay, Dellapenna et al. (2022) found that Harvey deposited 131.34×10^6 tons of sediment across the bay in a deposit with an average thickness of 14 cm (Figure 7-2).

Table 7-1: Sources of suspended sediment for Galveston Bay.

Source of Suspended Sediment	Mass (tons)	Years of Average Galveston Bay Sediment Load
Wind Resuspension (2000)	$17.9x10^6$	3.8 years
Average Shrimp Trawling	$9.9x10^6$	2.1years
Average Galveston Bay sediment load	$4.24x10^6$	1.0 year
Hurricane Harvey Storm Deposit (2017)	$131.34x10^6$	23.9 years
Eroded Hurricane Harvey deposit (2017-2021)	$35.1x10^6$	6.4 years

The Trinity River delivers an average sediment load of 4.23×10^6 metric tons (Dellapenna et al. 2006) and about 77% of the fluvial input to Galveston Bay (Du et al., 2019a). Assuming that the remaining 23% of the freshwater discharge flows in with a proportionally comparable sediment load, it can be estimated that the average annual sediment load for Galveston Bay is 5.49×10^6 metric tons. A comparison of Harvey sediment deposit mass to the average annual sediment load indicates that Harvey delivered a load to the bay equivalent to approximately 31 years of the bay's average annual sediment load. The Hurricane Harvey (2017) core sites were resampled in Fall 2021 with a combination of pushcores and small gravity cores. X-radiographs were taken of each core and the thickness of the Harvey layer was estimated from each core based on physical characteristic of the sediment. Figure 7-3 shows an example of two of the cores.

The changes in core thickness were uploaded to ArcGIS for geospatial analyses and to determine overall change in the mass of the deposit (Figure 7-3). It was found that between 2017 and 2021, there was a loss in mass of the mapped Harvey deposit of $6.92x10^6$ tons, which equates to a loss of 20.3% of the original deposit mass, which is equivalent to 1.34 years of average Trinity River sediment yield. The decrease in thickness of the Harvey flood deposit over the last four years was anticipated. On average, the bay experiences 30 cold fronts, extensive shrimp trawling, which on average reworks the entire surface once per year and the impact of the passage of over 20,000 ships per year, each generating bow wakes, creating numerous erosional events per year to re-work the

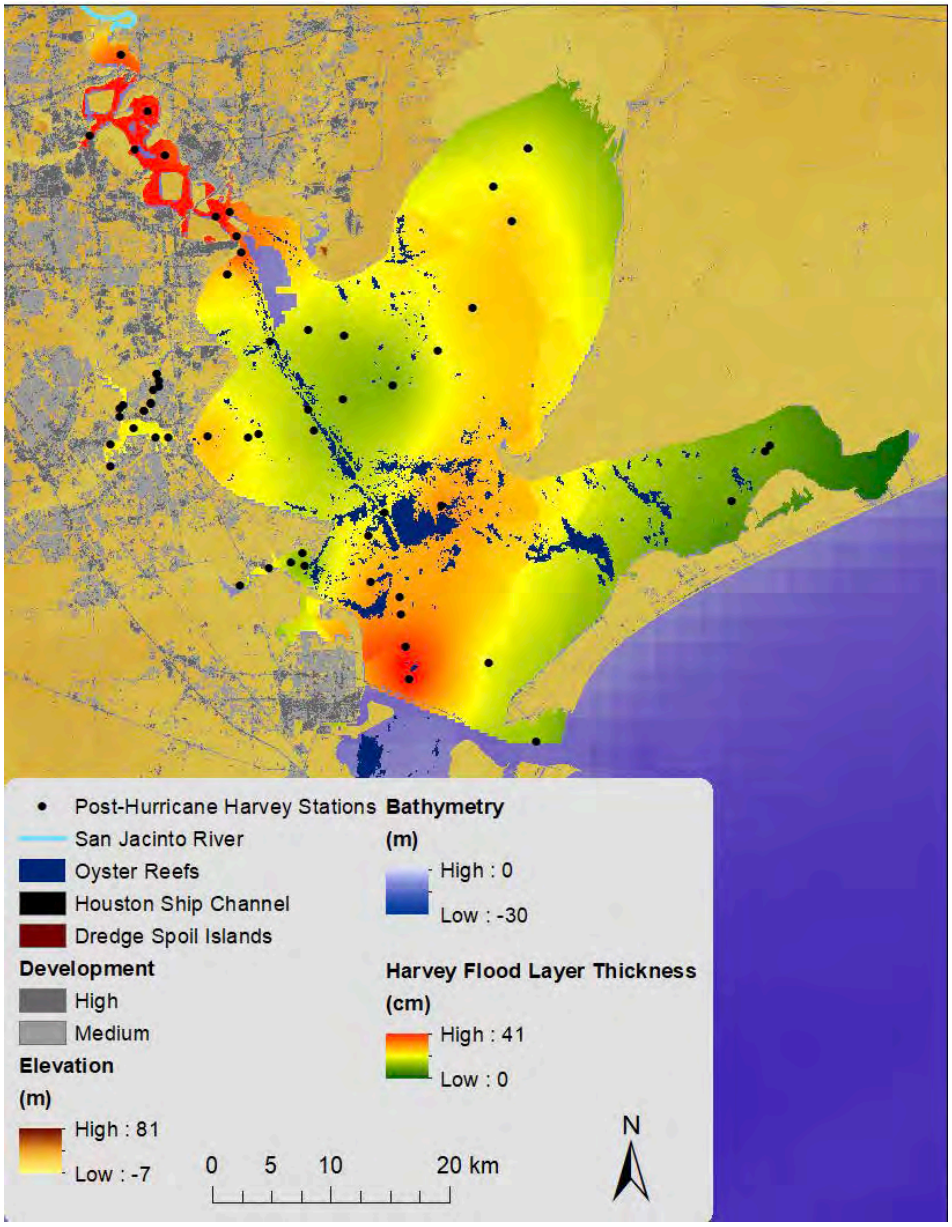

Figure 7-2: Isopach map of Harvey layer thickness in Galveston Bay. The thickest deposits were found within Clear/Bear Lake Bays, Scott and Burnett Bays, all within the San Jacinto Estuary as well as upstream of the Texas City Dike in southwestern Galveston Bay. (From Dellapenna et al., 2021).

Harvey flood layer. The greater erosion of the Harvey layer north of the Texas City Dike (Figure 7-4) is likely the combined result of an anomalously thick original flood layer and intensified wave reflection off the Texas City Dike creating a more energetic setting for the erosion of finer grained sediment. The other area where there was elevated erosion of the flood layer is in the center of the bay, primarily where the bay is narrowest between Eagle and Smith Point, and where the tidal

currents would be the greatest, due to this restriction in cross sectional area. This area is also the most exposed to winds coming from nearly any direction, with the potential for large fetch lengths. It is also shallower than other parts of the bay and due to the lack of dredge spoil islands and receives the greatest impact of ship bow wakes. Collectively, this area is the most energetic and this likely explains the enhanced erosion of the flood layer in this area.

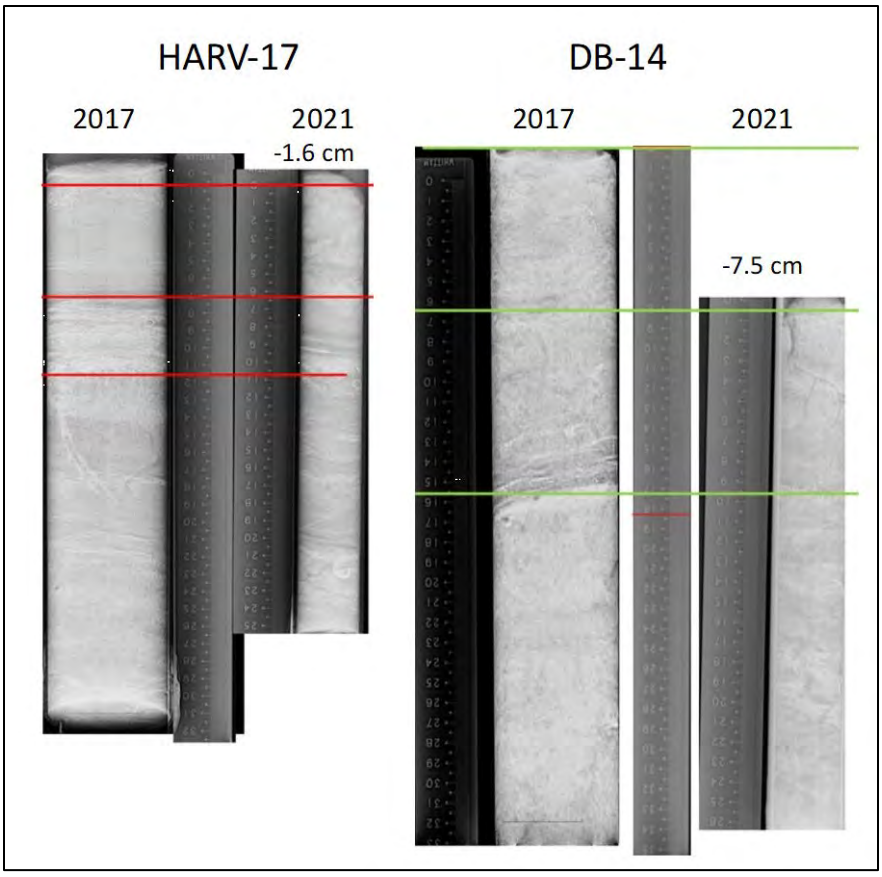

Figure 7-3: X-radiographs showing the differences in thickness of the Hurricane Harvey Flood Deposits between 2017 and 2021.

Areas of the bay where there was the least erosion of the Harvey flood layer include middle and upper Trinity Bay, San Jacinto Bay and the portion of the bay adjacent to the mouth of Clear Lake. Trinity Bay depth is generally deeper than other parts of the bay, generally deeper than 2 m, it is sheltered from winds coming from the north or south, limiting the fetch for generated waves and it is also significantly distal from the HSC, limiting the impact of bow wakes. The portion of

Galveston Bay off Clear Lake is deeper, generally greater than 3 m, is generally fetch limited for any wind direction other than from the east and is generally distal from the HSC. San Jacinto Bay is also very sheltered and, although it is closer to the HSC, there is a large shoal along the western side of the HSC, allowing for bow wakes to break before entering the bay, so in general, it is less energetic than the open parts of the bay. Taken all together, it is likely that those areas of the bay which receive the highest tidal currents, receive the greatest exposure to wind generated waves and the area most exposed to bow wakes experience the greatest erosion of the Harvey layer of the four years investigated for this study. The Hurricane Harvey storm layer thickness data that formed the basis for Figure 7-4 is provided in Appendix E.

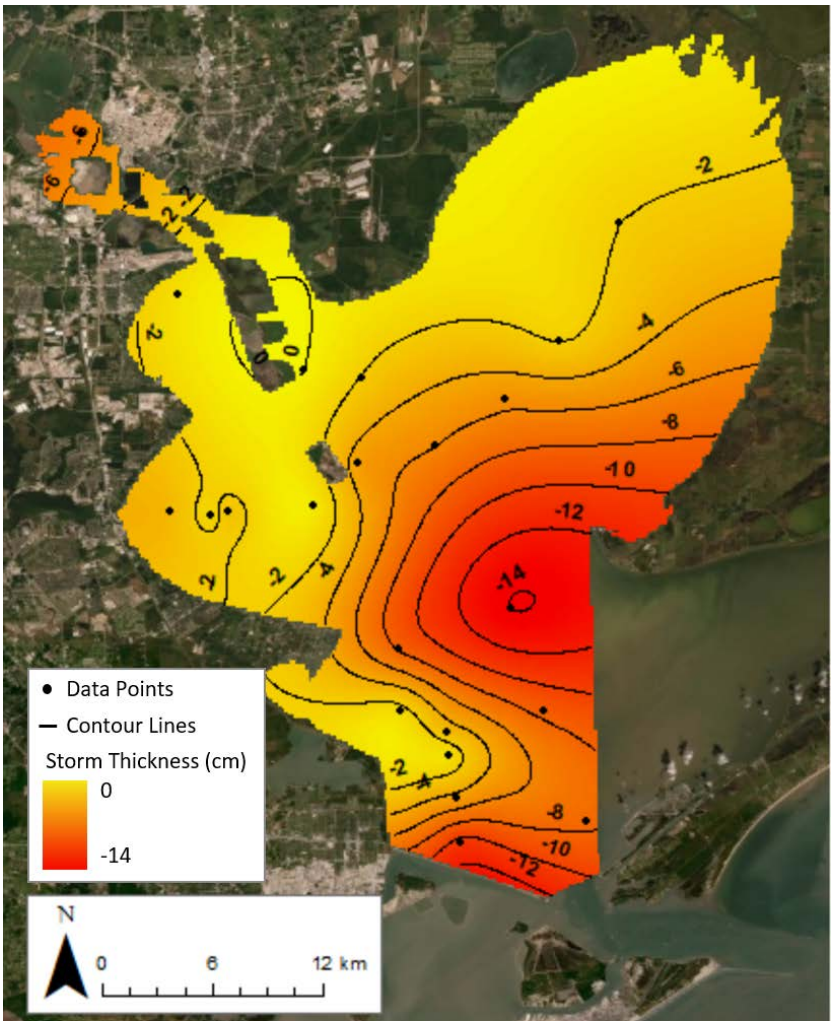

Figure 7-4: Map illustrating the overall change in thickness of the Harvey flood layer between 2017 and 2021.

7.2.5 Naturally occurring radionuclides

Short-lived radioisotope geochronology, including natural radionuclide such as ^{210}Pb ($t_{1/2}$ = 22.3 yr, Eγ= 46 KeV) and anthropogenic nuclide such as ^{137}Cs ($t_{1/2}$ = 30.2 yr, Eγ= 662 KeV), has been used extensively to investigate sedimentary processes and sedimentary records in wide variety of aquatic and marine environments including estuaries (e.g., Nittrouer et al., 1979; Santschi et al., 1999; Sharma et al., 1987; Dellapenna et al., 1998; Dellapenna et al., 2003; Yeager et al., 2004). In shallow environment, it is better to use more than one radionuclide to obtain precise information about sedimentation rates rather than relying on excess ^{210}Pb ($^{210}Pb_{xs}$) itself (Santschi et al., 1999; Jweda and Baskaran, 2011). Both $^{210}Pb_{xs}$ and ^{137}Cs are used in this study to determine the sedimentation rate in Galveston Bay and to reconstruct the historical input of mercury in the bay for the last 100 years. For both isotopes it is always assumed that it has a very short residence time in the water compared to it is half-life time and that they are absorbed into fine-grained particles (Dellapenna et al., 1998; Nittrouer et al., 1979; Krishnaswami et al., 1971).

^{210}Pb is the final long-lived radionuclide (22.4 years) in the decay of ^{238}U in the earth's crust. The decay series of ^{238}U includes ^{226}Ra, which decay to ^{222}Rn, a noble gas, which then escapes into the atmosphere at a constant rate. The Radon atoms in the atmosphere subsequently decay through a series of short-lived radionuclides to produce unsupported components of ^{210}Pb activity. ^{210}Pb is primarily removed from the atmosphere by washout of wet and dry fallout. $^{210}Pb_{xs}$ then is deposited in the snow, ice of glaciers, lakes, and oceans. The half-life time of ^{210}Pb allows the determination of sedimentation rate back 50-100 years which is about five half-life times (Baskaran and Naidu 1995; Nittrouer et al., 1979). ^{210}Po has a half-life of 138.4 days, is a daughter product of the decay of ^{210}Pb and its activity is measured as part of the ^{210}Pb age dating analyses. The goal in this study is to identify the depth where the isotopic activity of the ^{210}Pb decay series reaches a background or supported level. When new sediment is introduced, which contains "excess" activity, this excess is the activity above the supported activity. Supported activity, is the radio-activity provide within the sediment by the decay of the ^{238}U series isotopes contained within the sediment. Excess activity is in refence to the environmental labeling of ^{210}Pb series isotopes that are attached to fresh sediment which are introduced into the sediment column. It is the presence and decay of this excess activity which allows us to estimate ages. As sediment is buried, a depth will be reached where all

of the excess activity has decayed, this typically means that the sediment is older than 5 half-lives. In the case of ^{210}Pb, this would be 112 years.

7.3 Sedimentological study and STA methodology

7.3.1 Field sampling

A grid of densely-spaced locations (Figure 7-5) were sampled using a clam grab sampler or a small gravity corer called a Rocket Corer (see also Table 3-1 and Figure 3-1). For the clam grab, each sample was homogenized and placed in a labeled whirlpak bag**.** For the rocket core samples, the cores were labeled and sealed and brought back to the lab. In the lab, the upper 5 cm was extruded and homogenized and placed in a whirlpak bag. GPS locations were logged for each sample, as well as the time, date, and water depth. Sites where a sample could not be recovered after multiple tries were logged as well. These were sites either over an oyster reef or along the dredged portion of the ship channel.

7.3.2 Grain size analysis

The gathered wet samples all underwent the same process of subsampling and homogenization to create a better representation of the surface strata. For the sand and finer fraction (< 2 mm), samples were homogenized in 0.05 M sodium metaphosphate solution prior to the determination of the grain size distribution using a Malvern Mastersizer 2000 particle analyzer. The Malvern uses laser diffraction to determine grain size distributions. The Malvern produced triplicate measurements of sample grain-size distributions for each sample site, which were then averaged. Grain size distributions and statistics were exported and compiled.

7.3.3 X-radiography

X-radiographs were taken of all the split core halves at an energy level of 64 kV and exposure time of 1.6 mAS with a portable Medison X-ray source and a Varian PaxScan® Amorphous Silicon Digital Imager. X-radiographs were imported to Photoshop for tone adjustments and Powerpoint for display. The tones of the image in the x-radiograph result from the density of the material being x-rayed. In this report, more dense objects appear as lighter tones, so, clay dominated sediment will appear lighter than sand or shells.

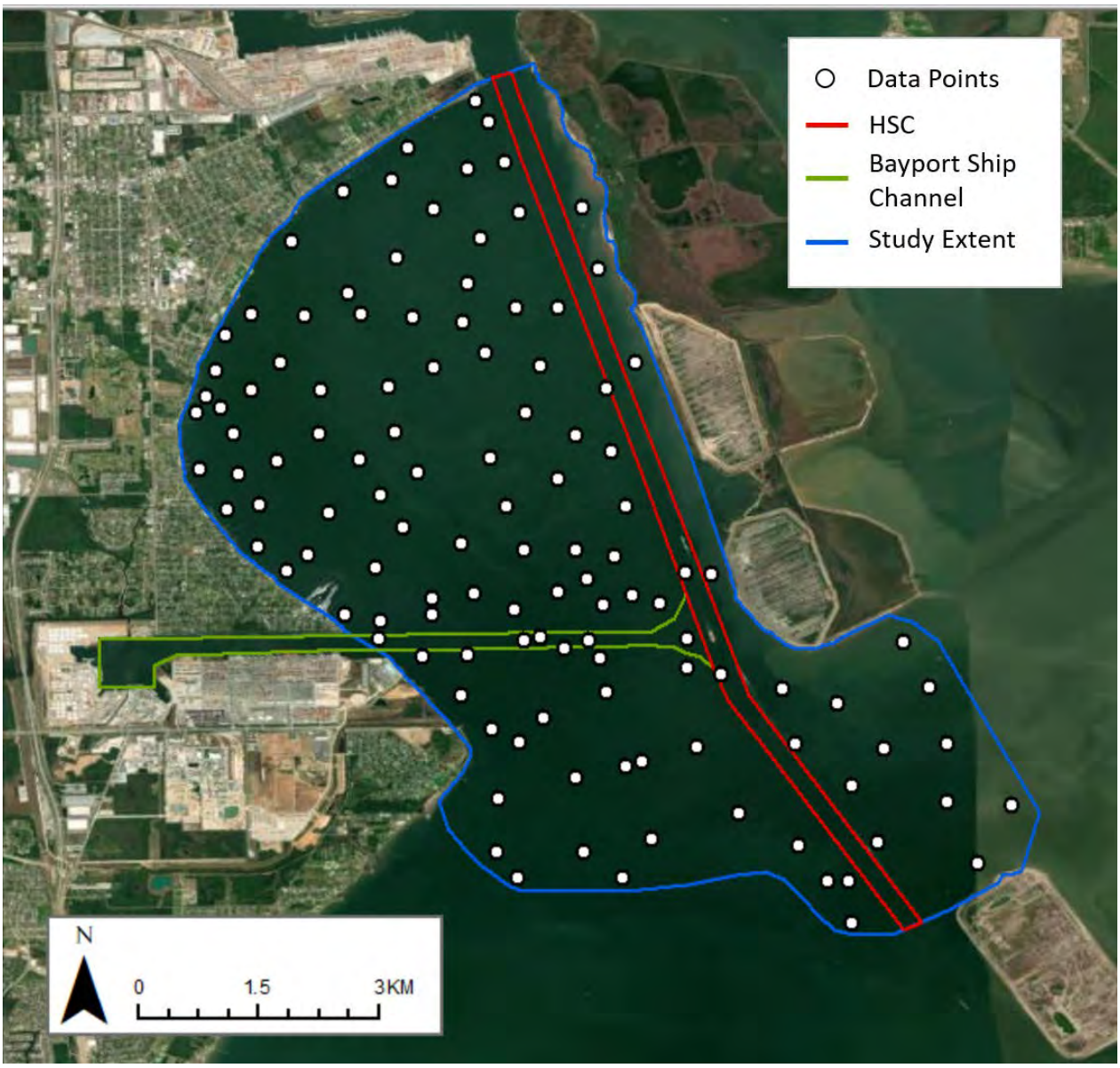

Figure 7-5: Map showing sediment sample locations used for the Sediment Trend Analysis (STA) within and around San Jacinto Bay. The Houston Ship Channel is outlined in Red. The Bayport Channel and Flare are outlined in green.

7.3.4 Determination of $^{210}Pb_{xs}$ activity concentrations

^{210}Pb activity concentrations are determined directly from its daughter radionuclide, i.e., ^{210}Po measured by alpha-spectroscopy, assuming their activity concentrations are in equilibrium. In brief, certain amounts of dried samples (~0.5 g) are digested with concentrated HNO_3 with the spike of ^{209}Po. The samples are heated at 100 ºC for 2 hrs, followed by the centrifugation to collect the supernatant for further processing. After the evaporation to incipient dryness, the samples are

dissolved by 3 M HCl solution for silver plating. Before the addition of 2 ml of 20% hydroxylamine hydrochloride and 2 ml of 25% sodium citrate, certain amount of ascorbic acid is added into the solution until the color disappears. The mixed solution is placed on an electromagnetic stirrer at 85-90°C for 4 h after the adjustment of pH to 1.5 with ammonia solution. The silver disk is rinsed with Milli-Q water and dried in the air for the measurement of ^{209}Po and ^{210}Po activities with alpha-spectroscopy. $^{210}Pb_{xs}$ is determined from total ^{210}Pb by either directly measuring the supported ^{210}Pb from following Nittrouer et al. (1979) or by taking the average activity of ^{210}Pb deeper in the core, below the depth where excess activity is found, which is the approach used in this study. Note, in this study, $^{210}Pb_{xs}$ is used simply to determine the depth at which the supported ^{210}Pb ceases to be recorded in the sediment (i.e., goes to background activities). Accumulation rates have not been calculated from the decay curves.

7.3.5 STA method

Sediment Trend Analysis (STA) was conducted using the QGIS plugin GiSedTrend (Poizot and Méar, 2010). GiSedTrend uses the relevant grain size parameters of 1) mean; 2) sorting (i.e., standard deviation); and 3) skewness, which were extracted from the outputted Malvern data sets and compiled into a singular data table (see Table A-1 in Appendix A). The data from the table were then inputted into a custom script that compared these three parameters of the closest neighboring sample locations, where the impact of a neighboring station is inversely proportional to the distance to the central location of interest. The plugin then uses the three statistical parameters to check for the existence of one of the eight possible sediment transport trend types. Previous work suggests that the two trend-type cases FB− (i.e., the grain size distribution becomes finer (F), better sorted (B), and more negatively (−) skewed) and CB+ (i.e., the grain size distribution becomes coarser (C), better sorted (B), and more positively (+) skewed) provide the best agreement with the true direction and transport (Gao et al., 1994). Because the mixing of trend cases is considered less flexible and efficient, the “exclusive or” operation was used so that only one trend case is considered at each sample location based on the highest number of cases found and the best directional homogeneity (Poizot and Méar, 2010).

7.3.6 Interpolation and cluster analysis

The relevant values needed to perform STA were prepared and uploaded into GIS and underwent interpolation to create individual contoured maps, to provide a better representation of sediment occurrence. Sample locations were plotted with additional interpreted result points along the west coast, mimicking the values of STA-224. Percent distributions of sand, silt, and clay grain size classes at each station were used to create interpolation maps of the study area. The maps were then contoured based individual minimum and maximum percent distributions for each parameter. Cluster analysis was also performed to find the most prominent types of sediment clusters based on the more detailed size distributions between very coarse sand and clay, following the Wentworth scale. Each sample was divided between both phi (Φ) and micrometers, from 15 Φ to -1 Φ, or very coarse sand to clay. These samples were processed through multivariate clustering using the K-means clustering method with optimized seed locations, with the cluster boundaries set by generated Thiessen polygons surrounding the sample sites.

7.4 Sedimentological study and STA results

7.4.1 Grain size distribution maps

Figure 7-6A-C show the Silt, Sand and Clay size distributions, respectively, with hotter to cooler colors reflecting higher to lower abundances of each size class, across the study site. Figure 7-6A shows a sand deposit along the eastern margin of the Houston Ship Channel (HSC), and additional sand deposits both at the mouth of the Bayport Ship Terminal, along just south of the Bayport Ship Channel, as well as along the western shoreline of the mainland. Figure 7-6B&C show the accumulation of silt/clay within the middle of SJB with the clay distribution mimicking the silt distribution, but with the clay dominated sediment having a narrower distribution overall. The large sand dominated area south of the Bayport channel was revealed during sample collection to contain a combination of an oyster reef and a broad distribution of gravelly oyster shell dominated sediment both north and south of the Bayport channel.

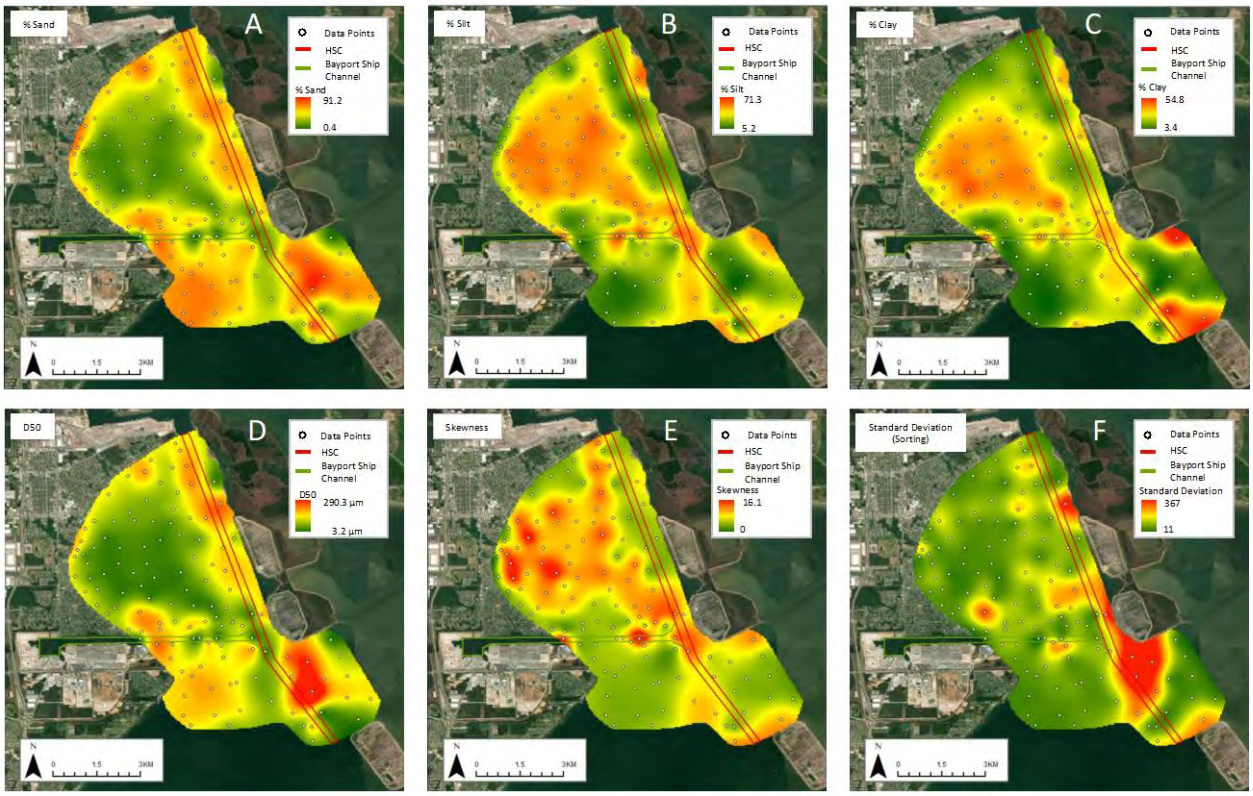

Figure 7-6: Interpolated and contoured maps demonstrating the individual percent distributions of A) % sand, B) % silt, C) % clay, D) D50 (50th percentile grain size diameter), E) Skewness, and F) Standard Deviation (sorting). For each map, the Houston Ship Channel (HSC) is shown in red, the Bayport Ship Channel is outlined in green, sample locations are shown in blue, and interpreted data points are shown in green (see text for explanation).

Figure 7-7A shows that the coarsest sediments are in the northeastern and southwestern corners of the study area, where the D_{25} consists of sand. Figure 7-7C shows that a sample from off Atkins Island in the northeastern corner of the study site has the coarsest overall sample. Skewness (Figure 7-6D) is a statistic which describes the asymmetry of grain size distributions. When Figures 7-6A-C are compared to Figure 7-6D, it is revealed that in this study, that higher skewness values tend to indicate a sediment which is has a higher silt and clay content and a lower skewness tends to indicate a sediment with a coarser size distribution. The lowest skewnesses are found along the shoal south of the HSC, along the northwestern shore of the mainland. Standard Deviation (SD) is the statistic which describes sorting. The higher the SD the poorer the sorting. The highest SD values (Figure 7-6F) tend to be found in the muddy patch in the middle of SJB within the mud dominated sediment.

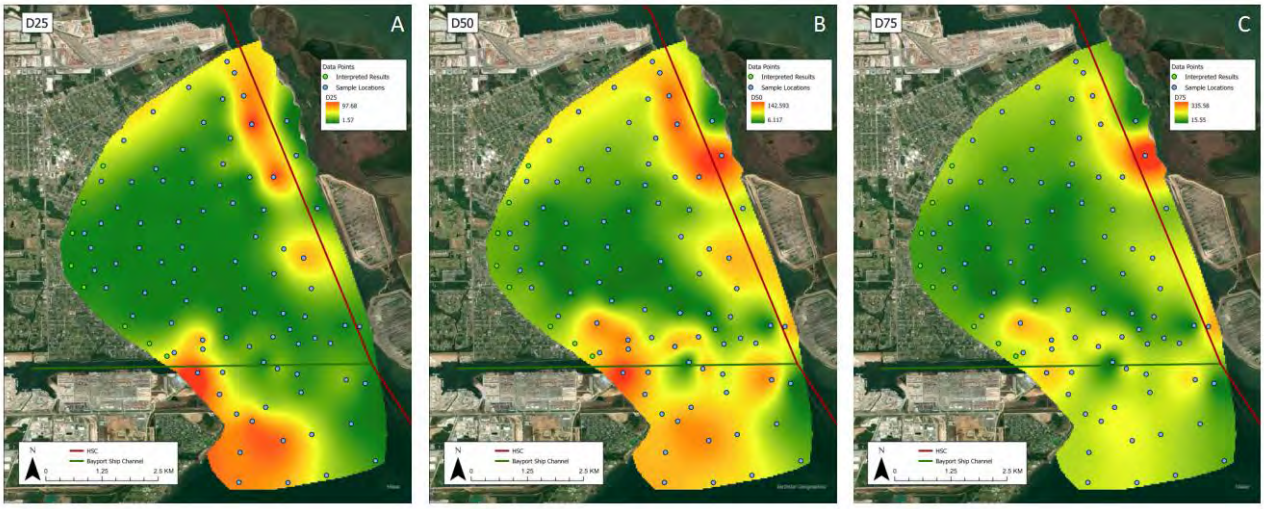

Figure 7-7: A) D25-map showing the range of the 25th percentile grain size diameter; D50- D50-map showing the range of the 50th percentile grain size diameter; D75-map showing the range of the 75th percentile grain size diameter.

7.4.2 Cluster map

The McLaren et al. (2007) approach considers the shifting of the skewness of size distribution between samples. The cluster analysis (Figure 7-8) reveals five different bottom classifications for the sediment types within the SJB, ordered and labeled from finest to coarsest mean grain-sizes. Based on Figure 7-8B, all the clusters demonstrate a bimodality, with each cluster containing both a coarser and finer size fraction. The coarser samples contained between 5-10% silt to clay grain sizes fractions and even the clay cluster contained nearly 15% very fine sand (greater than 63µm). Overall, the clusters show that the center of SJB is occupied by the Clay cluster with Coarse Silt and Fine Sand clusters found along the perimeter of the Clay cluster. Clusters of Clay and Fine Sand are also found along both navigation channels. The remainder of the study area occupies the Very Fine Sand Cluster.

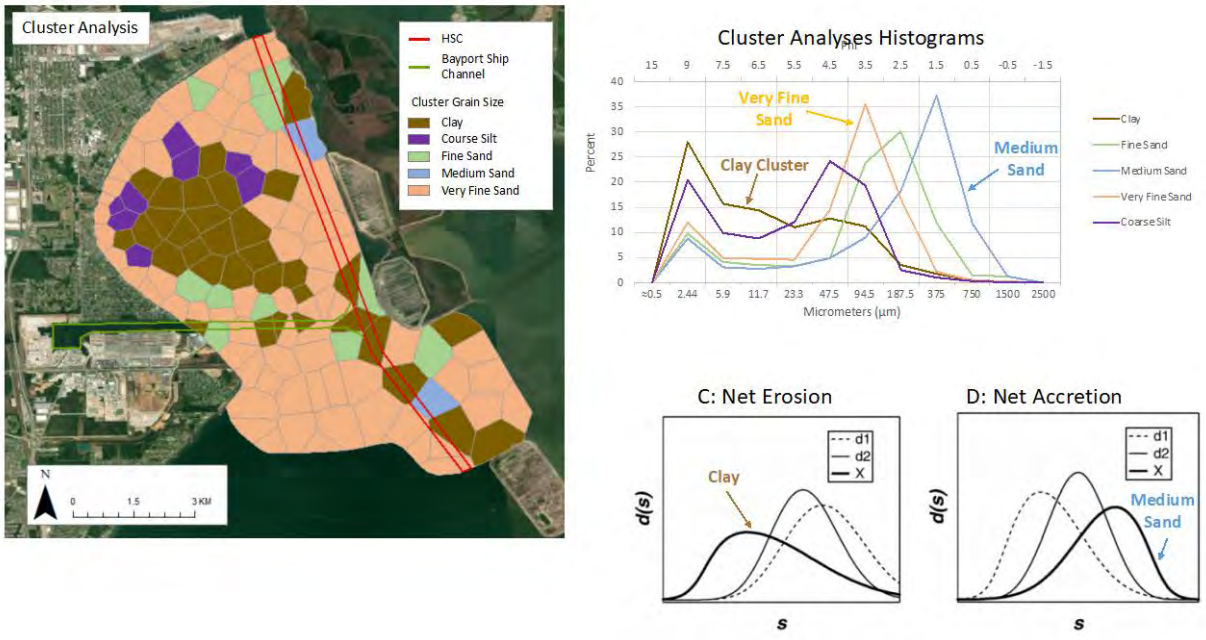

Figure 7-8: A) Cluster Map; B) Cluster Analyses Histogram showing the Very Fine Sand Cluster as the Reference Cluster; C) Example of size distribution from McLaren et al. (2007) showing example of cluster analyses for net erosion; and D) for net accretion.

7.4.3 STA results

Figure 7-9 shows the results of the STA. The left panel of Figure 7-9 shows the vector field as lighter arrows, with the darker, bold arrows showing the vectors for the actual samples. The right panel of Figure 7-9 shows only the interpolated transport vector field without the bold arrows. It should be noted that the STA results are a time averaged depiction of sediment transport as such, it shows overall trends as interpolated from the algorithm. A few general trends fall out, 1) shoreline erosion along the western margin of SJB, as indicted by arrows pointing eastward from the western shore; 2) transport and influx from above Morgan Point towards SJB; 3) transport from Trinity Bay through the passage between Atkinson Island and Bluewater Atoll and transport up the bay from south of the Bayport Flare; 4) overall convergence in transport towards the center of SJB just northwest of the Bayport Flare. Based on the sediment trends indicated in the STA, although there appears to be significant sediment transport southward from Morgan Point, it appears that the dominant source of sediment impacting the Bayport Flare is coming from the south and southeast, mainly being transported through the passage between Atkinson Island and Bluewater Atoll.

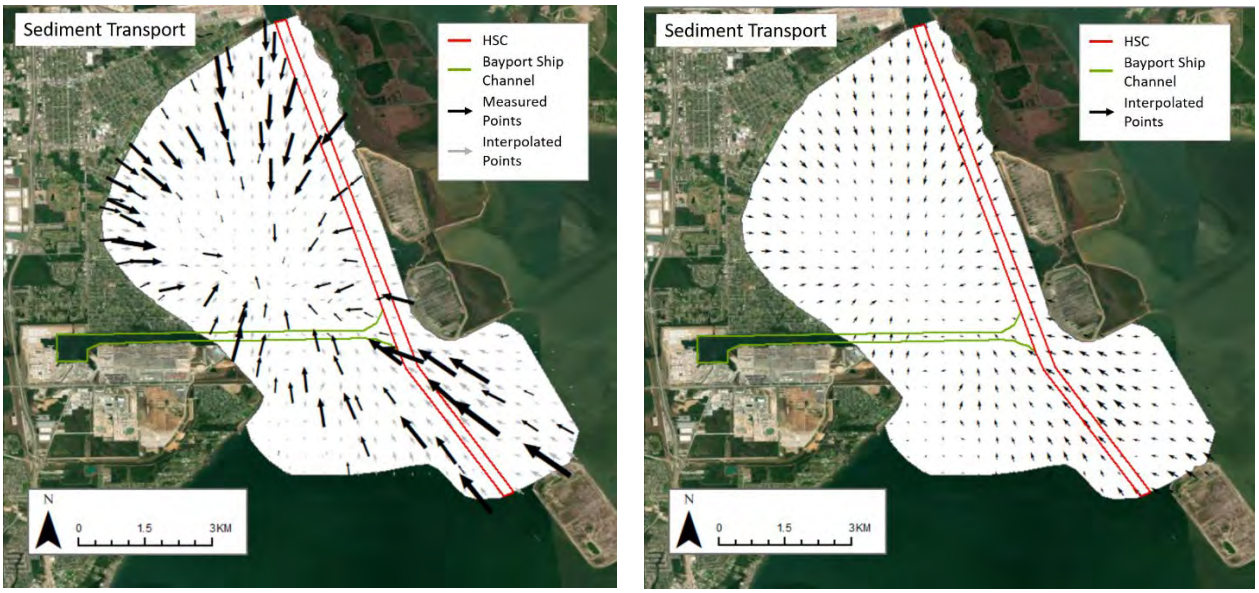

Figure 7-9: Sediment Trend Analyses (STA) results with larger sediment transport vectors for sample sites (left panel) and interpolated transport vector field over the project area (right panel).

7.4.4 Core results

Excess ^{210}Pb analyses were run on four cores from within the study area. Regression analyses of the excess activities of the cores for depth profiles provide an estimate of the average decadal sediment accumulation rates. These data reveal accumulation rates are 2.8 cm/y for the northern end of SJB, 2.4 cm/y for the middle of SJB and 2.6 cm/y for the southern end of SJB, just north of the Bayport channel. In contrast, the accumulation rate east of Atkinson Island is 1.2 cm/y (Figure 7-10).

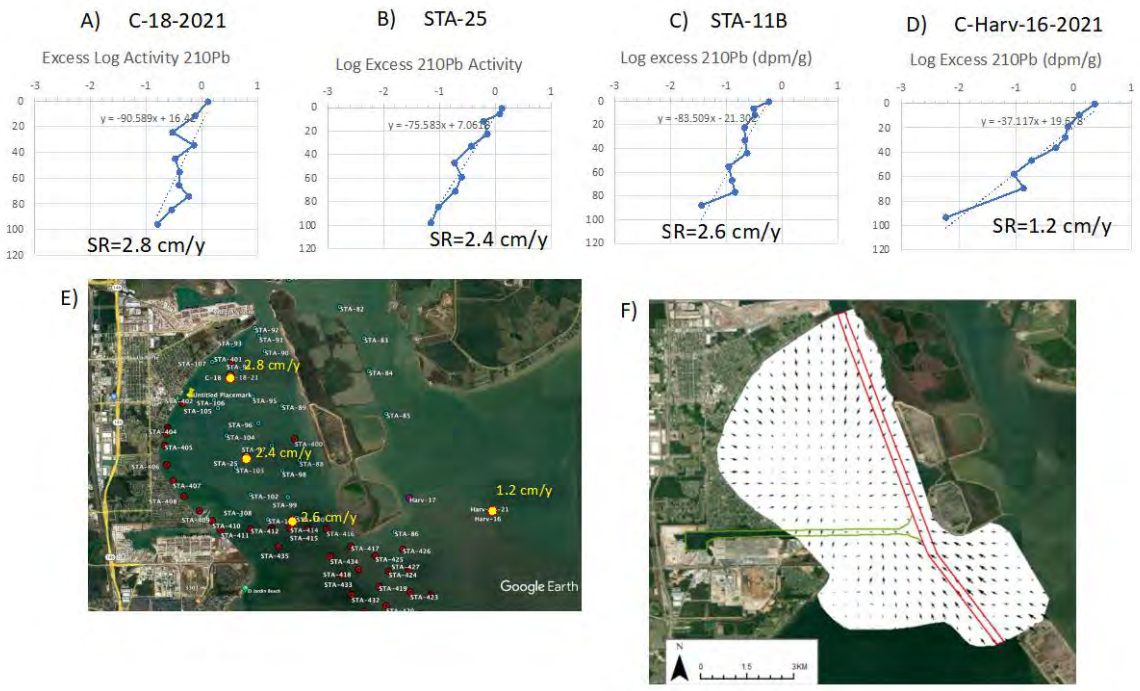

Figure 7-10: A-D) Excess 210Pb profiles showing sediment accumulation rates. E) Base map showing location of the cores as well as their respective sediment accumulation rates. F) Sediment Trend Analyses vector map showing convergence of sediment transport within San Jacinto Bay.

7.5 Sedimentological study and STA discussion

Al Mukaimi et al. (2018) found that the extremely high rate of subsidence for the eastern side of Metro-Houston and upper Galveston Bay, including lower Buffalo Bayou, and the San Jacinto Estuary is continually creating accommodation space for sediment to accumulate. For upper Galveston Bay and the San Jacinto Estuary, the sedimentation rates prior to Hurricane Harvey were approximately half of the subsidence rates, so, there was a sediment deficiency, likely resulting from the combined factors of the extremely high subsidence rates and the reduction of sediment input due to the installation of the Lake Houston dam on the San Jacinto River, located 44 river km upstream of Morgan Point.

Subsidence rates for SJB average 2 cm/y, as noted above, this subsidence rate is approximately 10 times higher than would be expected due to eustatic sea level (global) rise rates (Al Mukaimi et al., 2018) and for estuaries with sufficient sediment influx, sedimentation rates within estuaries on the

decadal to millennial time scale tend to approximate relative sea level rise rates. If the rates are higher, then fill in and convert to a delta. Dellapenna et al. (2022) found that Hurricane Harvey deposited 131.34×10^6 tons of sediment across the bay in a deposit with an average thickness of 14 cm, which is equivalent to 31 years of average sediment load from the Trinity River. This deposit more than compensated for the sediment deficit that was reported by Al Mukaimi et al. (2018) due to the extremely elevated subsidence.

Cores collected in this study, where the original Hurricane Harvey coring sites were re-occupied, found that in general, there has been a 20.3% loss of the Hurricane Harvey deposit, most of which is likely due to erosion (as opposed to sediment consolidation). Assuming that all the volume loss was due to erosion, then, overall, there was 35.1×10^6 tons eroded, which is equivalent to 8.28 years of average Trinity River sediment yield. Figure 7-11 shows the STA vector map plotted atop the Hurricane Harvey deposit change map. What is notable is that the STA vector map shows the strongest vectors originating from the southeastern corner of the study site, approximately 2.5 km northwest of the area where the greatest erosion of the Harvey deposit was found. This area of elevated erosion of the flood layer is in the center of the bay, and as noted above, this area includes the area where the bay is narrowest between Eagle and Smith Point, and where the tidal currents would be the greatest, due to this restriction in cross sectional area. This area is also the most exposed and for winds coming from nearly any direction, is where the fetch would be the greatest. It is also shallower than other parts of the bay and due to the lack of dredge spoil islands receives the greatest impact of ship bow wakes. Collectively, this area is the most energetic and this likely explains the enhanced erosion of the flood layer in this area. It is reasonable to assume that irrespective of the Harvey flood deposit, that in general, this area is a primary source of sediment resuspension within the bay. On average, the bay experiences 30 cold fronts per year as well as extensive shrimp trawling, which on average reworks the entire surface once per year and the impact of the passage of over 20,000 ships per year, each generating bow wakes, creating numerous erosional events per year to erode the Harvey flood layer from the central bay erosional area.

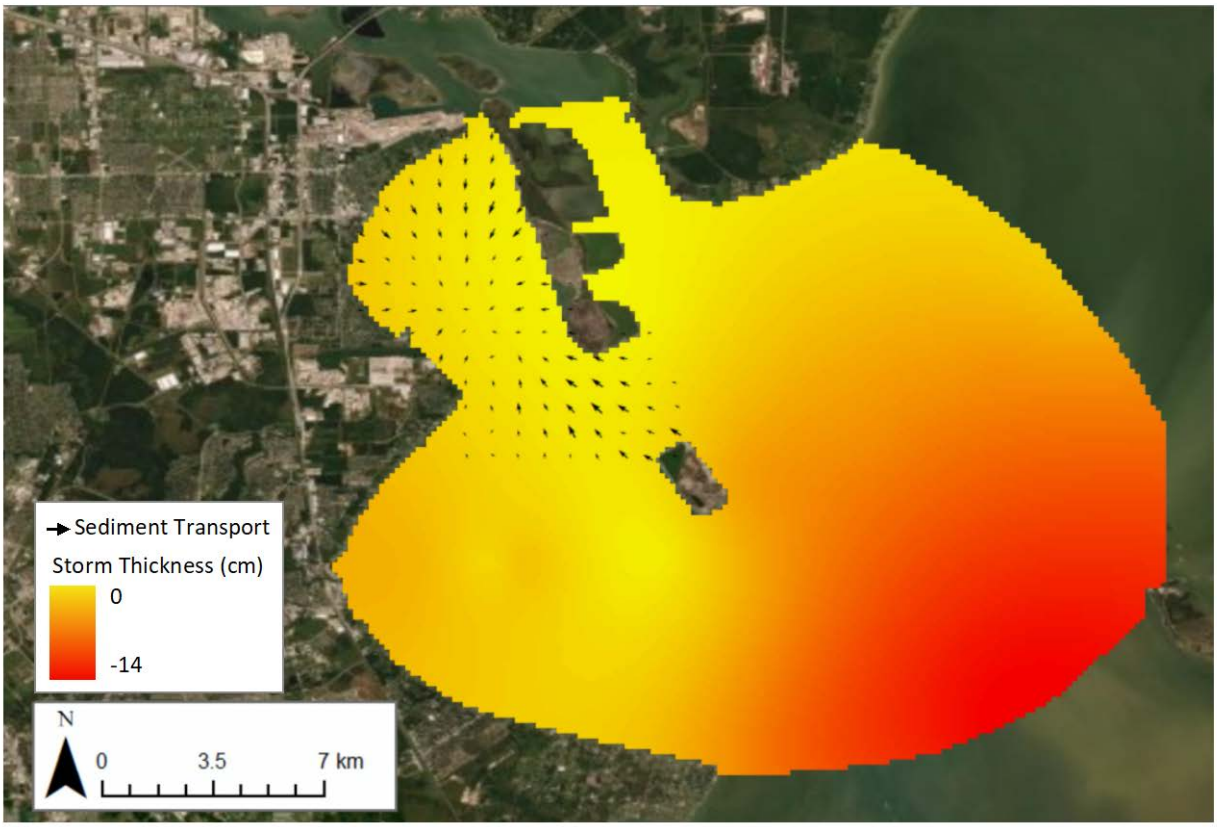

Figure 7-11: Sediment Trend Analysis (STA) transport vector map plotted atop a portion of the Hurricane Harvey Deposit Change map.

The suspended budget for Galveston Bay for both Pre- and Post-Harvey is summarized in Table 7-2. As discuss previously, Galveston Bay has multiple sources of suspended sediment, including fluvial input from its tributaries, most notably, the Trinity River, but also the San Jacinto River, Buffalo Bayou, Clear Creek and Dickinson Bayous, which have a combined annual load of, 5.49 $x10^6$ tons of sediment Dellapenna et al., 2022; Du et al., 2019). In addition, there is wind driven wave resuspension, shrimp trawling, and ship wake resuspension. Ship wake resuspension has yet to be quantified but is likely at least comparable to shrimp trawling, so will be considered for the budget as contributing the equivalent amount. Taken together, the total suspended sediment load is $43.2x10^6$ tons per year, or 7.9 years of average Galveston Bay sediment load. If the average sediment load from the erosion of the Harvey deposit is considered, then the total load becomes

$78.3x10^6$ tons, which is equivalent to 14.3 years of average Galveston Bay sediment load. It should be noted here that tidal current sediment resuspension is not considered here and so would be an additional load, making the entire load even higher.

Table 7-2: Suspended sediment budget for Galveston Bay pre- and post-Harvey.

	Pre-Harvey	***Post-Harvey***
Source of Suspended Sediment	**Mass (tons) per year**	**Mass (tons) per year**
Average Galveston Bay	$5.49x10^6$	$5.49x10^6$
Wind Resuspension (2000)	$17.9x10^6$	$17.9x10^6$
Average Shrimp Trawling	$9.9x10^6$	$9.9x10^6$
Average Ship wake Resuspension (estimated)	$9.9x10^6$	$9.9x10^6$
Eroded Hurricane Harvey deposit (2017-2021)	n/a	$35.1x10^6$
Total Suspended Sediment Load	$43.2x10^6$	$78.3x10^6$
Years of Average Galveston Bay Sediment Load Equivalent	7.9 years	14.3 years

In addition to these loads, the estimate of the sediment mass loss of the Harvey deposit, which is equivalent to an additional 6.39 years of average Galveston Bay sediment load and for each of the four years since, the average sediment load of the eroded Harvey deposit was equivalent to 1.6 years of average Galveston Bay sediment load. The average suspended sediment load due to the erosion of the Harvey deposit brings the total average suspended sediment load for Galveston Bay to be 9.29 years of average Galveston Bay sediment load, which in mass is $35.1x10^6$ tons of sediment or 27% of the Hurricane Harvey sediment load. This means the suspended sediment load in Galveston Bay in 3.74 years is equivalent Galveston Bay sediment load of Hurricane Harvey deposited within the bay. Although, exteme flood events such as Harvey deliver significant volumes of sediment to the bay, even during non-flood years, there is an abundeance of sediment moving around within the bay. Consequently, for periods of time between major floods, the

question of where in the drainage basin the sediment is sourced is almost irrelevant. The question should be, where in the bay is the sediment resuspended and where in the bay is it deposited. The results of the STA analyses suggest that the major sediment pathway for sediment moving into the Bayport Flare and SJB is from the southeast, mainly from the passage between Atkinson Island and Bluewater Atoll as well as directly south of SJB (Figure 7-11). The areas of the most intense erosion of the Hurricane Harvey deposit are the likely source of most of the suspended sediment transported into the SJB and the Bayport Flare. The extremely elevated sedimentation rates within SJB suggests that SJB is a major sediment sink and is located adjacent to the Bayport Flare.

8 Summary and Conclusions

Following a data gap analysis, an extensive field data collection campaign was completed as part of this project to help quantify sediment processes in Galveston Bay around the Bayport Flare area. Collected and analyzed data include surface sediment grab samples, gravity core and vibra core samples, water samples, and CTD information. Furthermore, in-situ deployments of ADCP, PT, TCM, and OBS systems were completed under energetic wave conditions during an entire spring tidal cycle. Vessel-mounted ADCP measurements along 27 survey tracks were completed as well, including tracks co-located in time and space with the in-situ measurements. Bed sediment samples were analyzed for grain size statistics and formed the basis for a sediment trend analysis (STA) of the immediate project area. Hydrodynamic measurements were used to compute water level fluctuations, determine circulation patterns, and assess suspended sediment concentrations. Tributary influx assessments were made using previously published data as well as data from vessel-mounted ADCP transects across tributary inlets to Galveston Bay. Additional laboratory tests related to salinity effects on sedimentation were carried out using simple settling column setups. Raw and post-processed data were made available to the sponsor and remain accessible for further analysis. The data and analyses contained in this report are intended to inform numerical modeling efforts and the design of mitigation strategies to limit the sedimentation issues at the Bayport Flare.

The following conclusions can be drawn from analysis of the measured data:

- Analyses of the Hurricane Harvey deposit revealed that the deposit is decimeters thick and persistent. STA analysis requires synoptic (temporally constrained) sampling of a densely spaced grid of surface sediment samples. The conducted data gap analysis of existing historic sources of information underscored that such data did not exist prior to this study. Additionally, the annual suspended sediment budget within the bay is orders of magnitude greater than the suspended load coming in from the tributaries, indicating that gap analyses to discern drainage basin sediment sources would provide virtually no relevance to our understanding of the system. The needed sediment data collection effort was accomplished as part of this project.

- Flow circulation and sediment movement patterns in the project area are influenced by tidal fluctuations, wind stress, wave action, tributary influx, and ship dynamics (i.e., vessel wakes and propeller wash). Considering only residual currents based on tidal forcing will lead to misinterpretation of the circulation patterns that drive sediment movement in the project area. Especially the effect of wind, waves, and ship wakes on sediment transport should be considered when designing mitigation measures.
- Tributary influx of water and sediment do provide source material for sedimentation in the Bayport Flare area. However, the large quantity of fine sediment carried into Galveston Bay during Hurricane Harvey in 2017 and deposited predominantly in areas surrounding the project area adds to the dynamics of sediment movement into the project area to this day. In fact, a major portion of the sediment accumulating in the Bayport Flare likely originates from areas south and southeast of the flare where reduction in the Harvey deposit layer thickness is still active, creating a source of sediment for the siltation at the Bayport Flare.
- Settling column tests at different salinity levels revealed that a slight increase in flocculation activity occurs between 0 – 2 ppt salinity levels with flocculation activity being higher at 2 ppt compared to 0 ppt. There is no significant change in flocculation activity above 2 ppt and the slightly higher flocculation activity is maintained at a constant level as salinity increases further. While these tests cannot address all aspects driving flocculation since they are carried out under still water conditions, they do reveal the potential of the sediment particles to react with water at different salinity levels. Salinity effects on sedimentation in the Bayport Flare area are likely minimal because typical salinity levels are well above 2 ppt in Galveston Bay, i.e., a transition from below 2 ppt to above 2 ppt in salinity rarely occurs. However, a large influx of freshwater into the bay could lead to a situation where salinity levels between 0 and 2 ppt are possible.
- The Sediment Trend Analysis (STA) revealed that the portion of Galveston Bay called San Jacinto Bay, which includes the Bayport Flare area is a sediment sink with sediment transport toward it from all sides (even though transport from the south and southeast seem to dominate). The elevated subsidence rate averaging 2.0 cm/yr in San Jacinto Bay coupled with the sedimentation rate over 2.6 cm/yr demonstrates a high convergence of sediment to this area. Sediment in San Jacinto Bay is available for resuspension by various means

but once sediment moves into the channel, resuspension is more difficult due to the large depth compared to the nearby shallow areas. This leads to enhanced sedimentation in the Bayport Flare and needs to be considered when designing mitigation measures.

- The combination of tide-, wind-, and wave-driven circulation coupled with the STA analysis results show that the Bayport Flare area is a preferred location for sediment deposition.

Analyses of collected data will continue in the future and any updates to the above findings will be made available.

9 References

Al Mukaimi, M. E., Dellapenna, T. M., and Williams, J. R. (2018). Enhanced land subsidence in Galveston Bay, Texas: Interaction between sediment accumulation rates and relative sea level rise. *Estuarine, Coastal and Shelf Science*, *207*, 183–193. https://doi.org/10.1016/j.ecss.2018.03.023.

Armstrong, N.E. (1982). Responses of Texas estuaries to freshwater inflows. In *Estuarine Comparisons* (pp. 103-120). Academic Press. https://doi.org/10.1016/B978-0-12-404070-0.50013-2.

Baskaran, M. & Naidu, A. S. (1995). 210Pb-derived chronology and the fluxes of 210Pb and 137Cs isotopes into continental shelf sediments, East Chukchi Sea, Alaskan Arctic. *Geochimica et Cosmochimica Acta*, 59(21): 4435–4448. https://doi.org/10.1016/0016-7037(95)00248-X.

Bianchi, T. S. & Allison, M. A. (2009). Large-river delta-front estuaries as natural "recorders" of global environmental change. *Proceedings of the National Academy of Sciences*, 106(20): 8085–8092. https://doi.org/10.1073/pnas.0812878106.

Cao, Z., Pender, G., and Meng, J. (2006). Explicit Formulation of the Shields Diagram for Incipient Motion of Sediment. *Journal of Hydraulic Engineering*, *132*(10), 1097–1099. https://doi.org/10.1061/(ASCE)0733-9429(2006)132:10(1097).

Carlin, J. A., Lee, G., Dellapenna, T. M., and Laverty, P. (2016). Sediment resuspension by wind, waves, and currents during meteorological frontal passages in a micro-tidal lagoon. *Estuarine, Coastal and Shelf Science*, 172, 24-33. https://doi.org/10.1016/j.ecss.2016.01.029.

Coplin, L.S. & Galloway, D. (1999). Houston-Galveston, Texas Managing coastal subsidence, in: Galloway, D., Jones, D.R., Ingebritsen, S.E. (Eds.), Land subsidence in the United States. *U.S. Geological Survey Circular* 1182, pp. 35-48.

Day, J.W., Yanez-Arancibia, A., and Kemp, W.M. (2013). Human impact and management of coastal and estuarine ecosystems, in: Day, J.W., Crump, B.C., Kemp, W.M., Yanez-Arancibia, A. (Eds.), Esturine ecology, 2 ed. John Wiley and sons, New Jersey, USA.

Dellapenna, T. M., Allison, M. A., Gill, G. A., Lehman, R. D., and Warnken, K. W. (2006). The impact of shrimp trawling and associated sediment resuspension in mud dominated, shallow estuaries. *Estuarine, Coastal and Shelf Science*, *69*(3), 519–530. https://doi.org/10.1016/j.ecss.2006.04.024.

Dellapenna, T. M., Hoelscher, C., Hill, L., Al Mukaimi, M. E., and Knap, A. (2020). How tropical cyclone flooding caused erosion and dispersal of mercury-contaminated sediment in an urban estuary: The impact of Hurricane Harvey on Buffalo Bayou and the San Jacinto Estuary, Galveston Bay, USA. *Science of The Total Environment*, *748*, 141226. https://doi.org/10.1016/j.scitotenv.2020.141226.

Dellapenna, T. M., Hoelscher, C., Hill, L., Critides, L., Salgado (Bartlett), V., Bell, M., Al Mukaimi, M. E., Du, J., Park, K., and Knap, A. H. (2022). Hurricane Harvey Delivered a

Massive Load of Mercury-Rich Sediment to Galveston Bay, TX, USA. *Estuaries and Coasts*, *45*(2), 428–444. https://doi.org/10.1007/s12237-021-00990-7.

Dellapenna, T. M., Kuehl, S. A., and Schaffner, L. C. (1998). Sea-bed mixing and particle residence times in biologically and physically dominated estuarine systems: A comparison of lower Chesapeake Bay and the York River subestuary. *Estuarine, Coastal and Shelf Science*, 46(6): 777–795. https://doi.org/10.1006/ecss.1997.0316.

Dellapenna, T. M., Kuehl, S. A., and Schaffner, L. C. (2003). Ephemeral deposition, seabed mixing and fine-scale strata formation in the York River estuary, Chesapeake Bay. *Estuarine, Coastal and Shelf Science*, 58(3): 621–643. https://doi.org/10.1016/S0272-7714(03)00174-4.

Du, J. & Park, K. (2019). Estuarine salinity recovery from an extreme precipitation event: Hurricane Harvey in Galveston Bay. *Science of The Total Environment*, *670*, 1049–1059. https://doi.org/10.1016/j.scitotenv.2019.03.265.

Du, J., Park, K., Dellapenna, T. M., and Clay, J. M. (2019a). Dramatic hydrodynamic and sedimentary responses in Galveston Bay and adjacent inner shelf to Hurricane Harvey. *Science of The Total Environment*, *653*, 554–564. https://doi.org/10.1016/j.scitotenv.2018.10.403.

Du, J., Park, K., Dellapenna, T.M., and Clay, J.M. (2019b). Dramatic hydrodynamic and sedimentary responses in Galveston Bay and adjacent inner shelf to Hurricane Harvey. *Science of the Total Environment,* 653: 554–564. https://doi.org/10.1016/j.scitotenv.2018.10.403.

Du, J., Park, K., Shen, J., Zhang, Y. J., Yu, X., Ye, F., Wang, Z., and Rabalais, N. N. (2019). A hydrodynamic model for Galveston Bay and the shelf in the northern Gulf of Mexico. *Ocean Science*, *15*(4), 951–966. https://doi.org/10.5194/os-15-951-2019.

Du, J., Park, K., Yu, X., Zhang, Y. J., and Ye, F. (2020). Massive pollutants released to Galveston Bay during Hurricane Harvey: Understanding their retention and pathway using Lagrangian numerical simulations. *Science of The Total Environment*, *704*, 135364

https://doi.org/10.1016/j.scitotenv.2019.135364.

Figlus, J. & Fuller, W.P. (2019). Deep-draft vessel wake and wind wave hydrodynamics near a mixed-sediment embankment in Galveston Bay, Texas. Final Report (June 2019) for U.S. Army Corps of Engineers – Galveston District, pp. 112, Department of Ocean Engineering, Texas A&M University / Texas A&M Engineering Experiment Station, Galveston, TX.

Figlus, J. & Song, Y.-K. (2020). Sand tracer study of a nearshore berm in South Padre Island, TX. Final Report (December 2020) for U.S. Army Corps of Engineers – Galveston District, pp. 22, Department of Ocean Engineering, Texas A&M University, Texas A&M Engineering Experiment Station, Galveston, TX.

Folk, R. L. (1966). A review of grain-size parameters. Sedimentology, 6(2), 73-93

Friedrichs, C.T. & Aubrey, D.G. (1988). Non-linear tidal distortion in shallow well-mixed estuaries: a synthesis. *Estuarine, Coastal and Shelf Science* 27, 521-545.

Friedrichs, C.T., Aubrey, D.G., and Speer, P.E. (1990). Impacts of relative sea-level rise on evolution of shallow estuaries. 105-122.

Gao., S., Collins, M., Lanckneus, J., De Moor, G., and Van Lancker, V. (1994). Grain size trends associated with net sediment transport patterns: an example from the Belgian continental shelf. *Marine Geology*, 121, 171-185.

HGSD. (2013). Subsidence and groundwater regulation FAQ's. Available at http://hgsubsidence.org/frequently-asked-questions/subsidence-groundwater-regulation-faqs/.

Hughes, S. A. (2005). Use of sediment trend analysis (STA) for coastal projects. ERDC/CHL CHETN-VI-40, U.S. Army Engineer Research and Development Center, Vicksburg, MS.

Jweda, J. & Baskaran, M. (2011). Interconnected riverine–lacustrine systems as sedimentary repositories: Case study in southeast Michigan using 210Pb and 137Cs-based sediment accumulation and mixing models. Journal of Great Lakes Research, 37(3): 432–446. https://doi.org/10.1016/j.jglr.2011.04.010.

Krishnaswamy, S., Lal, D., Martin, J. M., and Meybeck, M. (1971). Geochronology of lake sediments. *Earth and Planetary Science Letters*, 11(1): 407–414. https://doi.org/10.1016/0012-821X(71)90202-0.

McLaren, P. (2014). Sediment trend analysis (STA®): Kinematic vs. dynamic modeling. *Journal of Coastal Research*, 30(3), 429-437.

McLaren, P. (2016). The environmental implications of sediment transport in the waters of Prince Rupert, British Columbia, Canada: A comparison between kinematic and dynamic approaches. *Journal of Coastal Research*, 32(3), 465-482.

McLaren, P. & Bowles, D. (1985). The effects of sediment transport on grain-size distributions. *Journal of Sedimentary Research*, 55(4), 457-470.

McLaren, P. & Hill, S. (2001). A Sediment Trend Analysis (STA®). *Sea Technology*, *42*(3), 10-14.

McLaren, P., Hill, S. H., and Bowles, D. (2007). Deriving transport pathways in a sediment trend analysis (STA). *Sedimentary Geology*, 202(3), 489-498.

Nichols, M.M. (1989). Sediment accumulation rate and relative sea level rise in lagoons, in: Ward, L.G., Ashley, G.M. (Eds.), Physical processes and sedimentology of siliciclastic dominated lagoonal systems. *Marine Geology*, pp. 201-219.

Nittrouer, C. A., Sternberg, R. W., Carpenter, R., and Bennett, J. T. (1979). The use of Pb-210 geochronology as a sedimentological tool: Application to the Washington continental shelf. *Marine Geology*, 31(3): 297–316. https://doi.org/10.1016/0025-3227(79)90039-2.

Poizot, E. & Méar, Y. (2010) Using a GIS to enhance grain size trend analysis. *Environmental Modelling & Software*, 25, 513-525.

Rayson, M. D., Gross, E. S., Hetland, R. D., and Fringer, O. B. (2016). Time scales in Galveston Bay: An unsteady estuary. *Journal of Geophysical Research: Oceans*, 121(4): 2268–2285. https://doi.org/10.1002/2015JC011181.

Roberts, H. H., Huh, O. K., Hsu, S. A., Rouse, L. J., and Rickman, D. (1987). Impact of cold-front passages on geomorphic evolution and sediment dynamics of the complex Louisiana coast. In Coastal Sediments ’87 (pp. 1950–1963). American Society of Civil Engineers.

Rodriguez, A. B., Anderson, J. B., and Simms, A. R. (2005). Terrace Inundation as an Autocyclic Mechanism for Parasequence Formation: Galveston Estuary, Texas, U.S.A. *Journal of Sedimentary Research*, *75*(4), 608–620. https://doi.org/10.2110/jsr.2005.050.

Salehi, M. & Strom, K. (2012). Measurement of critical shear stress for mud mixtures in the San Jacinto estuary under different wave and current combinations. *Continental Shelf Research*, *47*, 78–92. https://doi.org/10.1016/j.csr.2012.07.004.

Santschi, P. H., Allison, M. A., Asbill, S., Perlet, A. B., Cappellino, S., Dobbs, C., and McShea, L. (1999). Sediment Transport and Hg Recovery in Lavaca Bay, as Evaluated from Radionuclide and Hg Distributions. *Environmental Science & Technology*, 33(3): 378–391. https://doi.org/10.1021/es980378l.

Schmidt, N., Dellapenna, T. M., and Lin, P. (2021). Cold Front Sediment Resuspension, Age, and Residence Times of Suspended Sediment Using $^{7}Be/^{210}Pb_{xs}$ Ratio in Galveston Bay. *Frontiers in Marine Science,* 8: 703945. https://doi.org/10.3389/fmars.2021.703945.

Sharma, P., Mahannah, R., Moore, W. S., Ku, T. L., and Southon, J. R. (1987). Transport of10Be and9Be in the ocean. Earth and Planetary Science Letters, 86(1): 69–76. https://doi.org/10.1016/0012-821X(87)90189-0.

Solis, R. S. & Powell, G. (1999). Hydrography, residence times, and physical processes. Biogeochemistry of Gulf of Mexico Estuaries. New York: John Wiley, 29-61.

Walker, N. D. & Hammack, A. B. (2000). Impacts of winter storms on circulation and sediment transport: Atchafalaya-Vermilion Bay region, Louisiana, USA. *Journal of Coastal Research*, 16: 996-1010. https://www.jstor.org/stable/4300118.

Ward, G. H. (1980). Hydrography and circulation processes of gulf estuaries. In: *Estuarine and Wetland Processes* (Hamilton, P. and Macdonald, K.B., eds), *Marine Science*, 11: 183-215. Springer, Boston, MA. https://doi.org/10.1007/978-1-4757-5177-2_7.

Weight, R. W. R., Anderson, J. B., and Fernandez, R. (2011). Rapid mud accumulation on the central Texas shelf linked to climate change and sea-level rise. *Journal of Sedimentary Research*, 81(10): 743–764. https://doi.org/10.2110/jsr.2011.57.

Wollast, R. (1993). Pollution of the North Sea. The Scheldt Estuary, pp. 183–193. doi:10.1007/978-3-642-73709-1_11.

Yeager, K. M., Santschi, P. H., and Rowe, G. T. (2004). Sediment accumulation and radionuclide inventories (239,240Pu, 210Pb and 234Th) in the northern Gulf of Mexico, as influenced by organic matter and macrofaunal density. Marine Chemistry, 91(1): 1–14. https://doi.org/10.1016/j.marchem.2004.03.016.

10 Appendix A: Surface Sediment Statistics

Table A-1: Surface sediment statistics for all samples used in STA analysis.

Name	Latitude	Longitude	Skewness	Standard Deviation /Sorting	Volume Weighted Mean	D25 (µm)	D75 (µm)	D50 (µm)	%Clay	%Silt	%Sand	Dominant Grain Size
STA-82	29.68089	-94.95322	6.3	54.5	23.4	2.11	22.75	7.1	36.2	55.3	8.1	Clay
STA-83	29.67153	-94.94488	6.4	51.5	23.7	1.81	26.02	7.4	37.8	53.1	8.7	Clay
STA-84	29.66175	-94.94331	3.1	52.3	59.3	14.34	96.36	51.4	15.9	40.4	39.2	Very Fine Sand
STA-86	29.61378	-94.93443	6.4	48.6	19.4	1.57	15.55	6.1	40	52.6	7	Clay
STA-87	29.61818	-94.96178	0.7	57.1	66.2	10.06	101.56	60.7	15.3	34.5	44.5	Very Fine Sand
STA-88	29.63525	-94.96716	0.4	61.7	101.8	63.73	138.04	97.1	7.4	15.4	67.7	Very Fine Sand
STA-89	29.65147	-94.97318	0.3	67.5	123.3	84.69	162.81	120	6.1	7.6	74.6	Very Fine Sand
STA-90	29.66773	-94.97915	5.2	160.5	147.3	71.09	186.96	122.2	7.7	13.3	71	Fine Sand
STA-91A	29.64468	-94.98723	5.1	56.2	28.9	3.52	29.83	8.9	26.7	59.6	12.8	Clay
STA-91B	29.67233	-94.98102	0.7	64.9	100	57.81	136.32	92.6	7	19.6	64.9	Very Fine Sand
STA-92	29.6746	-94.9825	6.7	109	97.1	48.8	118.29	78.1	6.4	28.4	59	Very Fine Sand
STA-93A	29.64983	-94.98396	5	51.1	35.7	5.53	49.02	21.2	18.9	62.9	17.2	Coarse Silt
STA-94A	29.63741	-94.99144	4.9	46.6	30.2	3.87	43.19	11	24.6	58.6	15.7	Clay
STA-93B	29.66942	-94.99015	0.9	67	87	38.02	124.39	76.6	9.7	29.5	54.2	Very Fine Sand
STA-94B	29.6624	-94.98717	0.8	46.7	58.7	15.68	87.12	54.1	12.6	42.6	40.5	Very Fine Sand
STA-95	29.65409	-94.98328	5.7	154.9	82.5	22.92	82.65	51.6	12.6	45.7	39.5	Very Fine Sand
STA-96	29.64625	-94.98132	8.5	94.7	48.8	7.26	58.46	30.5	18.8	57.4	22.6	Coarse Silt
STA-97	29.63953	-94.97675	0.7	46.9	55	8.18	85.2	51.1	17.3	39.9	38.7	Very Fine Sand
STA-98	29.6321	-94.97311	6.2	134.6	71.5	12.43	78.88	45	14.8	47.9	35.1	Very Fine Sand
STA-99A	29.61629	-94.99307	0.7	66.5	93.1	48.02	131.24	86.8	9.6	22.3	60.3	Very Fine Sand
STA-99B	29.62417	-94.97122	5.9	168.8	52.2	2.95	27.82	8.4	30.4	56.3	13.1	Clay
STA-100	29.61805	-94.9682	1.2	60.5	57.3	5.65	93.38	38.5	19.8	39.9	35.8	Very Fine Sand
STA-101	29.61753	-94.978	0.7	89.4	107.1	19.62	162.97	98.4	13	22.1	57.7	Fine Sand
STA-102	29.6249	-94.98402	1.4	92.7	75.7	4.41	124.07	34.1	22.9	36	37.4	Clay
STA-103	29.63299	-94.98901	6.1	36.1	24.2	3.19	34.57	9	28.5	58.6	12.1	Clay
STA-104	29.64252	-94.99222	4.9	52.1	35.1	3.38	52.22	14.4	26.8	52.2	19.3	Clay
STA-105	29.65075	-94.9953	6.6	55.7	43.1	5.08	64.95	31.2	21.2	50.8	25.8	Coarse Silt
STA-106	29.6531	-94.9967	9	87.1	50.7	6.16	66.07	34.5	19.6	51.8	26.6	Coarse Silt
STA-107A	29.62831	-94.99895	6.6	48.3	21.8	2.83	20.26	7	31.9	59.6	8.2	Clay
STA-108A	29.63728	-95.00009	8.9	44.9	25.6	3.37	35.95	9.2	27.6	59.9	11.8	Clay
STA-107B	29.66455	-94.99728	0.5	49.8	79.7	47.46	108.88	75.2	7.6	28.6	56.9	Very Fine Sand
STA-108B	29.64019	-95.01105	8.5	74.1	43	4.76	58.74	27	21.1	54.9	22.7	Coarse Silt
STA-108C	29.61883	-94.9874	0.5	87.7	119.1	63.1	179.47	113.2	10.7	16.5	64.6	Fine Sand
STA-200	29.66204	-94.97755	0.3	72.3	131.4	89.37	174.02	127.7	5.3	7.9	75.4	Fine Sand
STA-203	29.62913	-94.96561	5.3	190	114.4	29.77	127.47	79.3	12.3	25.7	55.6	Very Fine Sand
STA-204	29.61087	-94.95863	0.6	89.2	113	22.16	170.18	109.3	12.2	19.5	60.5	Fine Sand
STA-205	29.60203	-94.95763	1.2	64.3	59.2	5.29	97.47	35.9	20.5	39.4	35.5	Very Fine Sand
STA-206	29.59463	-94.95279	4.6	77.7	56.3	7.86	76.91	36.7	17.2	49	31	Very Fine Sand
STA-207A	29.6236	-95.00137	4.4	63.9	51.5	4.63	82.28	31.5	21.7	42.6	32	Very Fine Sand
STA-207B	29.59174	-94.96259	0.4	57.2	79.6	32.53	116.46	78.3	11.7	25.2	55.4	Very Fine Sand
STA-208A	29.65037	-94.98946	4.4	57.8	43.1	4.33	64.18	27.6	23	49.6	25.3	Clay
STA-208B	29.5999	-94.96554	0.4	63.5	89.3	42.48	129.38	86.9	12	20.7	59	Very Fine Sand
STA-209	29.60832	-94.96767	0.9	69.2	78.2	11.18	120.33	69.3	13.6	31.7	48.4	Very Fine Sand
STA-210	29.61199	-94.96844	5.2	186.7	103.5	8.99	119.9	63.7	16.3	32	46.9	Very Fine Sand
STA-211	29.60534	-94.97475	0.9	80.8	102	32.88	150.39	91.4	7.1	28.6	57	Very Fine Sand
STA-212A	29.64518	-94.96441	0.8	61.5	117.2	4.78	94.75	53.6	22.4	31.7	40.8	Very Fine Sand
STA-212B	29.59869	-94.97124	0.2	61.5	117.2	80.24	154.07	113.7	4.7	9.4	74.3	Very Fine Sand
STA-213	29.59027	-94.9703	0	43.5	88	63.92	144.22	87.1	5.5	16.1	69.2	Very Fine Sand
STA-214	29.59031	-94.9801	0.1	45.8	101.8	75.37	128.92	99.6	4.1	9	75.1	Very Fine Sand
STA-215	29.5963	-94.9799	0.1	42.2	99.6	74.22	124.42	96.8	3.4	9.2	76	Very Fine Sand
STA-216	29.604	-94.98059	0.6	54.1	90	55.09	120.48	83.7	6	23.4	62.7	Very Fine Sand
STA-217	29.61235	-94.98336	0.8	83.1	108.1	44.05	157.75	97.6	9.8	21.9	60.9	Very Fine Sand
STA-218	29.61227	-94.98838	0.4	81.5	150.2	97.68	198.66	142.6	3.9	7	79.1	Fine Sand
STA-219	29.617	-94.98733	0.7	85.8	111.9	44.66	163.3	102.8	9.9	20.3	62.1	Very Fine Sand
STA-220	29.62666	-94.99064	5.5	57.2	38	3.85	55.67	13.6	24.8	52.6	20.9	Clay
STA-221	29.63439	-94.99558	10.4	49	37.9	3.53	57.86	15.6	24.7	50.8	22.4	Clay
STA-222A	29.63276	-95.00902	10.2	90.9	42.9	3.72	56.8	23	25.4	51.8	21.5	Clay
STA-222B	29.64223	-94.99979	4.8	47.5	32.6	3.43	49.4	12.7	26.9	53.9	17.8	Clay
STA-223	29.65049	-95.00159	3	60.7	52.5	7.04	75.27	38	18.2	48.2	30.7	Very Fine Sand
STA-224	29.6588	-95.00316	0.5	49.6	73.9	41.09	104.21	71.1	9.7	30.4	53.5	Very Fine Sand
STA-225	29.65062	-95.00766	7.7	121.8	80.9	20.54	105.45	60.2	12.1	38	45	Very Fine Sand
STA-226A	29.61014	-94.95483	7.6	93.7	40.4	4.61	42.34	11.9	21	61.2	16.8	Clay

Name	Latitude	Longitude	Skewness	Standard Deviation /Sorting	Volume Weighted Mean	D25 (µm)	D75 (µm)	D50 (µm)	%Clay	%Silt	%Sand	Dominant Grain Size
STA-226B	29.64218	-95.0077	3.9	50.3	38.7	4.68	56.7	24.5	21.8	55.4	21.3	Coarse Silt
STA-227	29.63414	-95.00474	4.3	40.3	27.7	3.04	41.99	10	29.3	55.9	14	Clay
STA-228	29.6373	-95.00974	9.8	65.3	42.2	4.65	59.2	30	22	53.7	22.8	Coarse Silt
STA-229A	29.657	-94.99135	4	72.4	54.9	6.78	75.96	38.1	17.7	48.2	31.4	Very Fine Sand
STA-229B	29.6293	-95.0067	3.9	61.3	47.2	5.63	65.97	33.9	19.7	51.6	26.8	Coarse Silt
STA-300	29.6671	-94.98337	7.8	133.6	82	15.1	104.48	63.7	13	34.5	47.1	Very Fine Sand
STA-301	29.65925	-94.98182	7.7	100.5	72	11.41	96.99	59.2	14.6	36.2	44.5	Very Fine Sand
STA-302	29.65145	-94.97794	3.3	84.9	76.4	10.48	106.89	64	15.5	32.1	47.2	Very Fine Sand
STA-303A	29.66271	-94.97052	3.2	48.9	33.1	4.16	43.79	12.3	23.3	58.3	16.8	Clay
STA-303B	29.64487	-94.97512	2.5	81.1	60.5	5.45	83.91	29.6	20.3	46.2	30.7	Clay
STA-304	29.63707	-94.97113	7	90.4	89.1	40.83	121.8	81.1	11.6	23.6	57.4	Very Fine Sand
STA-305A	29.65577	-94.96863	2	262.3	222.5	18.29	335.58	138.3	14.1	22.8	63.9	Medium Sand
STA-305B	29.62093	-94.96987	5.6	59.4	38.2	4.45	53.94	18.4	22.3	56	20.1	Clay
STA-306	29.62349	-94.96687	6.7	128	71.1	8.81	83.81	46.3	15.3	45.2	36.7	Very Fine Sand
STA-307	29.61919	-94.96487	7.4	85.9	58.1	7.44	78.33	42.8	16.8	46.6	33.8	Very Fine Sand
STA-308A	29.63458	-94.98084	7.4	122.7	47.9	3.39	46.94	9.5	27.4	51.6	19.5	Clay
STA-308B	29.61308	-94.97241	4.8	167.6	121.6	23.52	149.44	91.8	12.1	22.2	58.9	Very Fine Sand
STA-309	29.60257	-94.97746	0.4	56.7	112.9	77.11	145.99	107.7	3.8	9.9	74.9	Very Fine Sand
STA-310	29.60794	-94.984	0.6	59.2	104.6	65.33	138.83	97.6	4.8	16.6	69.2	Very Fine Sand
STA-311	29.61436	-94.97517	3.8	64.2	32	4.18	22.93	9.2	22.7	63.6	12.5	Clay
STA-312A	29.62222	-94.99363	3.5	238.7	166	9.5	216.93	113.5	15.3	23.6	57.3	Fine Sand
STA-312B	29.61945	-94.97328	0.7	78.6	92	12.46	141.75	86.4	14.2	24.6	53.9	Very Fine Sand
STA-313	29.62427	-94.97697	2.8	66.8	43.5	4.01	59.57	12.2	23.9	51.3	22.5	Clay
STA-314A	29.63039	-94.99309	2.7	85.7	47.9	3.4	46.63	9.5	27.3	50.9	20.4	Clay
STA-314B	29.61932	-94.98265	1.1	84.2	80	6.03	129.67	56.9	18.8	32.3	43.6	Very Fine Sand
STA-333	29.62174	-94.95885	8.1	58.1	32.9	4.16	47.72	11.4	23	58.1	17.6	Clay
STA-335	29.62153	-94.95596	3.4	242.2	160.2	8.22	204.24	92.3	17.5	25	54.3	Fine Sand
STA-336	29.62918	-94.97901	3.4	72.6	42.2	3.42	49.35	12.1	26.9	52	19.6	Clay
STA-0	29.64529	-95.00438	10.8	85.3	36	4.09	46.42	12.5	23.5	58.8	16.6	Clay
STA-400	29.64228	-94.96775	0.8	81	101.5	29.6	147.74	94.4	11.7	20.7	67.6	Very Fine Sand
STA-401	29.6658	-94.99196	0.4	75.4	123.8	75.6	169.34	118.7	7.2	11.5	81.4	Fine Sand
STA-402	29.64832	-95.01049	0.5	57.6	91	53.72	125.1	86.3	8.2	21.3	70.4	Very Fine Sand
STA-403	29.6443	-95.01174	0.7	66.6	92.6	45.72	131.08	85.3	9.8	23.5	66.6	Very Fine Sand
STA-404	29.64152	-95.01277	6.4	151.2	108.8	47.81	129.82	84.1	9.4	23.7	67	Very Fine Sand
STA-405	29.63956	-95.01375	0.6	55.4	75.2	31.82	109.61	72	12.8	28.3	58.9	Very Fine Sand
STA-406	29.6333	-95.01352	0.9	62	67.1	6.6	105.35	58.5	19.5	31.5	49	Very Fine Sand
STA-407	29.62866	-95.01041	0.7	56.7	71.7	22.65	106.07	66.3	14.5	31	54.4	Very Fine Sand
STA-408	29.62448	-95.00692	0.8	51.9	56.3	5.24	89.84	51.3	21.3	34.7	43.9	Very Fine Sand
STA-409	29.62187	-95.00359	0.9	50.4	53.9	6.23	85	45.9	19.2	40.5	40.3	Very Fine Sand
STA-410	29.61696	-94.99707	0.6	43.3	69.5	42.08	94.11	65.3	8	36.5	55.5	Very Fine Sand
STA-411	29.61413	-94.99337	10	29.6	13.3	2.8	12.74	6.3	32.7	63.9	3.4	Clay
STA-413	29.61406	-94.97691	2.2	11	10.5	3.33	13.14	7	28.3	71.3	0.4	Clay
STA-414	29.61411	-94.96982	16.1	51.9	15.8	3.56	14.31	7.4	26.7	70	3.3	Clay
STA-415	29.61429	-94.95874	7.7	53.4	27.4	3.68	34.04	10	25.7	61.6	12.8	Clay
STA-417	29.60857	-94.94789	1.9	367.1	293.9	61.24	399.98	137.4	9.7	15	75.3	Very Fine Sand
STA-418	29.60236	-94.94661	2.3	316.7	216.7	6.83	282.12	95.8	19.3	23.1	57.5	Clay
STA-419	29.59779	-94.94024	0.7	197.7	313.9	172.77	430.2	290.3	3.5	5.2	91.2	Medium Sand
STA-420	29.59134	-94.93732	1.3	35	28.9	2.05	50.89	9.2	36.3	44	19.7	Clay
STA-421	29.5611	-94.93122	4.2	28.6	12.8	1.21	9.19	3.2	54.8	39.4	5.9	Clay
STA-422	29.58906	-94.92598	5.3	180	73.6	2.5	78.73	11.3	31.8	39.5	28.7	Clay
STA-423	29.59585	-94.92939	0.3	53.9	92.2	59.65	124.58	89.2	7.5	18	74.6	Very Fine Sand
STA-424	29.60186	-94.9366	0.3	57.6	119.7	84.83	152.84	115.1	3.5	6.9	89.6	Very Fine Sand
STA-425	29.6069	-94.94179	2.3	344.3	284.4	92.51	310.4	167.9	5	12.1	82.9	Fine Sand
STA-426	29.60873	-94.93155	0.9	45.3	56.8	18.3	83.84	50.9	12.2	45.8	42	Very Fine Sand
STA-427	29.60247	-94.92938	0.3	49.4	78.1	46.94	109.22	76.9	9.5	25.6	65	Very Fine Sand
STA-428	29.59545	-94.92217	0.4	53.1	80.9	46.22	113.76	78.7	9.9	24.8	65.4	Very Fine Sand
STA-429	29.58236	-94.9401	5.7	125.3	72.1	6.69	94.2	39.1	16	43.4	40.7	Very Fine Sand
STA-430	29.58707	-94.94282	1.2	52.1	53.3	8.31	82.91	39.7	16.9	45.9	37.2	Very Fine Sand
STA-431	29.59096	-94.94618	4.4	196.7	126.7	15.83	145.13	86.7	11.6	26.3	62.2	Very Fine Sand
STA-432	29.60047	-94.96375	0.4	54.7	83.7	48.39	117.17	80.8	9.5	23.7	66.8	Very Fine Sand
STA-434	29.6059	-94.5854	0.5	63	89.7	44.1	128.63	86	10.2	22.7	67.1	Very Fine Sand
STA-436	29.58693	-94.94052	0.1	44.9	101.1	74.97	127.74	98.9	4.1	9	87	Very Fine Sand
STA-437	29.58729	-94.97775	0	40.5	86.9	64.14	111.05	85.5	4.9	16.1	79	Very Fine Sand

Table A-2: Surface sediment statistics for locations sampled in 2017/18 post-Harvey.

2017-2018 Sample Name	Latitude	Longitude	%Sand	%Silt	%Clay	d (0.1)	d (0.2)	d (0.5)	d (0.8)	d (0.9)	Volume weighted mean	Skew-ness	Kurtosis	STD	Mode
Harv-7A SL	29.577817	94.902633	41.58	39.73	18.69	1.66	4.51	51.22	104.93	151.73	70.34	2.93	11.92	87.63	71.99
Harv-10 SL	29.55425	94.994967	27.67	47.01	25.32	1.53	3.08	18.81	83.04	134.67	53.05	3.30	14.90	83.67	63.03
Harv-05 SL	29.609833	94.830467	18.29	45.00	36.71	1.02	1.99	6.63	52.31	138.21	46.69	6.49	63.81	118.07	4.25
Hary-8 SL	29.552933	94.97495	23.47	37.48	39.05	0.98	1.83	6.32	81.96	174.52	53.62	3.21	13.31	103.46	3.51
C18 SL	29.6604	94.991017	46.69	37.83	15.48	1.91	7.67	58.35	115.21	159.85	75.78	2.85	12.79	83.39	77.33
HARV-06 SL	29.586867	94.864683	12.30	51.02	36.68	1.19	2.25	5.87	24.43	93.02	31.43	3.94	18.20	73.44	4.79
C18A SL	29.6604	94.991017	16.73	48.20	35.07	1.04	2.06	7.40	51.72	97.67	34.93	3.96	20.61	67.65	4.31
HARV-C10 SL	29.55425	94.994967	48.30	34.51	17.19	1.85	5.32	56.49	266.67	391.97	137.06	1.56	2.15	170.64	298.43
C-09 SL	29.637883	94.804183	13.49	52.94	33.58	1.14	2.28	7.03	29.95	101.85	34.66	3.83	16.97	77.55	5.66
HARV-1 SL	29.55485	94.966533	10.73	48.20	41.06	1.02	1.91	5.18	19.45	68.22	25.74	4.85	28.75	64.47	4.58
C22 SL	29.739	95.038083	7.41	63.49	29.11	1.33	2.67	8.74	28.65	50.39	23.48	5.55	39.67	48.98	7.37
HARV-17 SL	29.623883	94.929383	4.52	52.56	42.92	0.93	1.70	5.11	21.12	36.14	18.47	6.46	51.29	47.89	3.61
TB-D2 SL	29.695883	94.7746	8.75	52.08	39.17	0.97	1.83	6.20	25.41	51.41	27.74	4.71	25.97	68.39	3.53
HARV-7B SL	29.557	94.924667	19.30	41.45	39.25	0.89	1.66	6.58	58.19	143.82	42.45	3.11	11.50	83.55	3.33
DB-08	29.45644	94.88131	74.55	13.49	11.97	2.86	17.59	130.60	210.81	259.78	132.81	0.44	-0.19	96.28	160.33
DB-09	29.44817	94.85933	49.56	30.37	20.07	1.41	3.98	61.61	148.90	197.90	80.48	1.10	0.90	83.82	126.96
DB-10	29.43503	94.85826	71.92	15.87	12.22	2.86	13.41	119.96	198.67	246.46	123.08	0.48	-0.24	92.27	151.91
DB-11	29.4142	94.85553	36.41	37.83	25.76	1.19	2.90	14.60	124.77	173.77	60.42	1.48	1.90	77.39	129.08
DB-12	29.39361	94.85291	39.63	36.71	23.66	1.23	3.16	28.75	107.70	142.24	56.53	1.98	9.46	65.41	98.54
DB-13	29.38245	94.82774	48.81	42.29	8.91	5.27	29.77	61.78	103.18	133.09	72.82	3.77	24.14	68.23	69.98
DB-14	29.48664	94.8827	38.58	37.68	23.74	1.12	3.01	38.99	105.45	150.03	85.92	5.45	33.58	197.33	85.81
DB-15	29.472467	94.870367	67.12	20.39	12.50	2.65	13.45	92.57	156.78	202.69	121.57	5.32	34.45	184.76	112.33

Table A-3: Surface sediment statistics for re-sampled locations from Harvey study.

2021-2022 Sample Name	Latitude	Longitude	%Sand	%Silt	%Clay	d (0.1)	d (0.2)	d (0.5)	d (0.8)	d (0.9)	Volume weighted mean	Skew-ness	Kurtosis	STD	Mode
Harv-16	29.6199	94.9007	36.61	41.23	22.16	1.31	3.47	26.59	129.36	209.49	101.70	4.60	23.79	226.73	114.47
STA-11B	29.61707	94.96986	63.20	20.99	15.81	1.79	6.68	88.50	152.29	191.88	92.02	0.68	0.21	75.30	116.94
STA-25	29.63632	94.98535	14.44	54.84	30.72	0.97	2.20	9.59	45.03	83.42	29.71	4.84	37.67	53.01	6.33
C-18--21	29.66044	94.99096	37.82	45.78	16.41	1.76	5.75	46.17	97.07	133.56	61.06	3.14	17.06	69.83	69.80
C-22--21	29.73906	95.03812	41.91	34.69	23.40	1.29	3.22	34.97	146.66	226.89	88.49	4.67	35.54	145.33	115.46
EB-05	29.40372	94.79181	85.61	8.11	6.28	10.56	109.38	166.87	228.00	264.49	162.56	-0.18	-0.05	84.93	179.76
EB-06	29.45692	94.81233	43.80	34.96	21.24	1.26	3.64	44.44	127.77	173.61	75.81	6.48	65.85	121.72	111.67
EB-07	29.5072	94.8288	27.38	50.72	21.90	1.25	3.56	13.47	97.15	163.50	53.98	2.58	8.37	84.63	8.72
DB-06	29.47389	94.91344	78.02	15.18	6.80	8.77	59.17	100.09	147.23	176.15	101.48	0.23	0.02	58.47	110.25
DB-08	29.45644	94.88131	65.61	20.26	14.14	2.23	7.89	112.45	199.70	251.76	117.93	0.66	-0.03	99.05	158.51
DB-09	29.44817	94.85933	51.98	29.20	18.82	1.47	4.41	69.59	158.02	207.68	85.92	1.00	0.56	86.89	133.98
DB-10	29.43503	94.85826	57.70	23.44	18.87	1.38	4.46	87.73	171.87	219.55	96.01	0.76	-0.06	89.08	142.76
DB-11	29.4142	94.85553	51.30	29.04	19.65	1.34	4.12	67.97	165.33	218.36	88.64	1.02	0.50	91.39	143.01
DB-12	29.39361	94.85291	53.06	29.26	17.68	1.60	4.95	69.00	133.93	176.17	83.97	6.32	67.88	113.00	103.68
DB-14	29.48664	94.8827	24.03	48.46	27.52	0.95	2.40	16.44	71.96	102.97	39.49	3.46	23.15	54.30	69.30

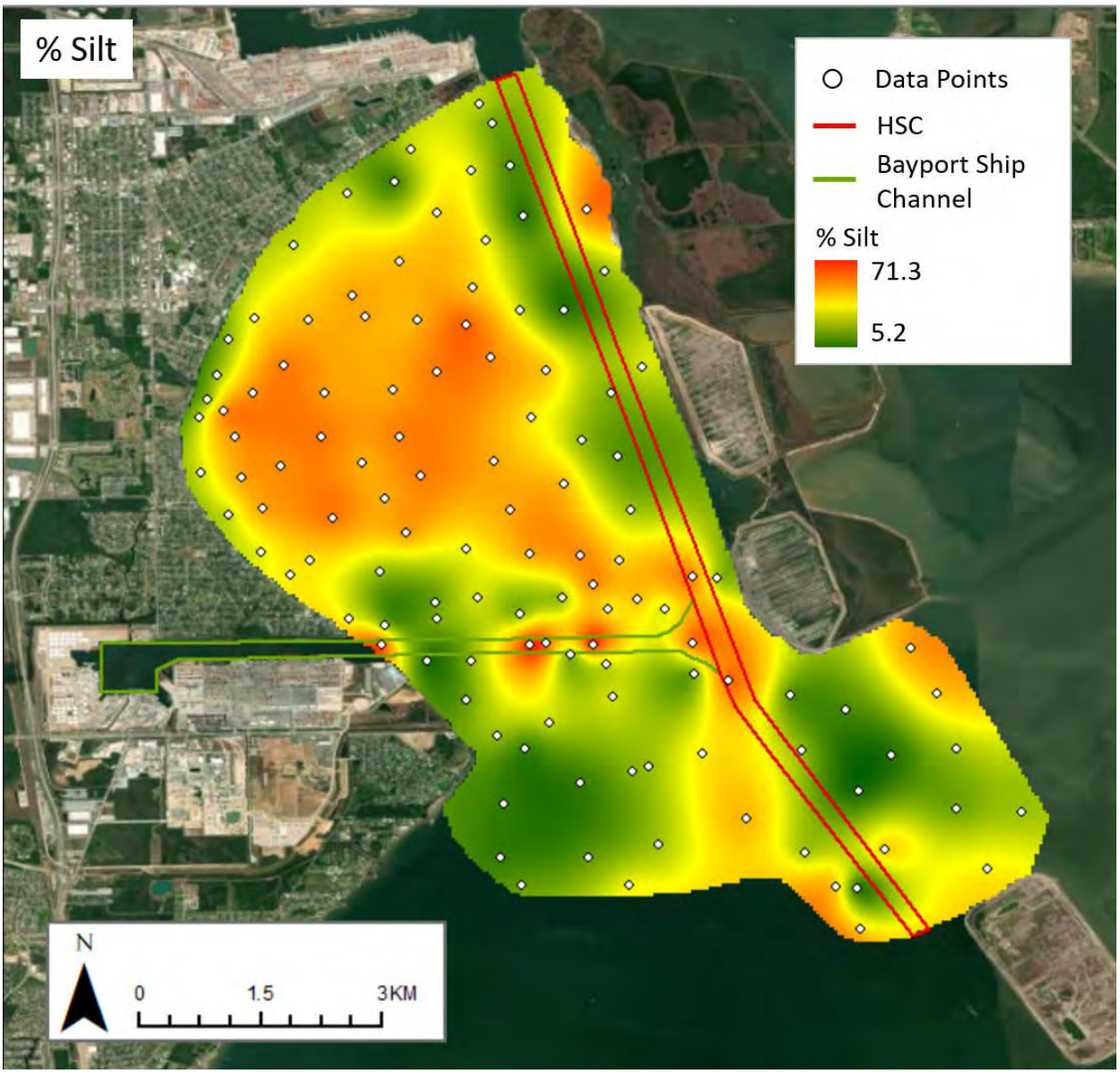

Figure A-1: Map showing percentage of silt sediment fraction in the project area.

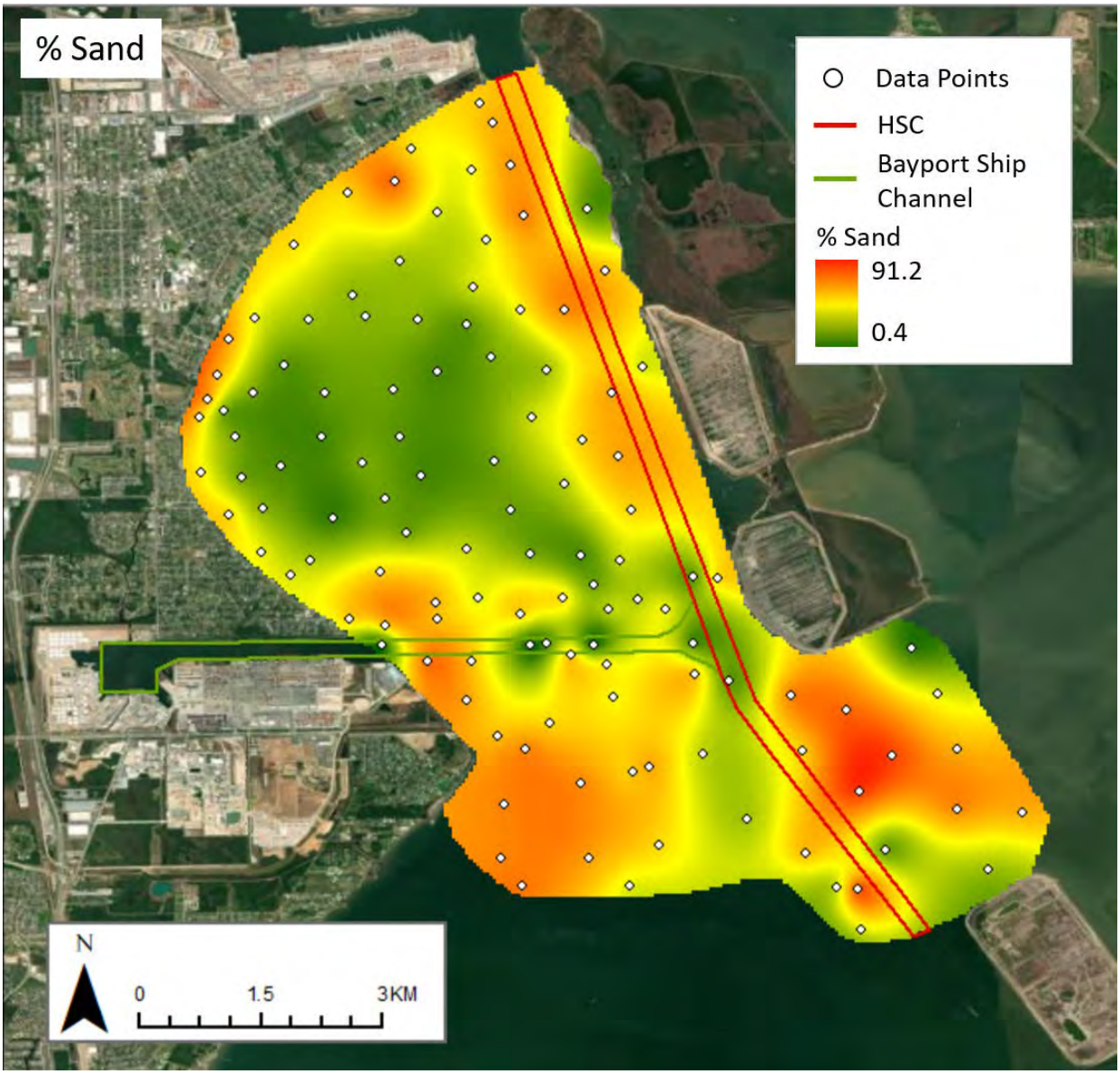

Figure A-2: Map showing percentage of sand sediment fraction in the project area.

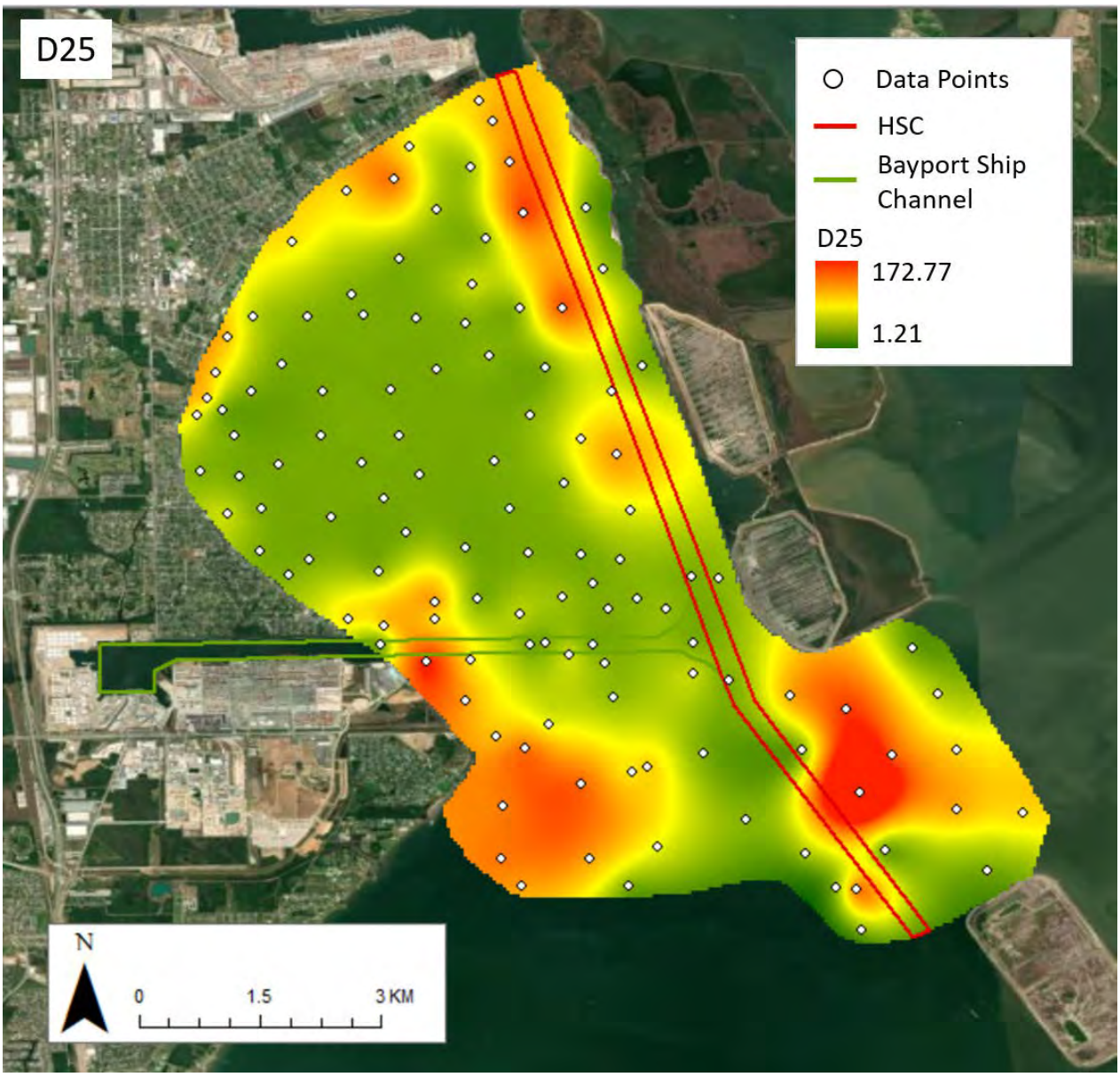

Figure A-3: Map showing D_{25} (in μm) in the project area.

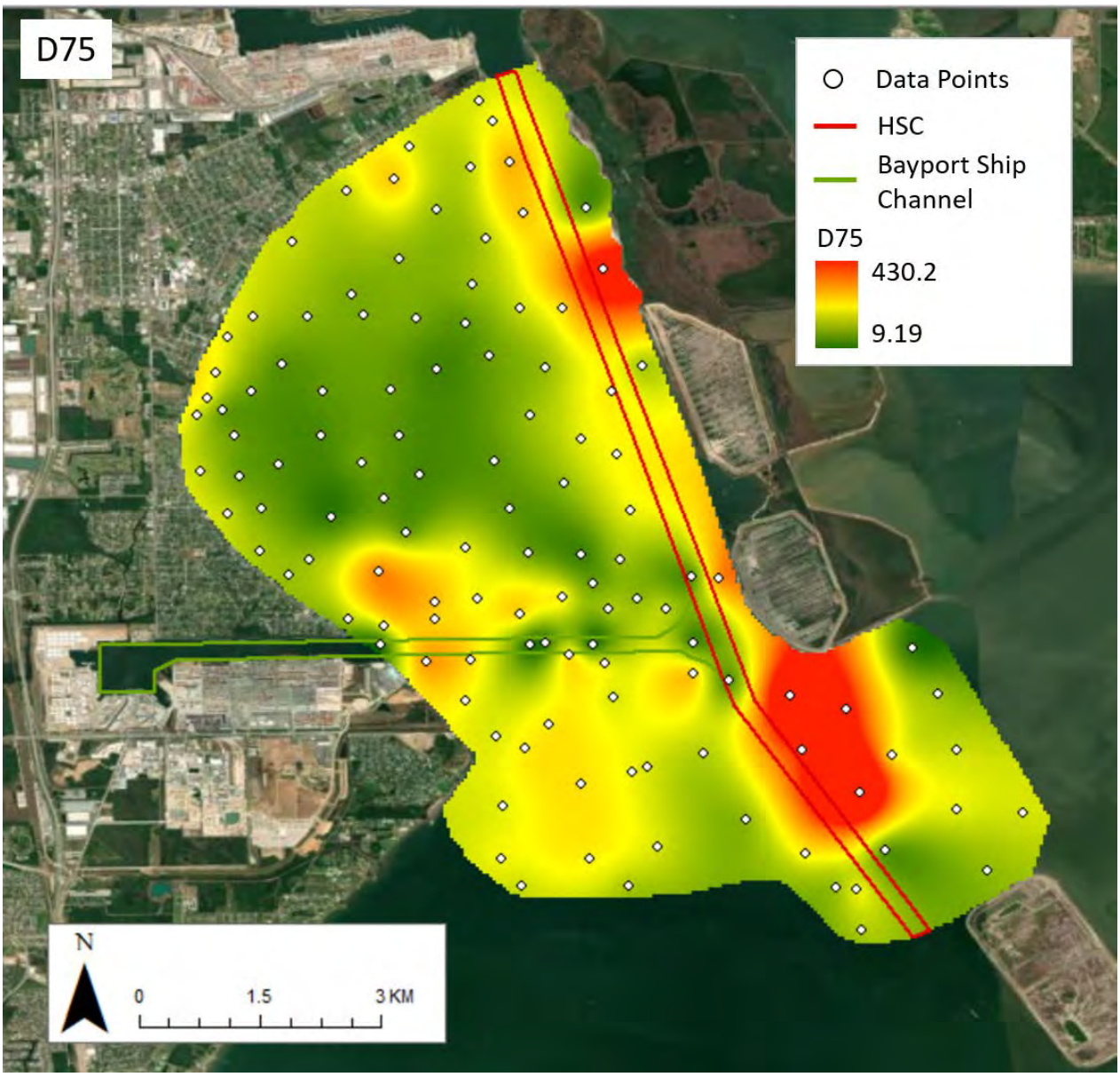

Figure A-4: Map showing D_{75} (in μm) in the project area.

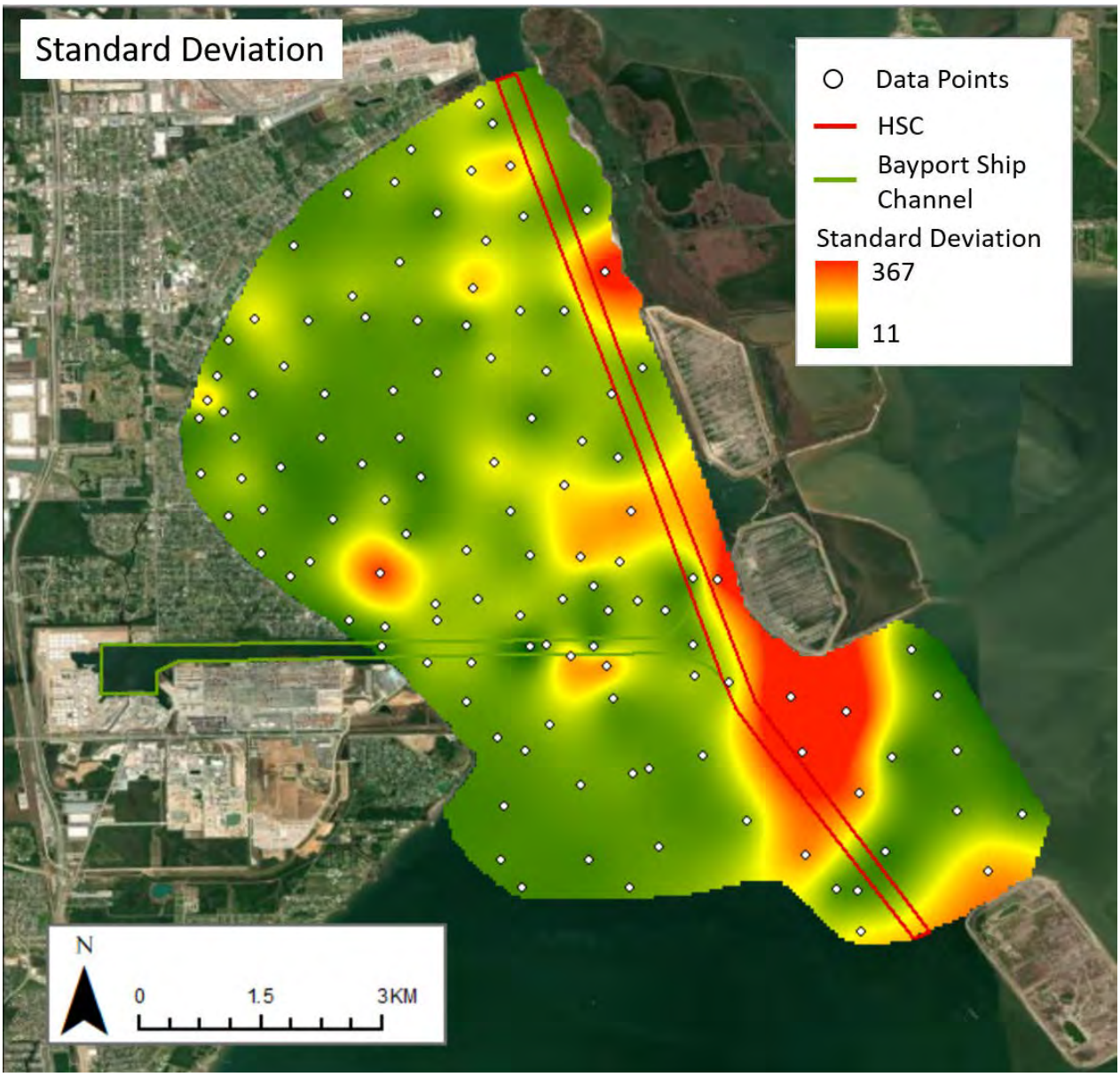

Figure A-5: Map showing sediment grain diameter standard deviation (in μm) in the project area.

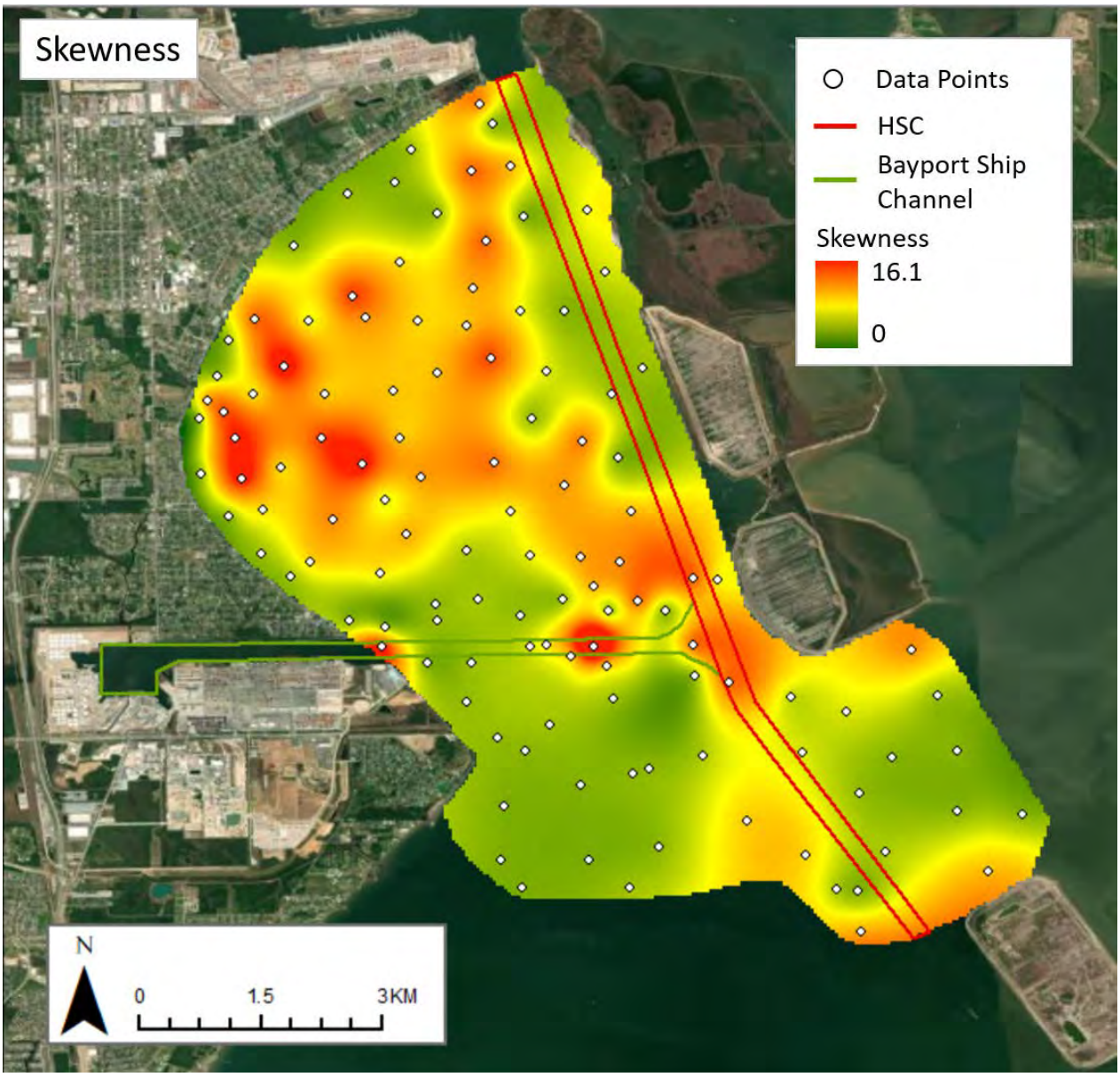

Figure A-6: Map showing sediment grain diameter skewness in the project area.

11 Appendix B: Fixed Hydrodynamic Measurement Data

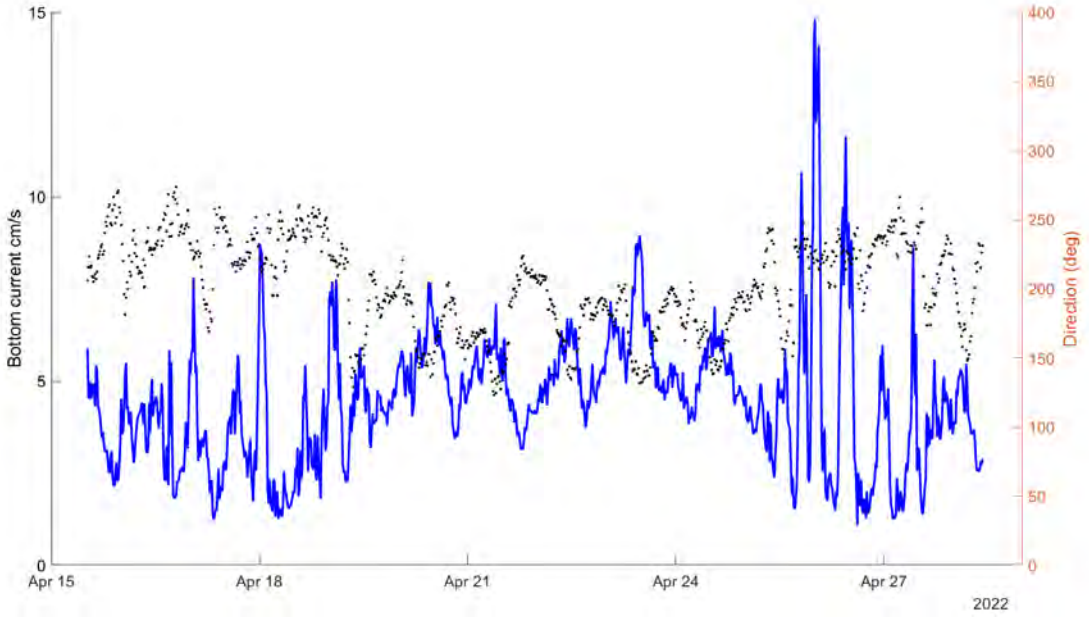

Figure B-1: Time series of current speeds (blue line) and direction (black) recorded by TC1.

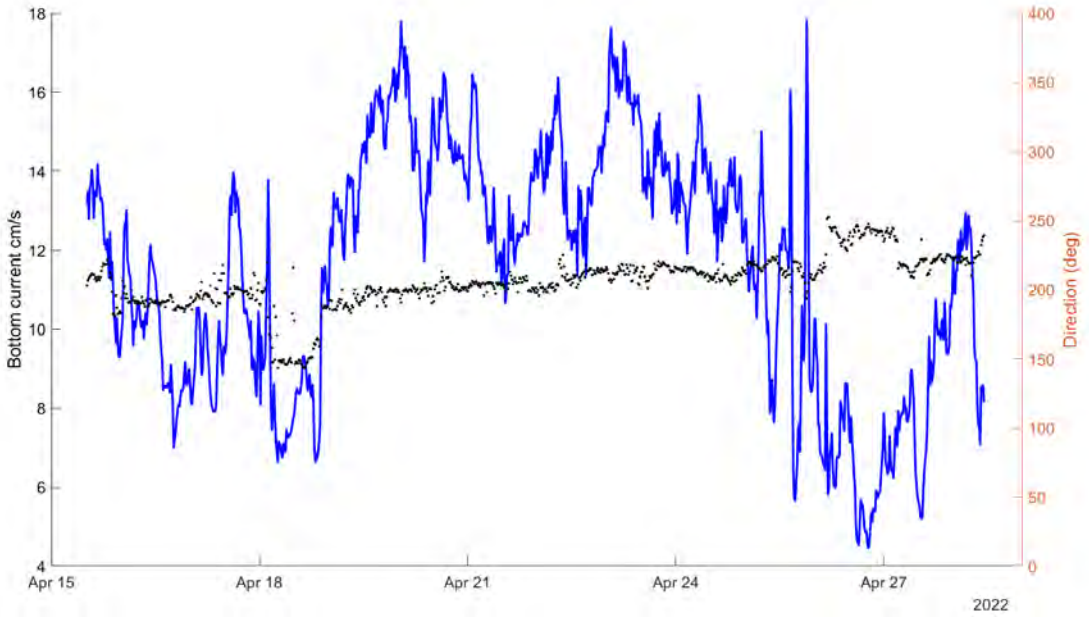

Figure B-2: Time series of current speeds (blue line) and direction (black) recorded by TC2.

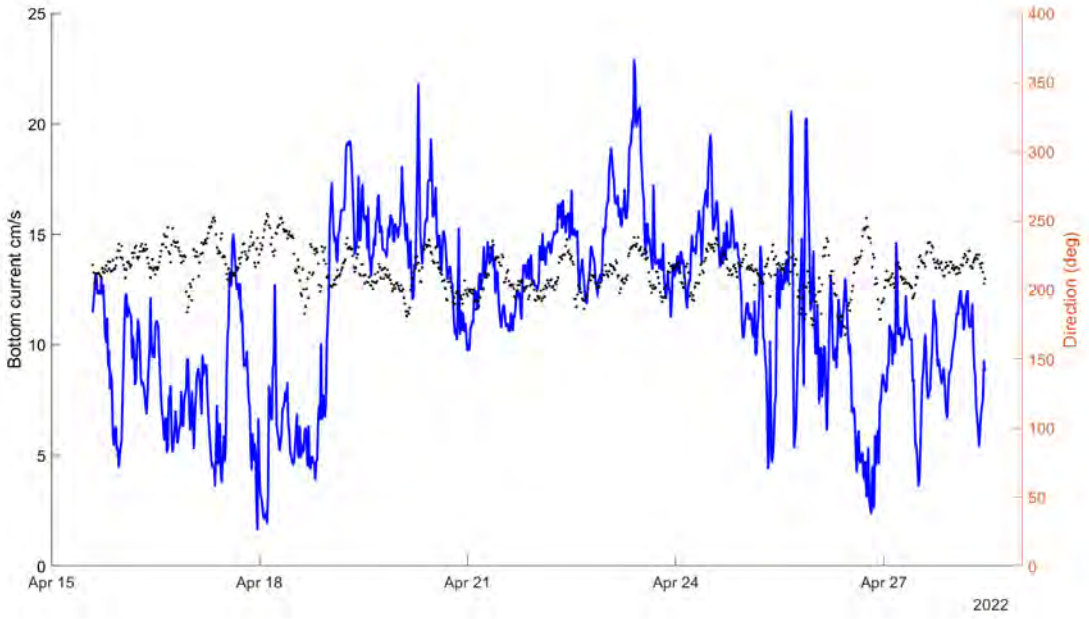

Figure B-3: Time series of current speeds (blue line) and direction (black) recorded by TC4.

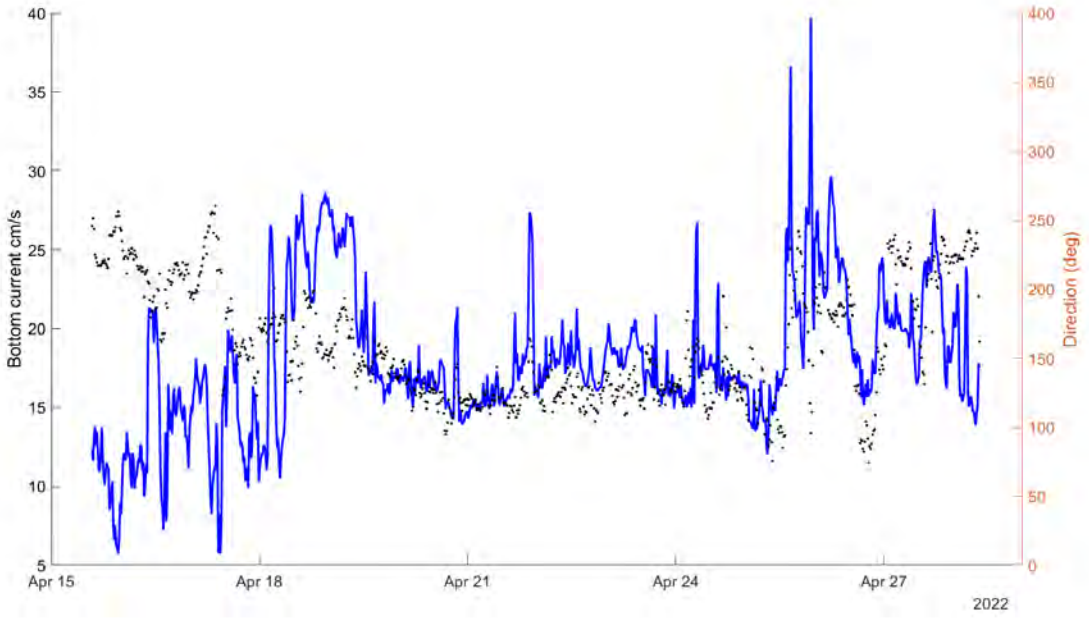

Figure B-4: Time series of current speeds (blue line) and direction (black) recorded by TC5.

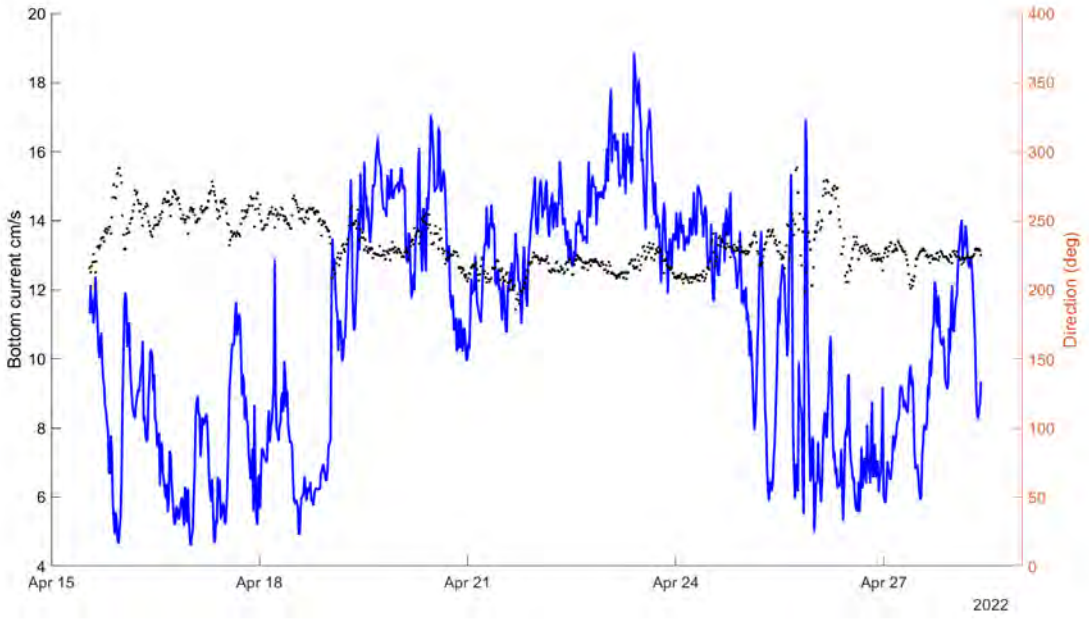

Figure B-5: Time series of current speeds (blue line) and direction (black) recorded by TC6.

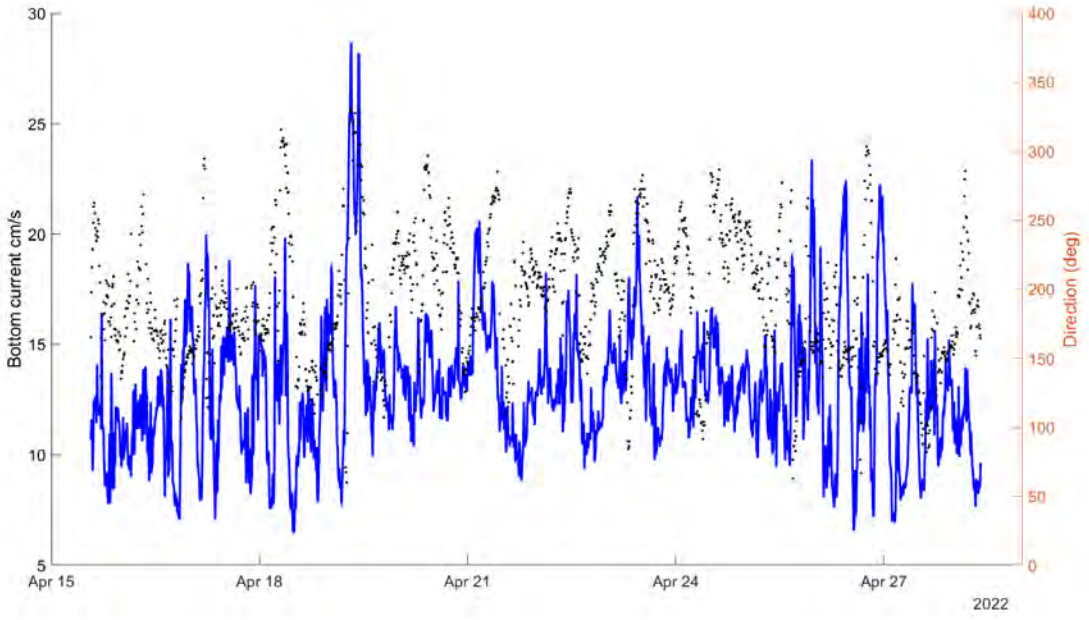

Figure B-6: Time series of bottom current speeds (blue line) and direction (black) recorded by ADCP2 (burst data).

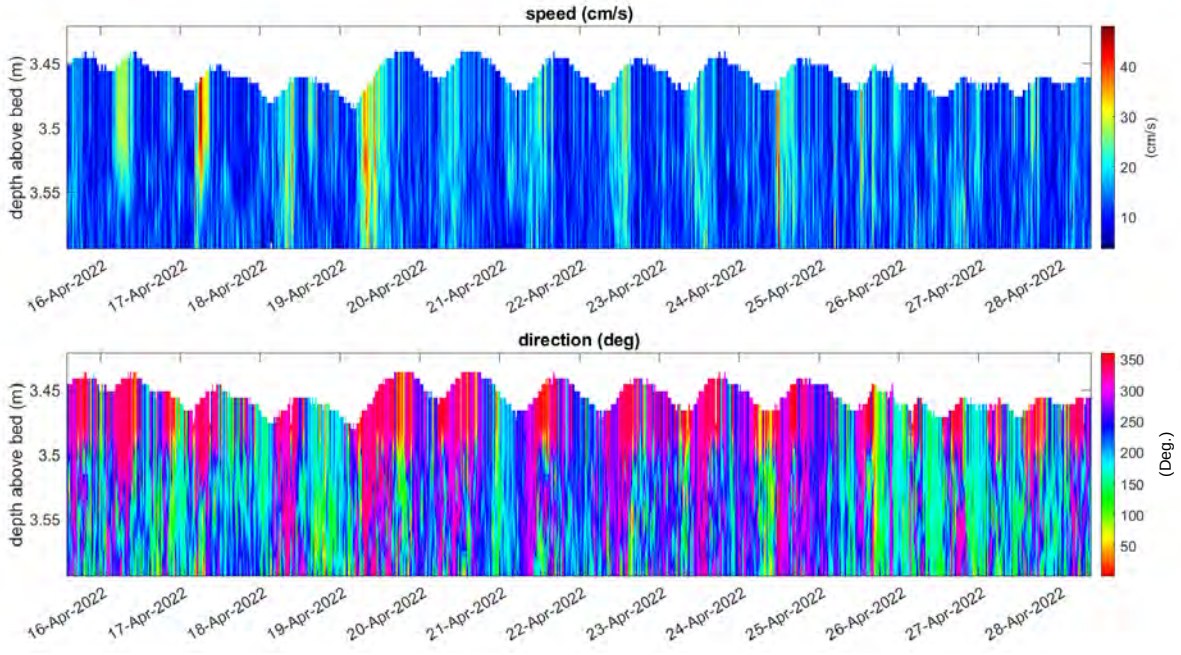

Figure B-7: Time series of current speeds (top) and direction (bottom) over the measuring water depth recorded by ADCP2 (profile data).

12 Appendix C: Vessel-Mounted Hydrodynamic Measurement Data

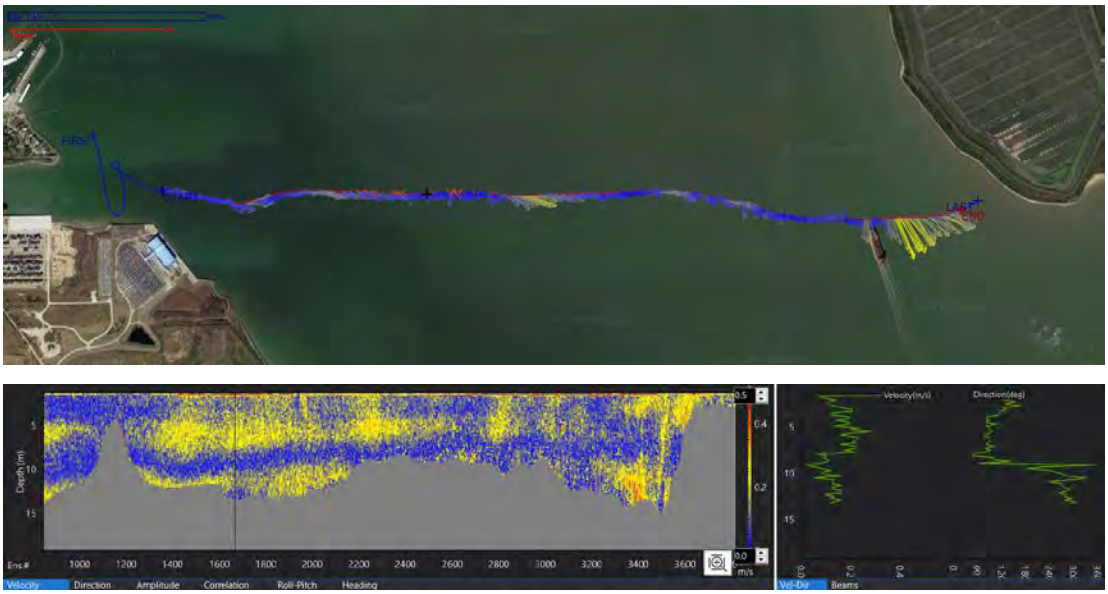

Figure C-1: Vessel track and velocity map for VM run: 20220201_BayportChannel_Ebb_Data.

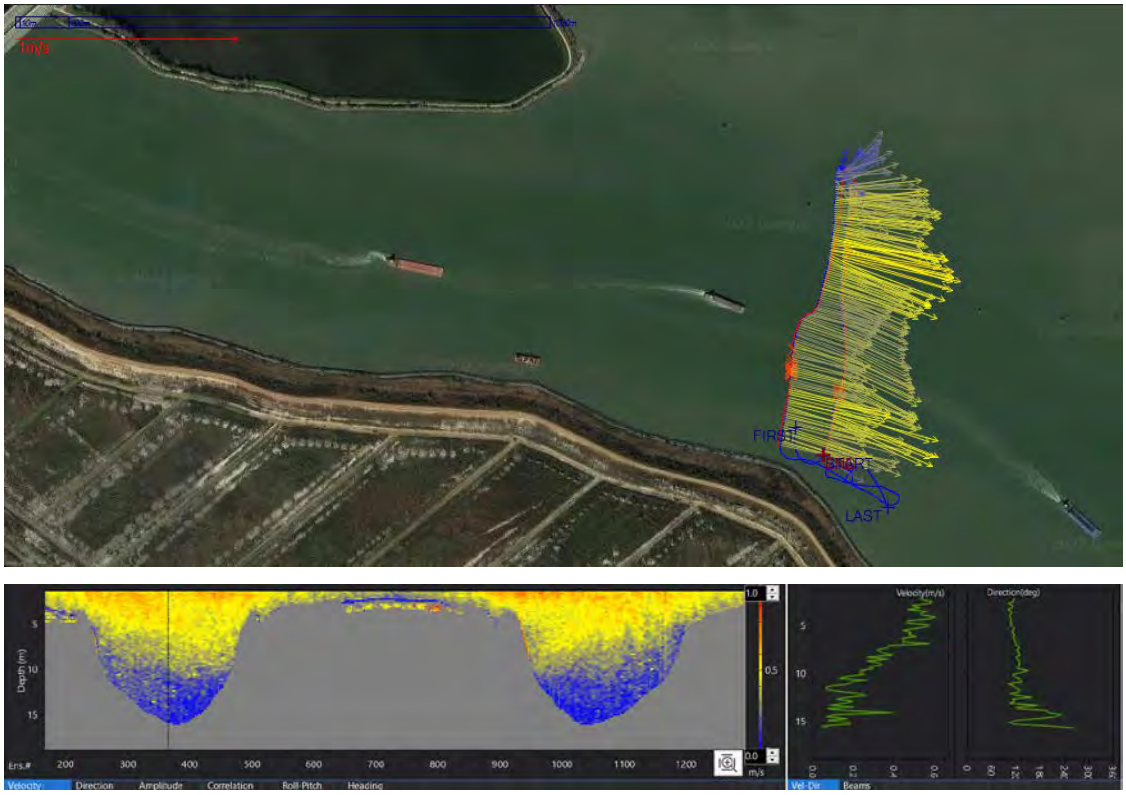

Figure C-2: Vessel track and velocity map for VM run: 20220201_FHB1_Ebb_Data.

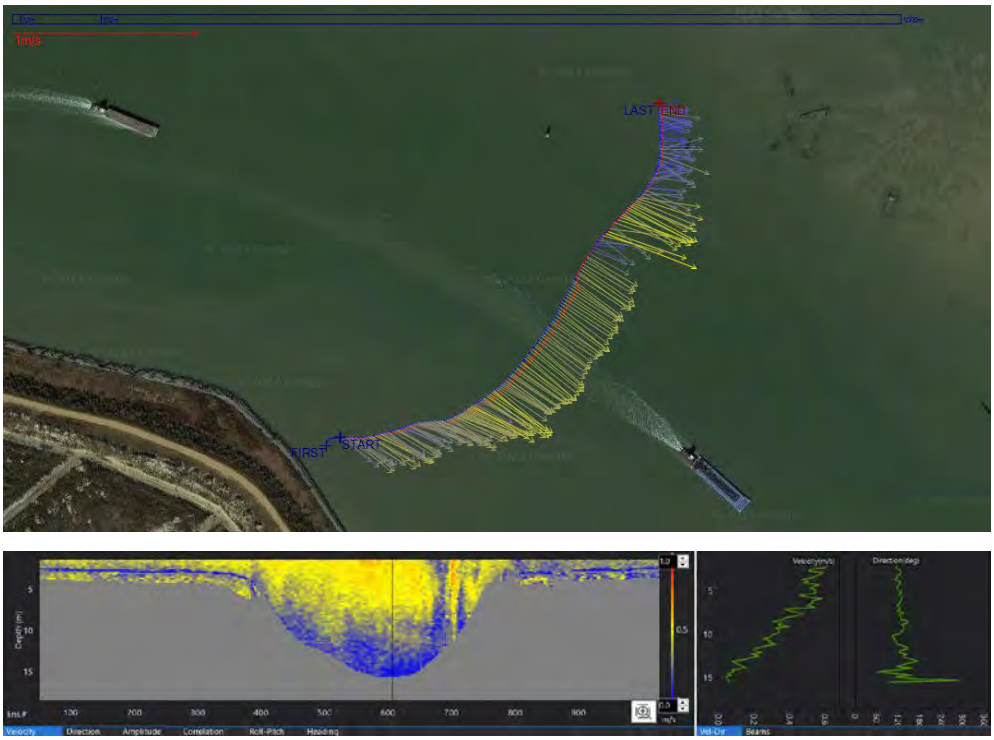

Figure C-3: Vessel track and velocity map for VM run: 20220201_FHB2_Ebb_Data.

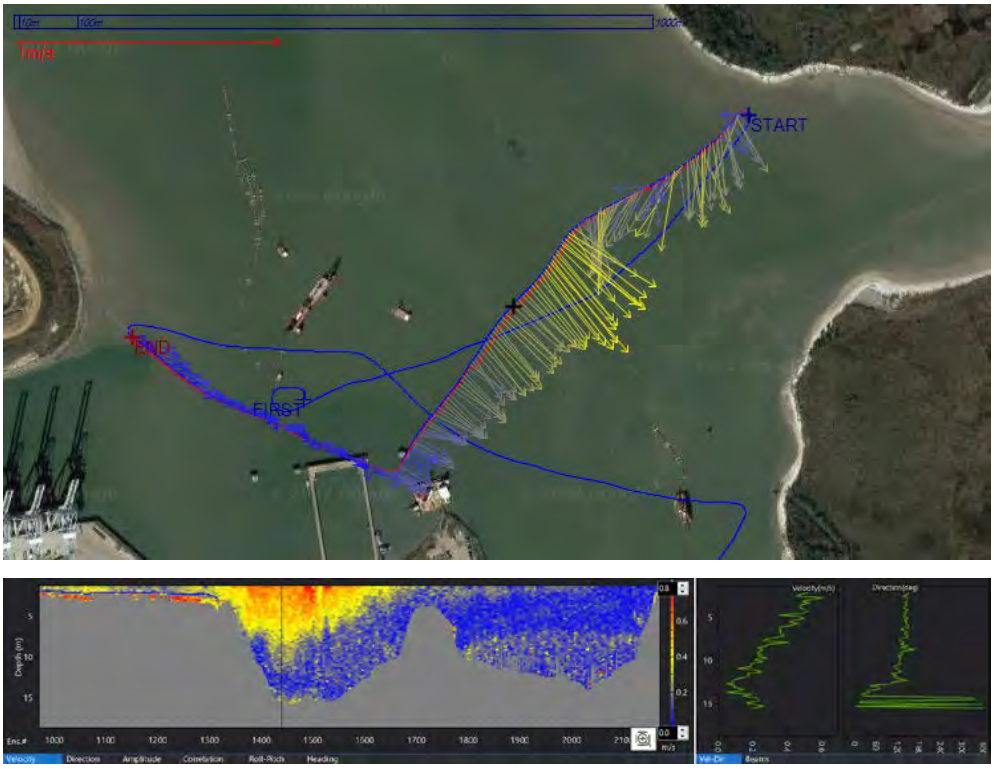

Figure C-4: Vessel track and velocity map for VM run: 20220201_MorgansPoint1_Ebb_Data.

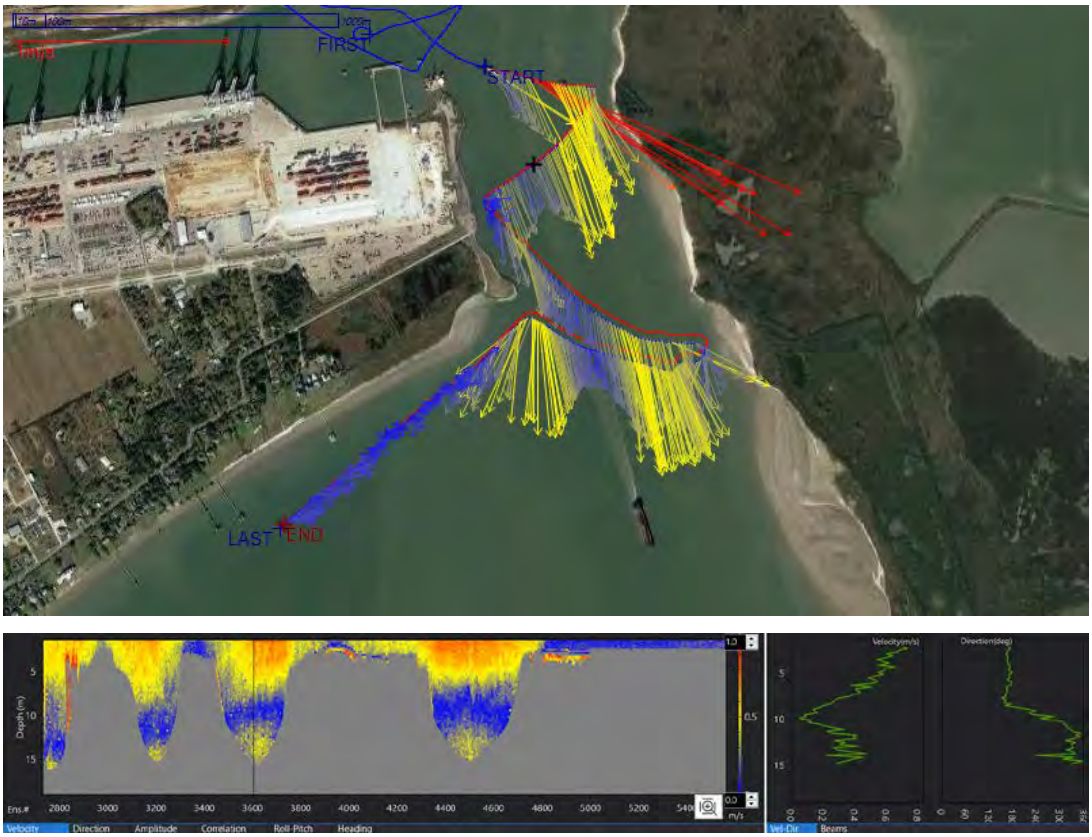

Figure C-5: Vessel track and velocity map for VM run: 20220201_MorgansPoint2_Ebb_Data.

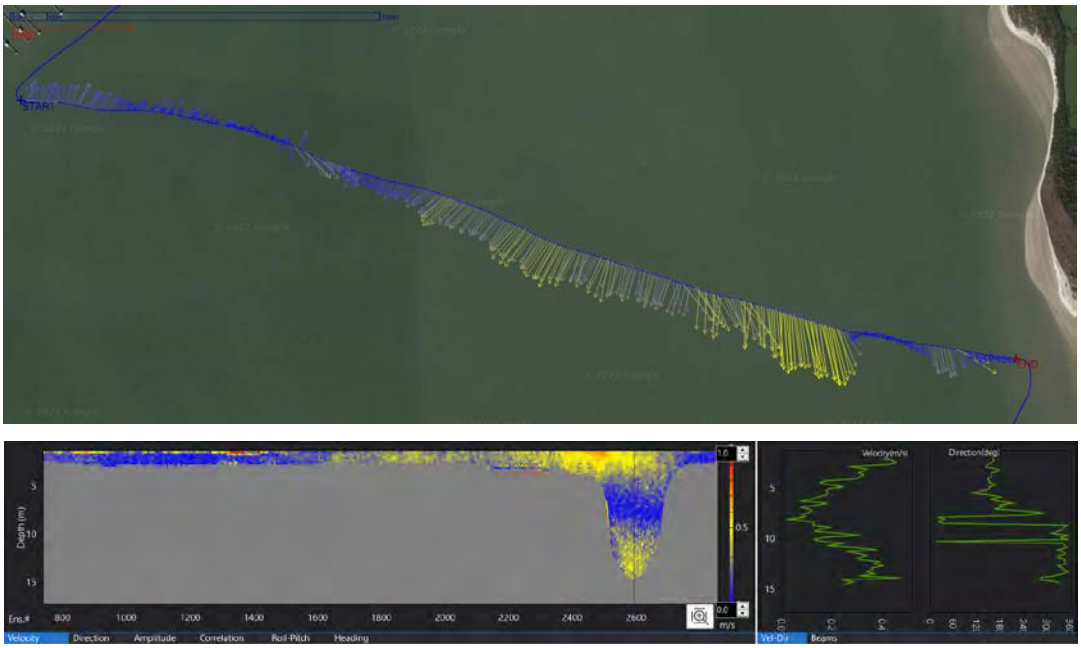

Figure C-6: Vessel track and velocity map for VM run: 20220201_SanJacBay1_Ebb_Data.

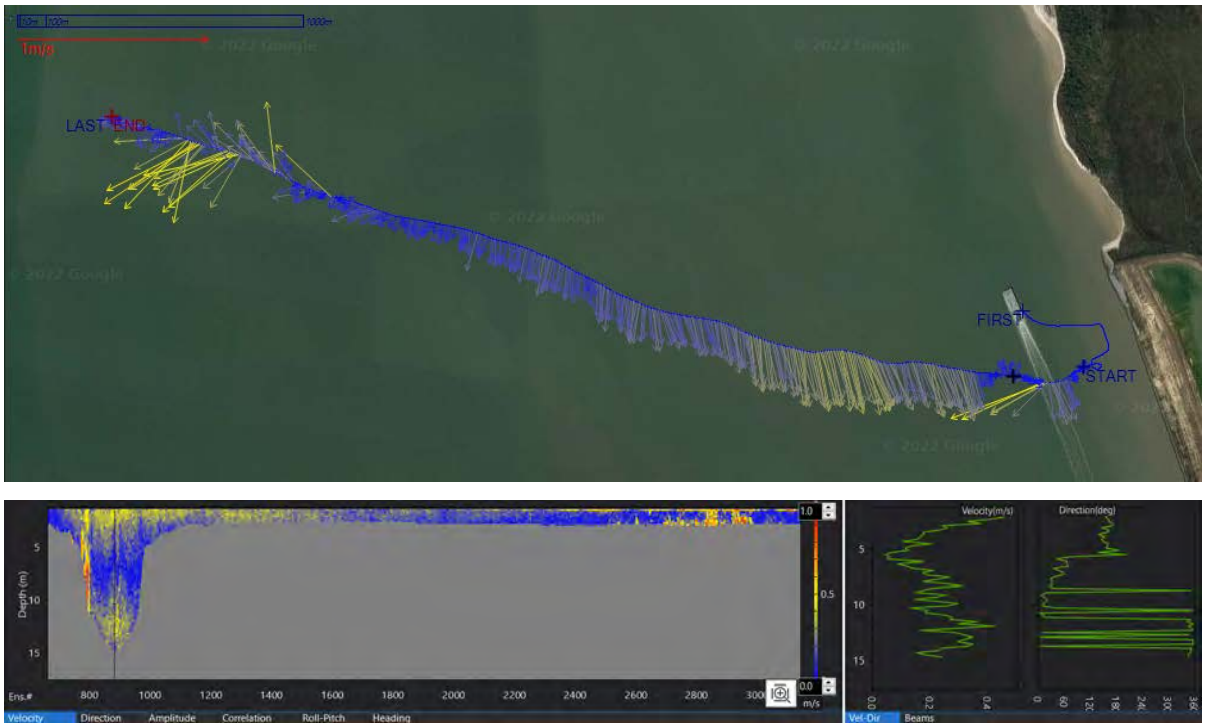

Figure C-7: Vessel track and velocity map for VM run: 20220201_SanJacBay2_Ebb_Data.

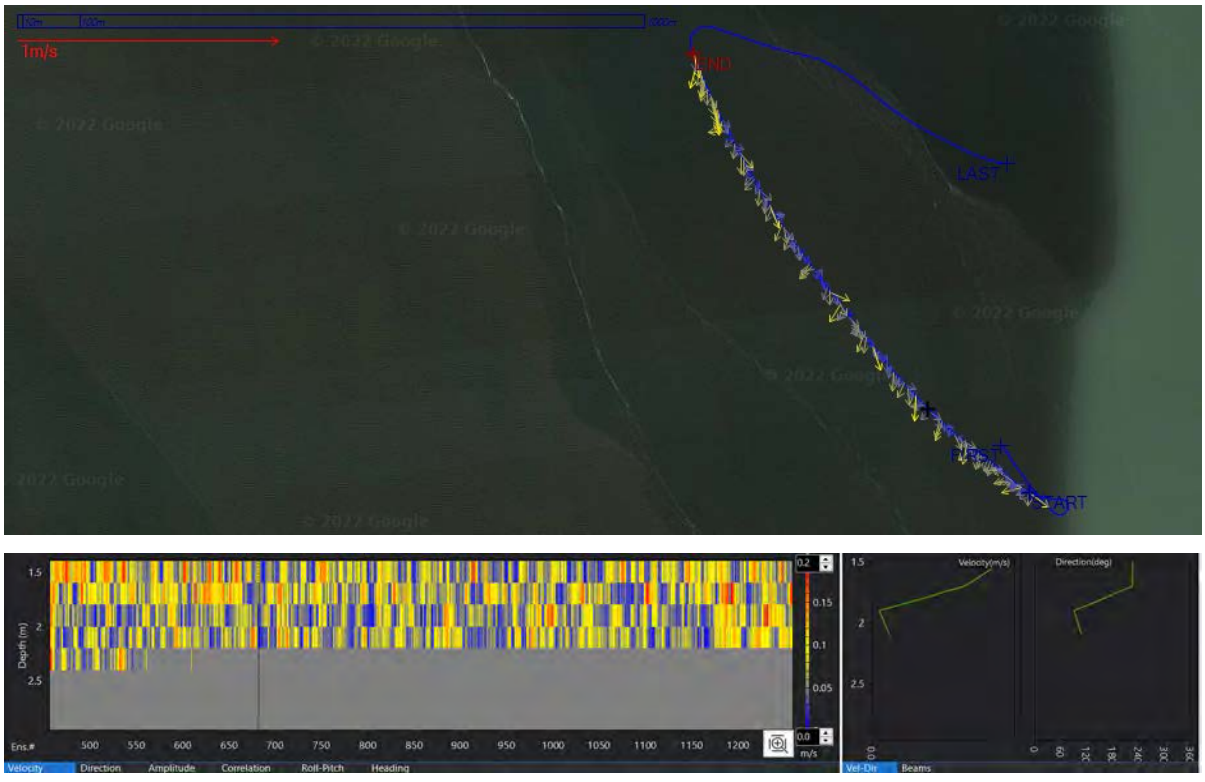

Figure C-8: Vessel track and velocity map for VM run: 20220201_TrinityBay_Ebb_Data.

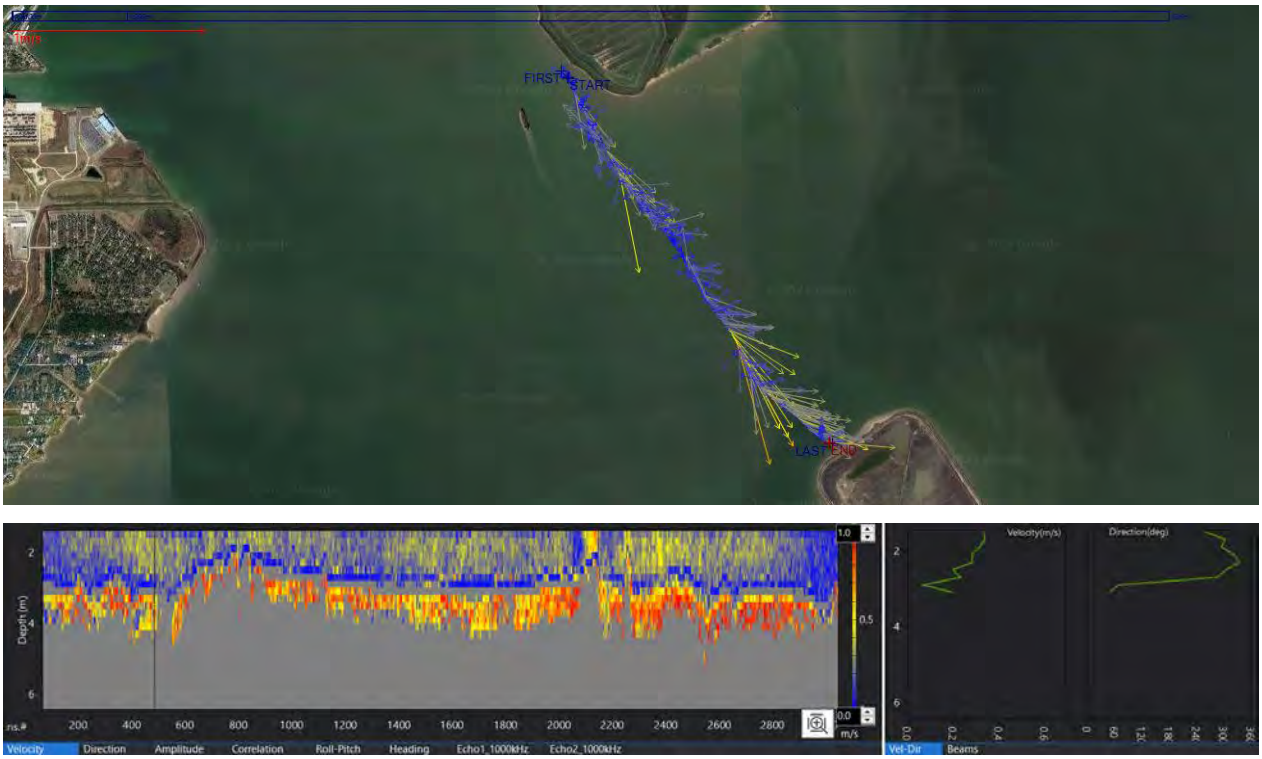

Figure C-9: Vessel track and velocity map for VM run: 20220210_AtkinsonIslandSouth_Flood _Data.

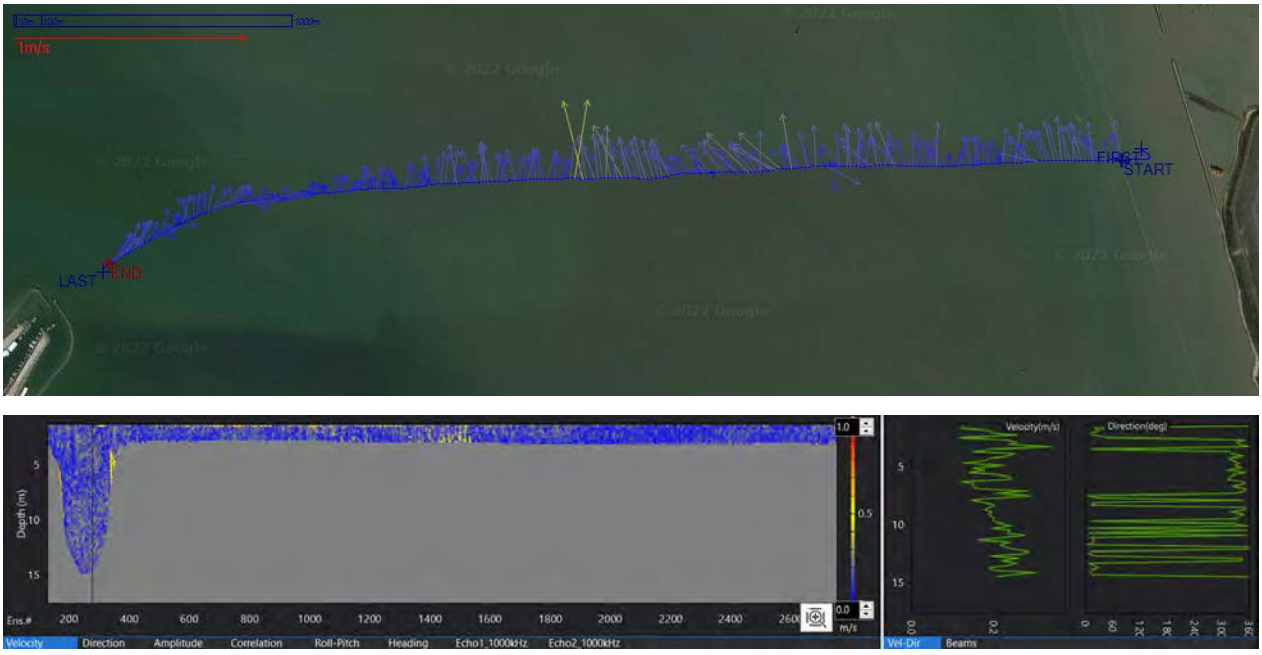

Figure C-10: Vessel track and velocity map for VM run: 20220210_BayportChannelNorth_Flood _Data

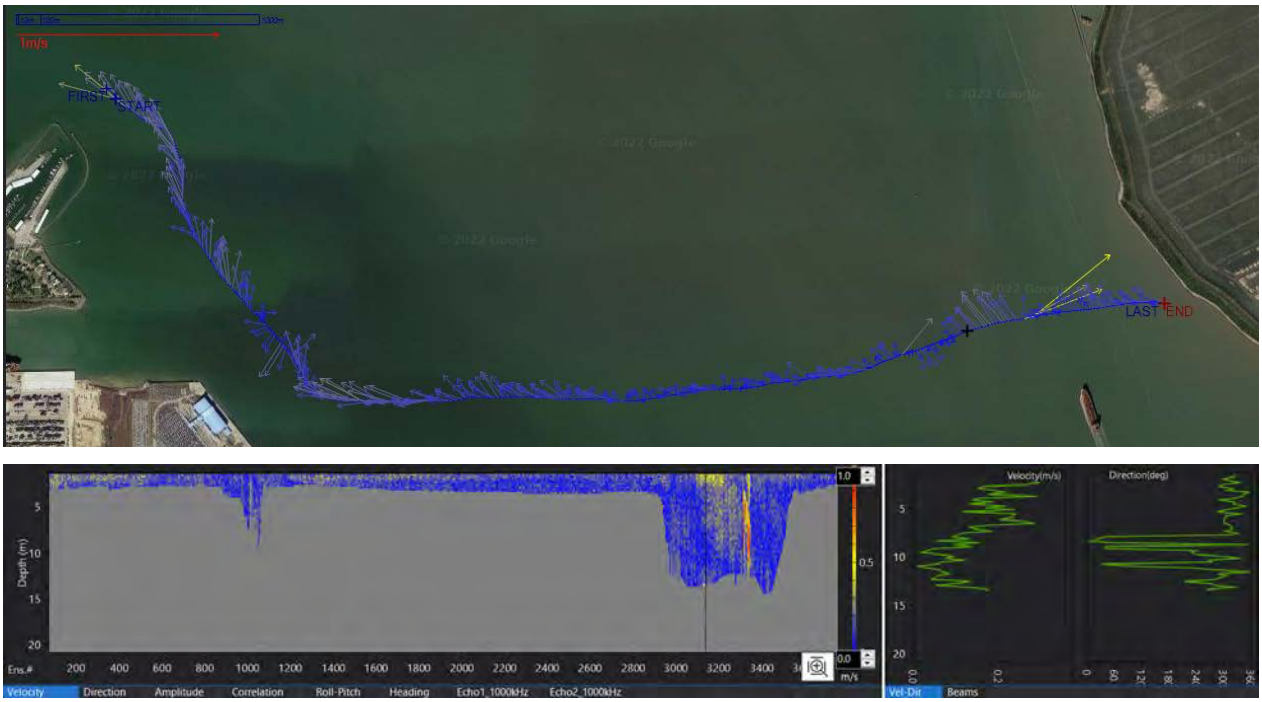

Figure C-11: Vessel track and velocity map for VM run: 20220210_BayportChannelSouth_Flood _Data.

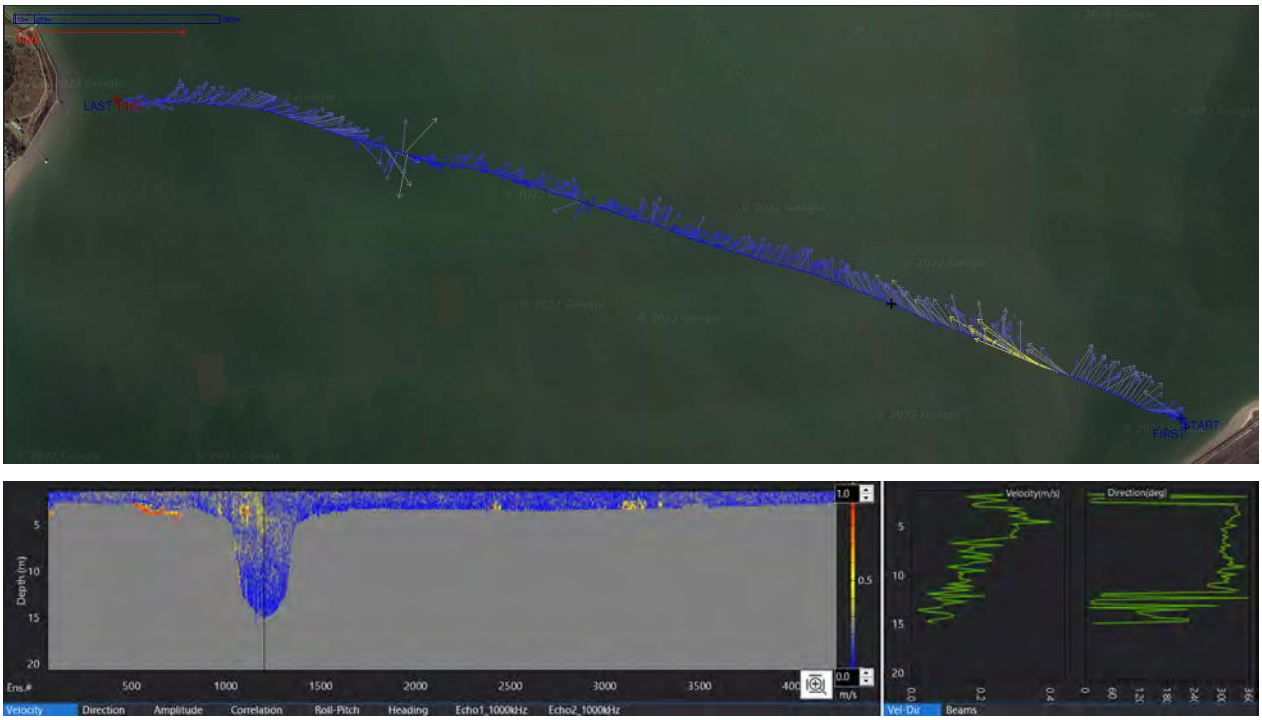

Figure C-12: Vessel track and velocity map for VM run: 20220210_BluewaterAtoll_Flood_Data.

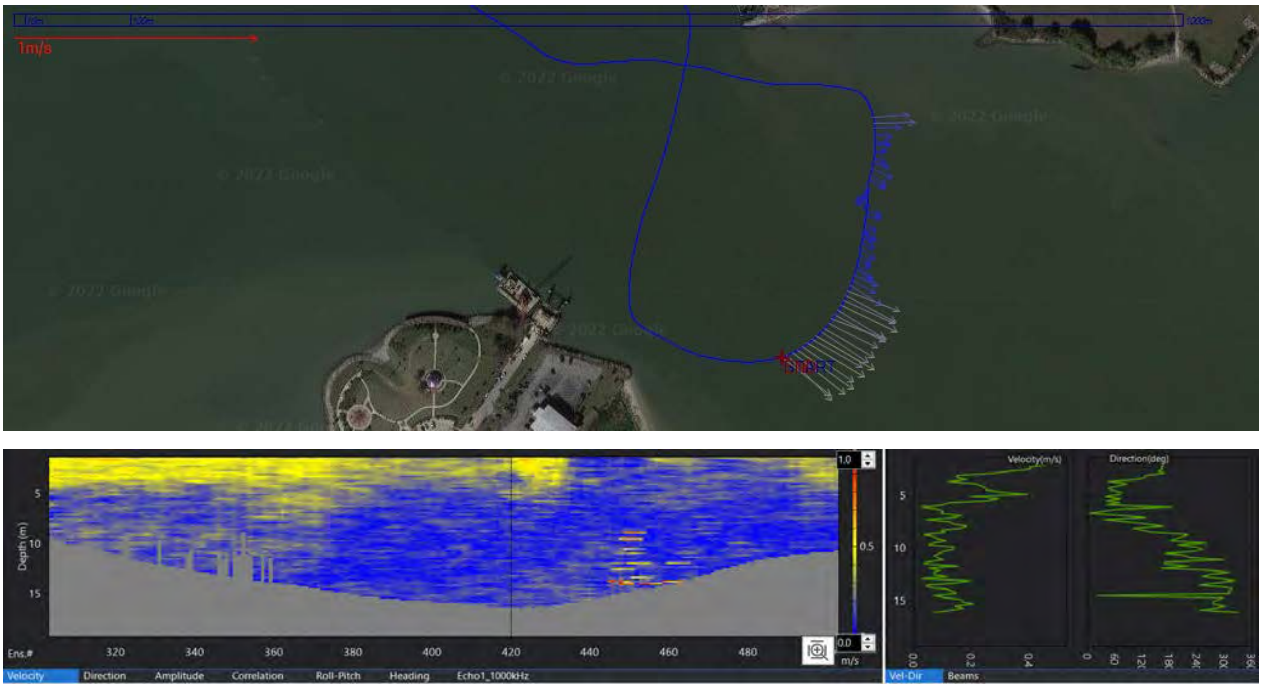

Figure C-13: Vessel track and velocity map for VM run: 20220210_BuffaloBayou1_Ebb_Data.

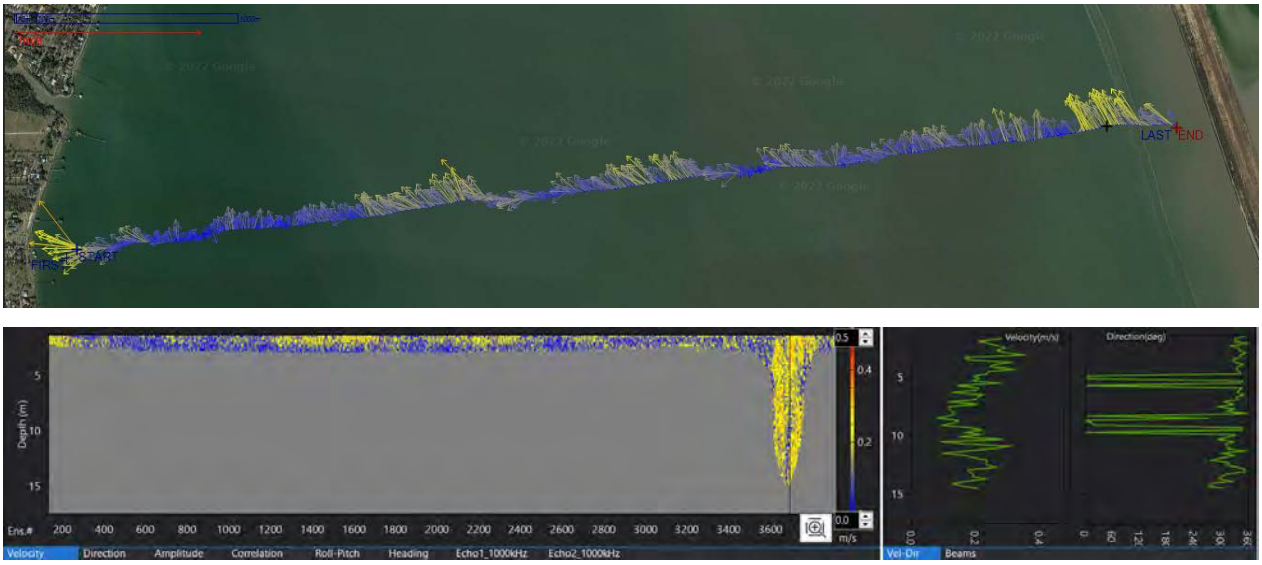

Figure C-14: Vessel track and velocity map for VM run: 20220210_SanJacBay3_Flood_Data.

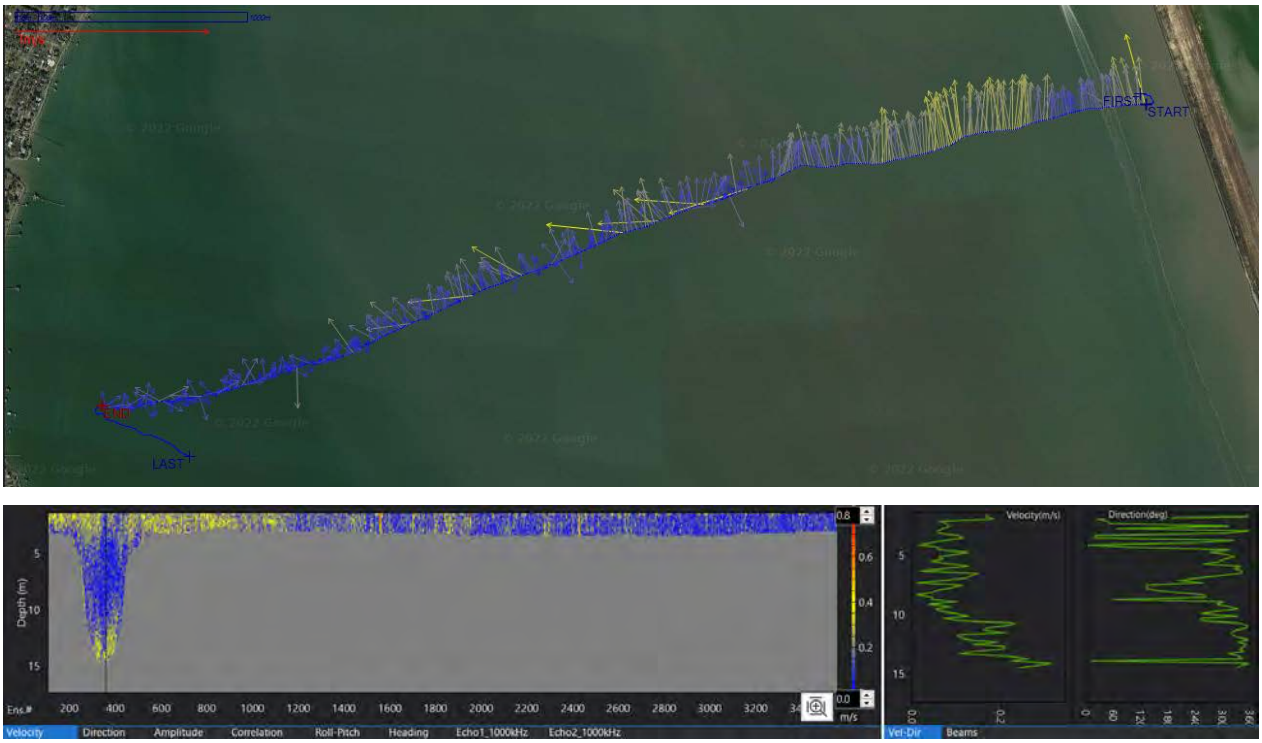

Figure C-15: Vessel track and velocity map for VM run: 20220419_SanJacBay4_Flood_Data.

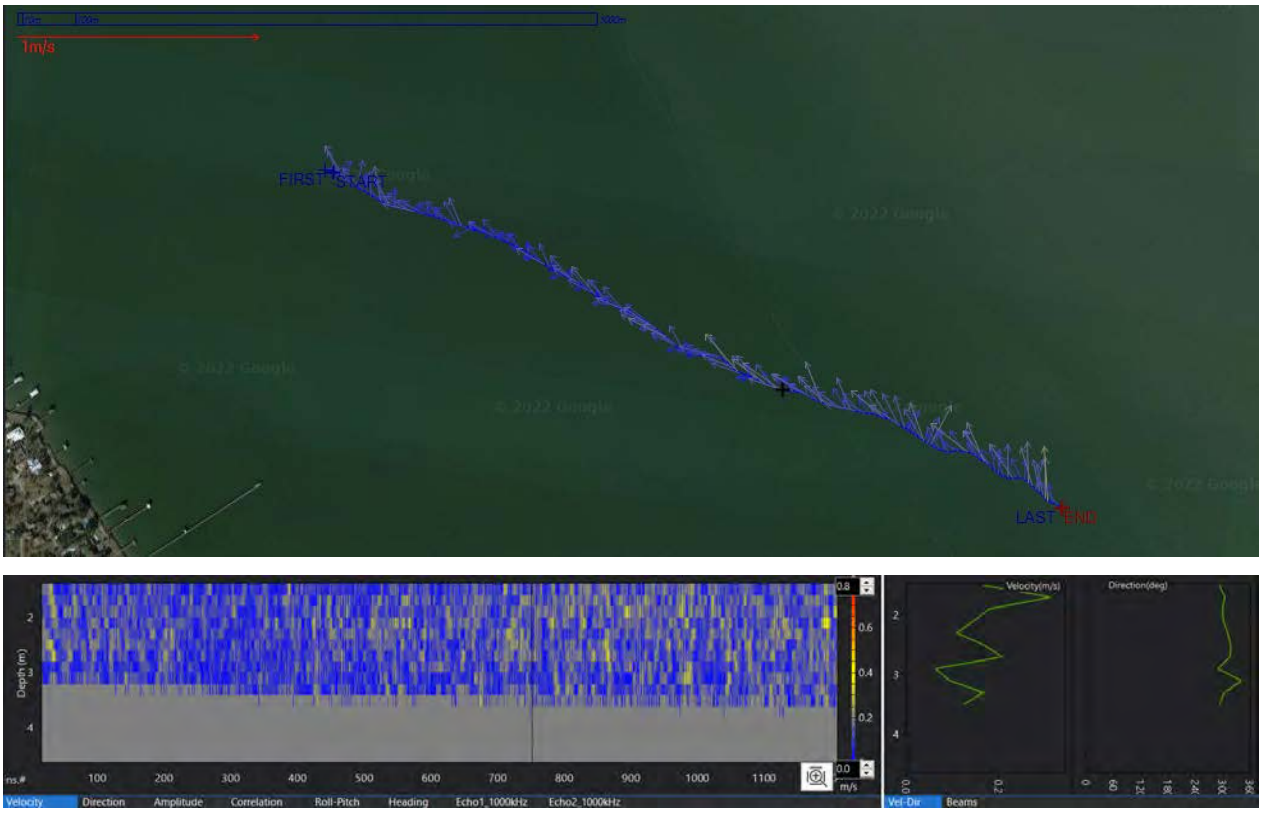

Figure C-16: Vessel track and velocity map for VM run: 20220419_SanJacBay5_Flood_Data.

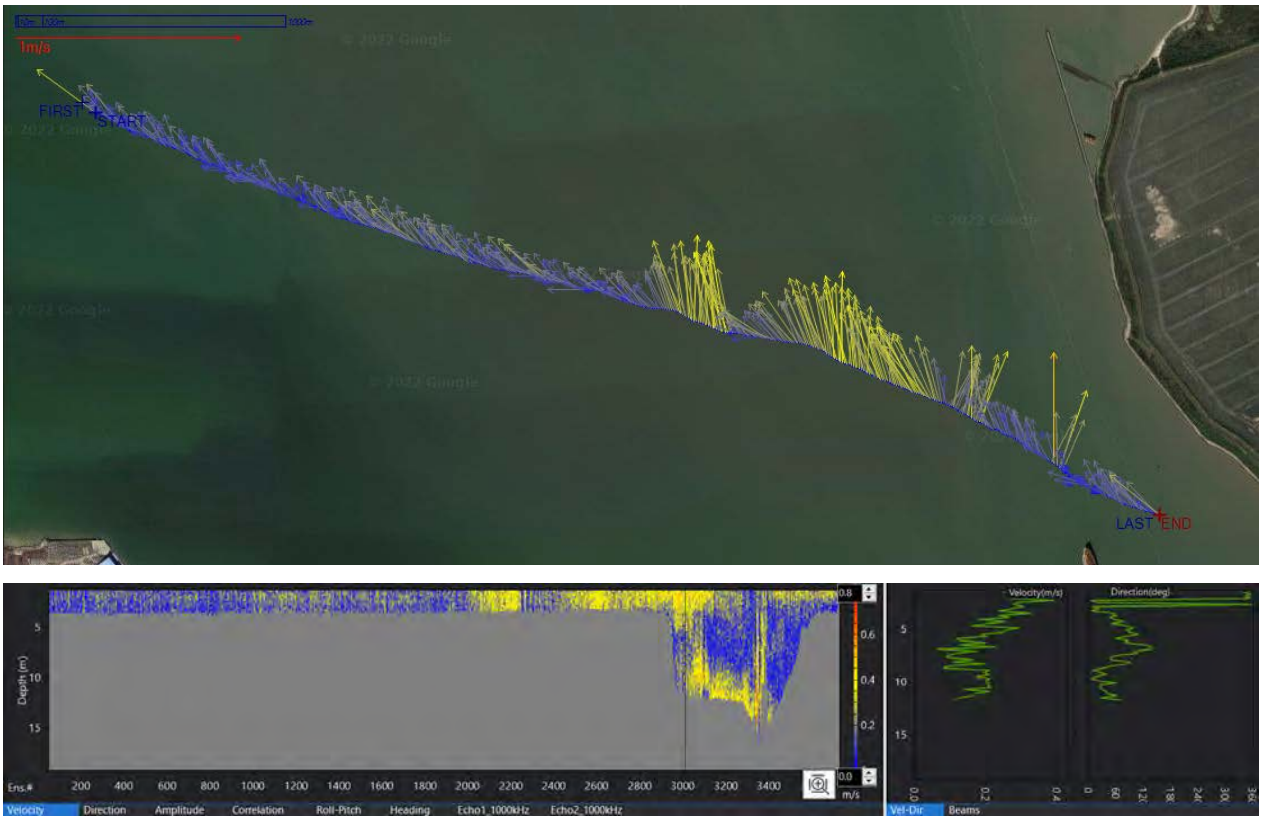

Figure C-17: Vessel track and velocity map for VM run: 20220419_SanJacBay6_Flood_Data.

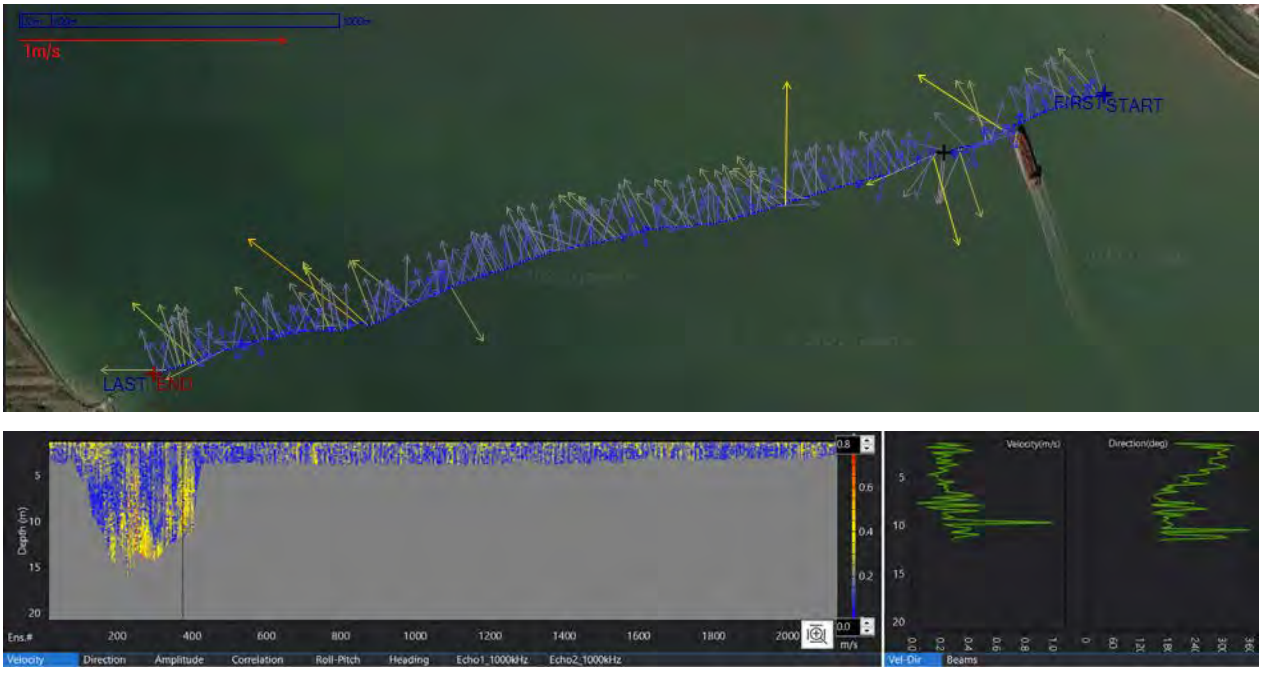

Figure C-18: Vessel track and velocity map for VM run: 20220419_SanJacBay7_Flood_Data.

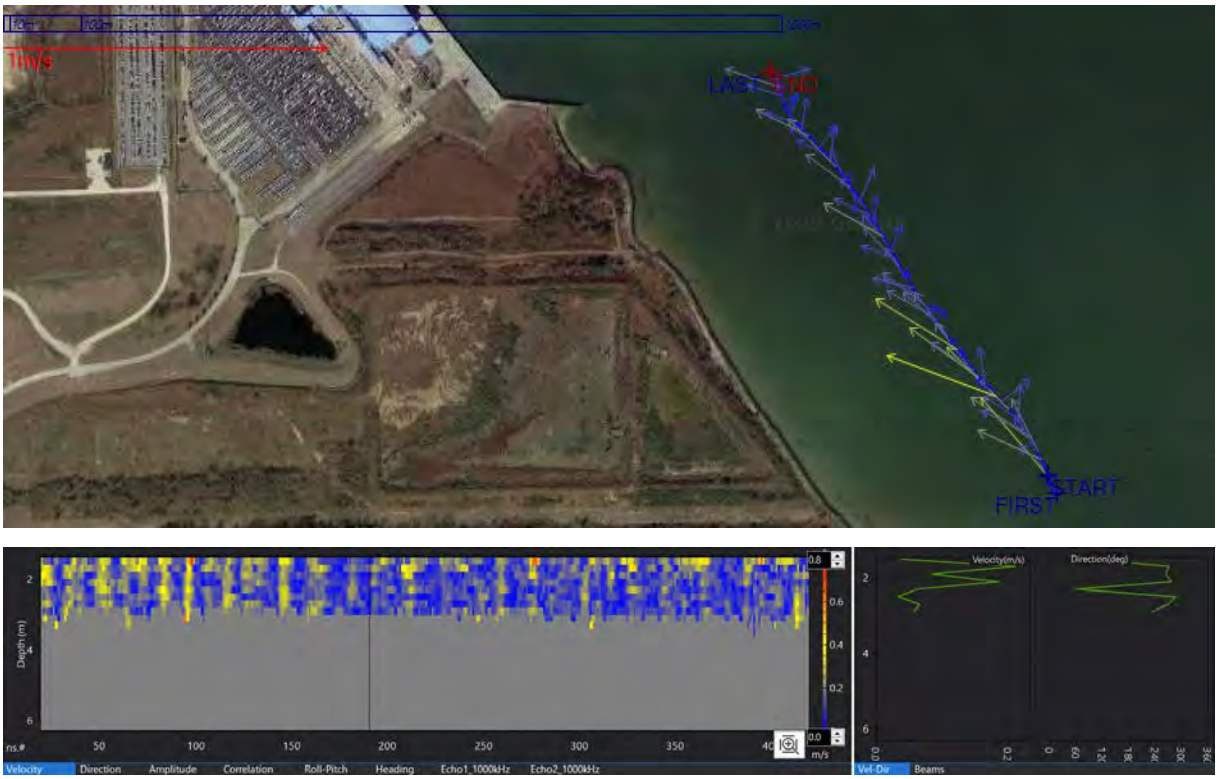

Figure C-19: Vessel track and velocity map for VM run: 20220419_SanJacBay8_Flood_Data.

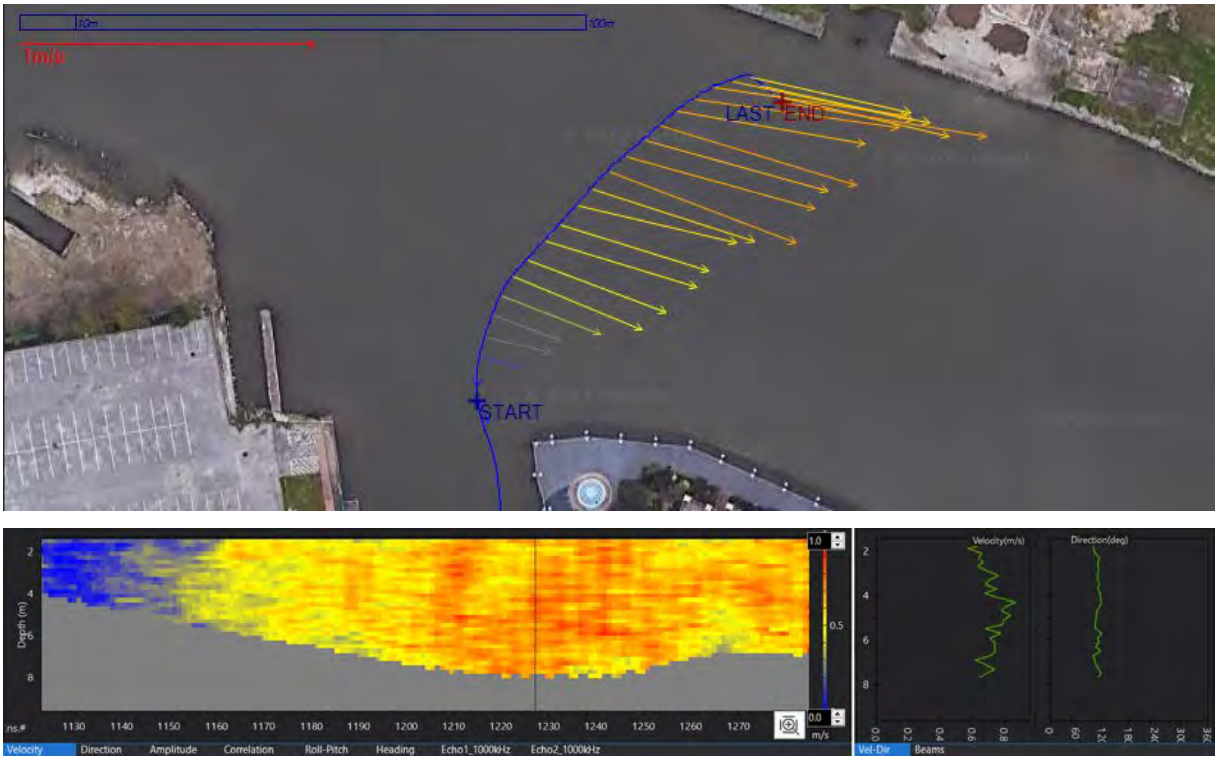

Figure C-20: Vessel track and velocity map for VM run: 20220421_Kemah_1_Ebb_Data.

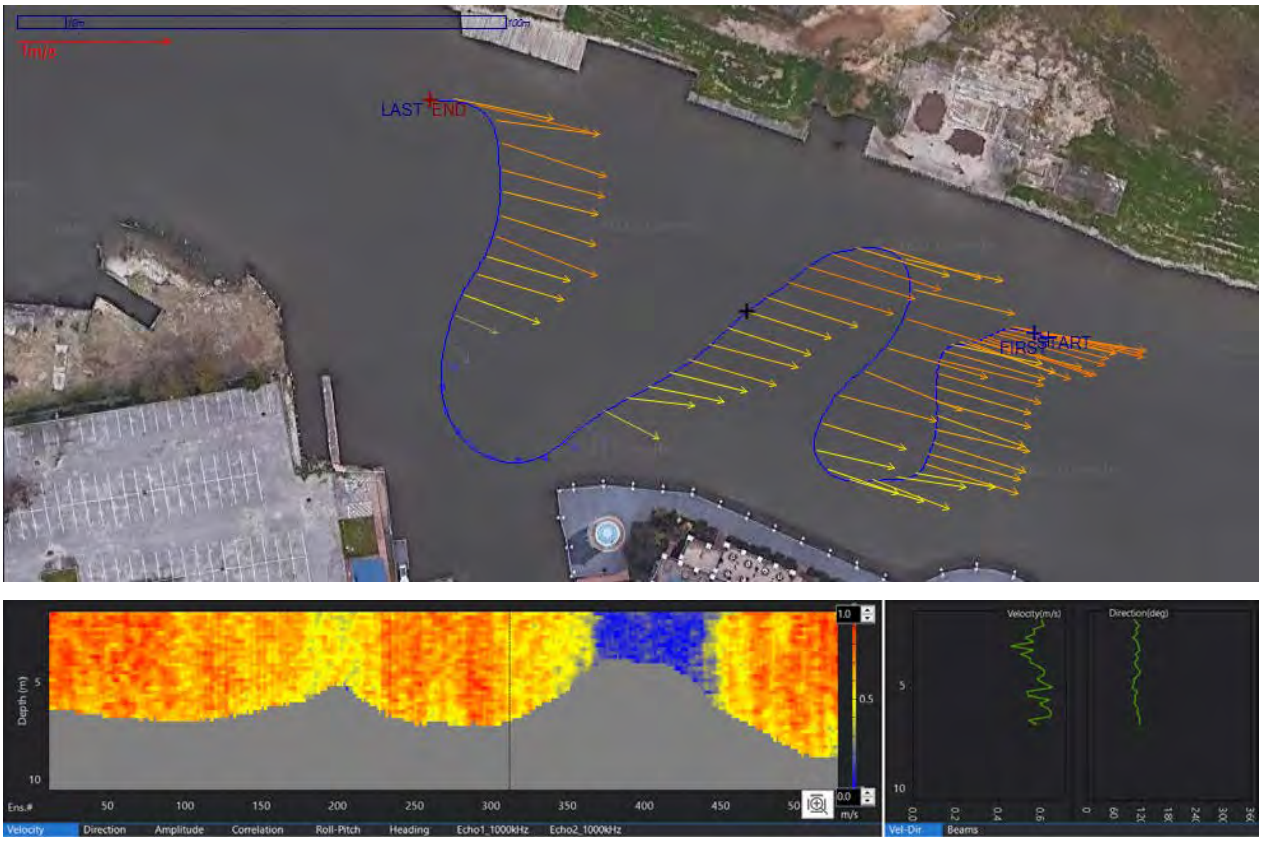

Figure C-21: Vessel track and velocity map for VM run: 20220421_Kemah_3_Ebb_Data.

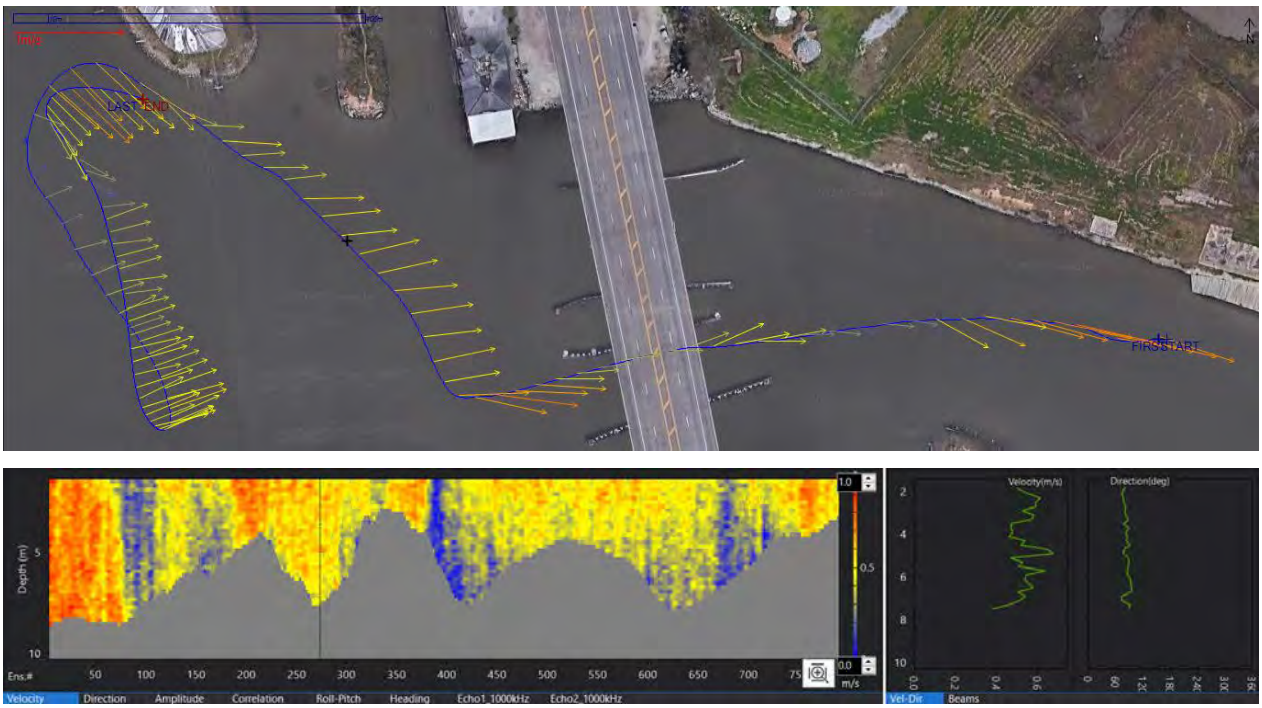

Figure C-22: Vessel track and velocity map for VM run: 20220421_Kemah_4_Ebb_Data.

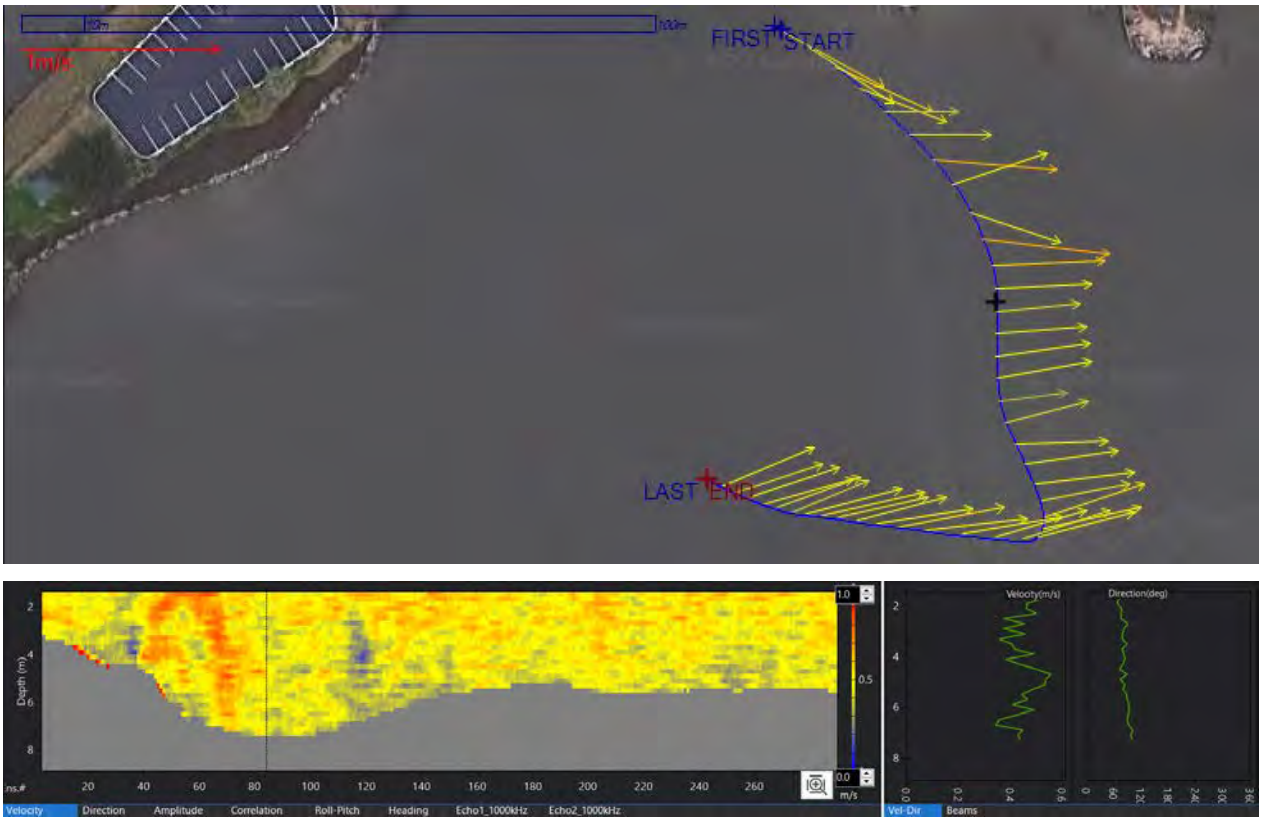

Figure C-23: Vessel track and velocity map for VM run: 20220421_Kemah_5_Ebb_Data.

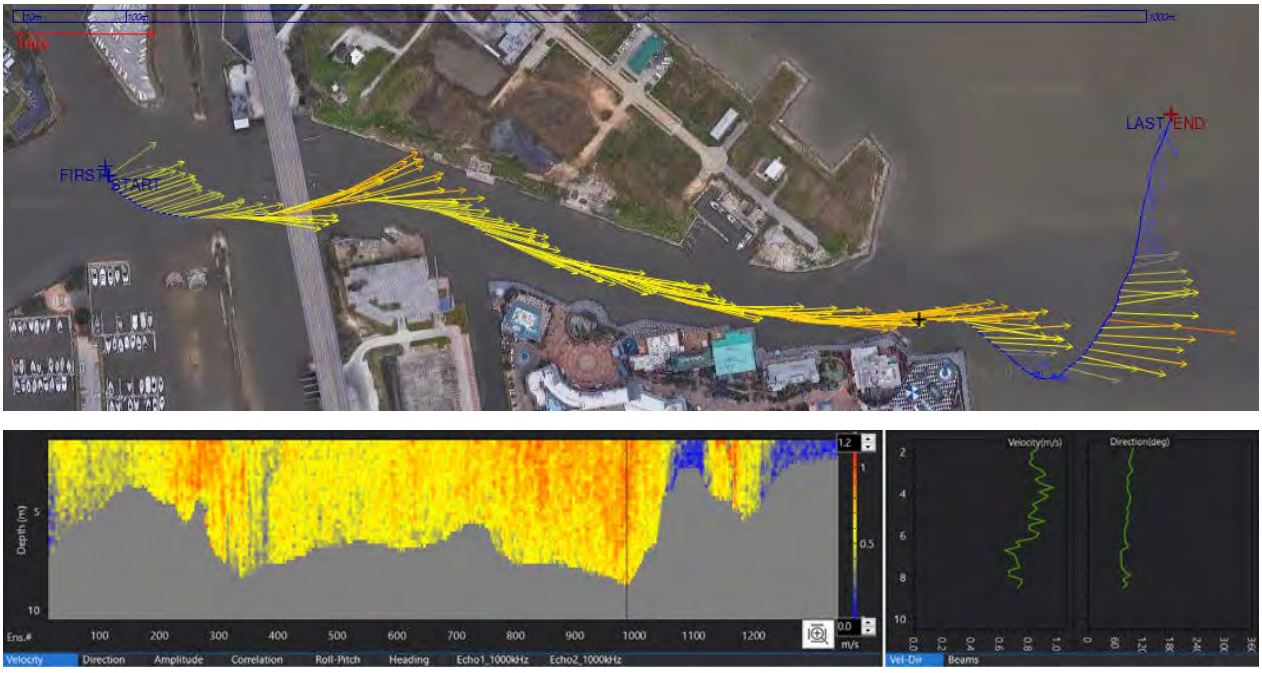

Figure C-24: Vessel track and velocity map for VM run: 20220421_Kemah_6_Ebb_Data.

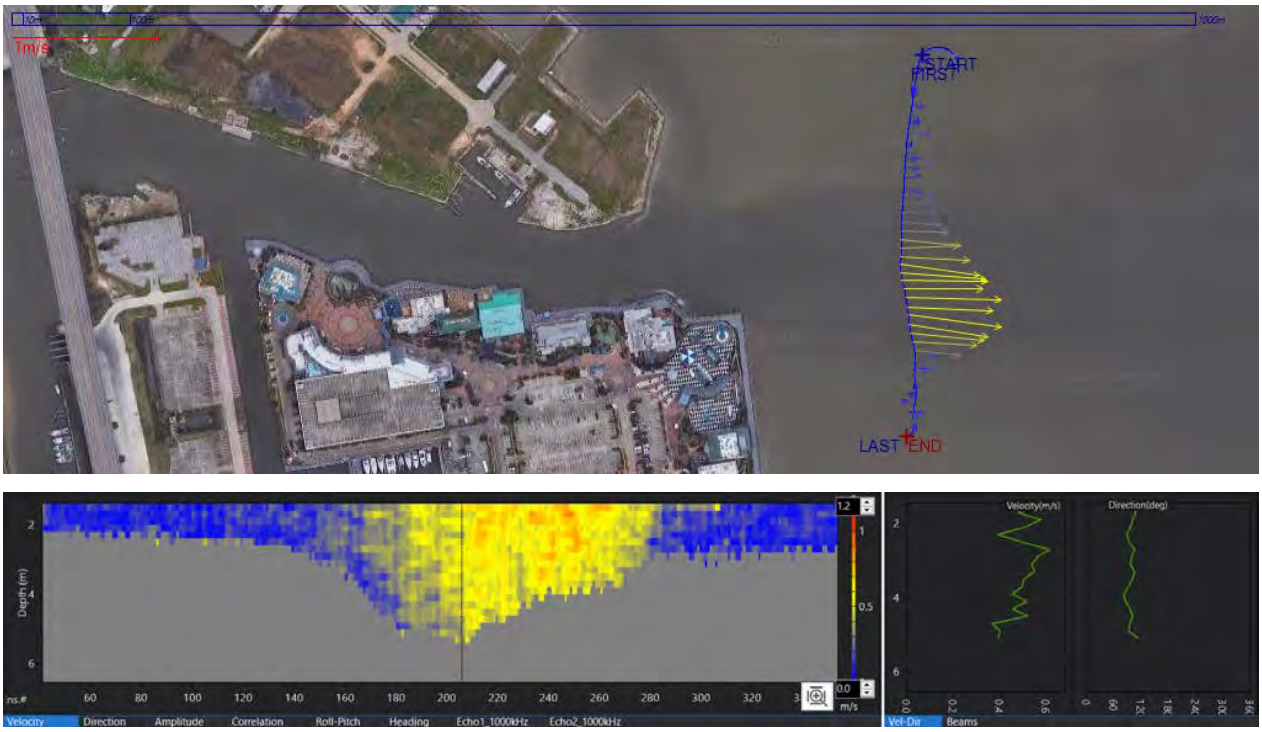

Figure C-25: Vessel track and velocity map for VM run: 20220421_Kemah_7_Ebb_Data.

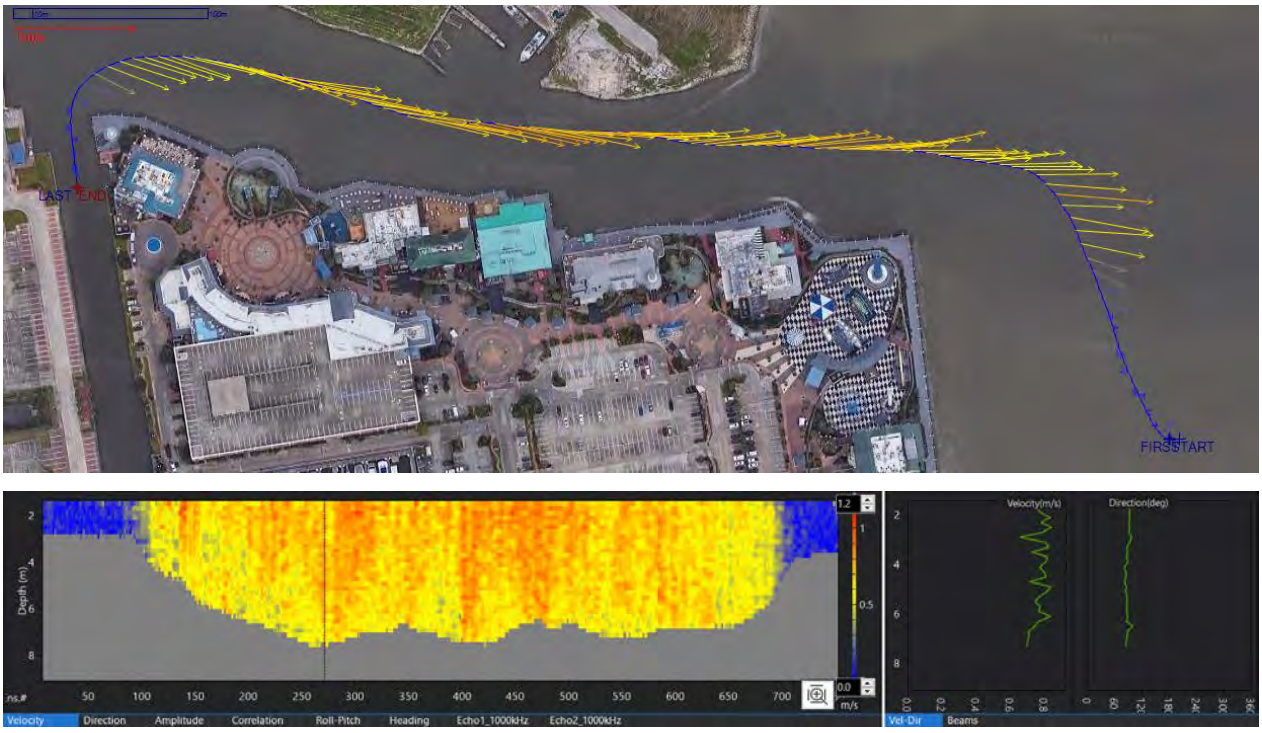

Figure C-26: Vessel track and velocity map for VM run: 20220421_Kemah_8_Ebb_Data.

13 Appendix D: Measured Salinity and Temperature Profiles

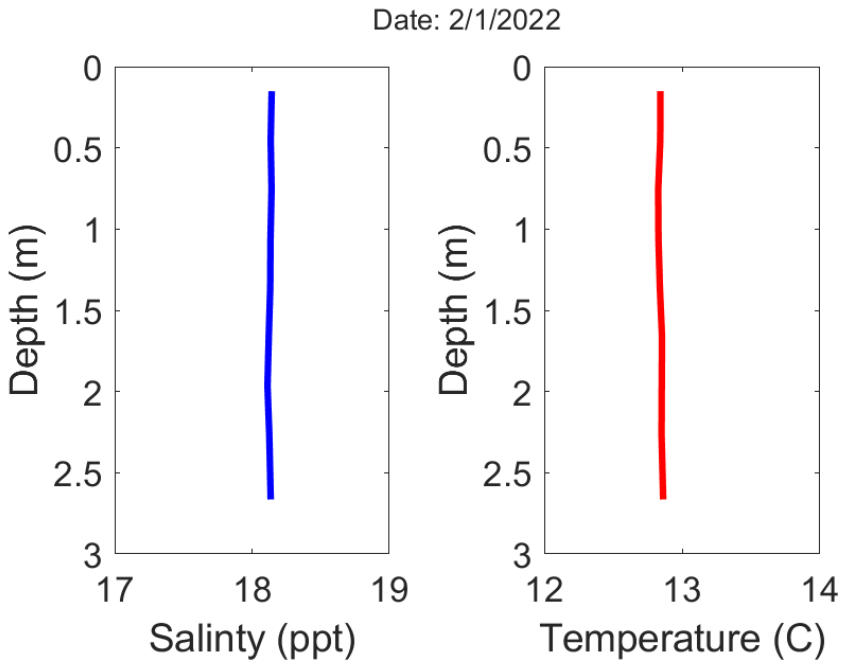

Figure D-1: Measured salinity and temperature profiles for CTD cast: 202221123.

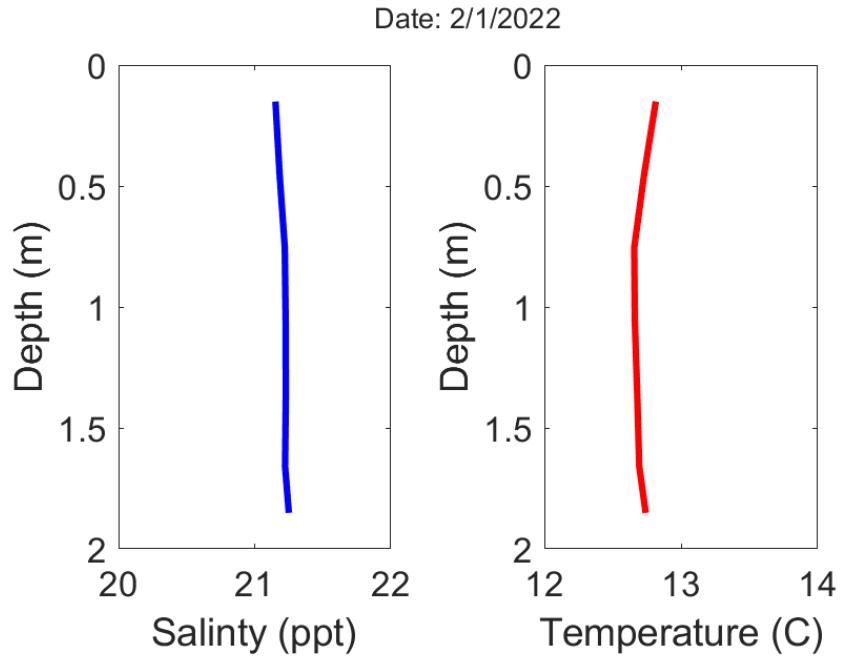

Figure D-2: Measured salinity and temperature profiles for CTD cast: 202221149.

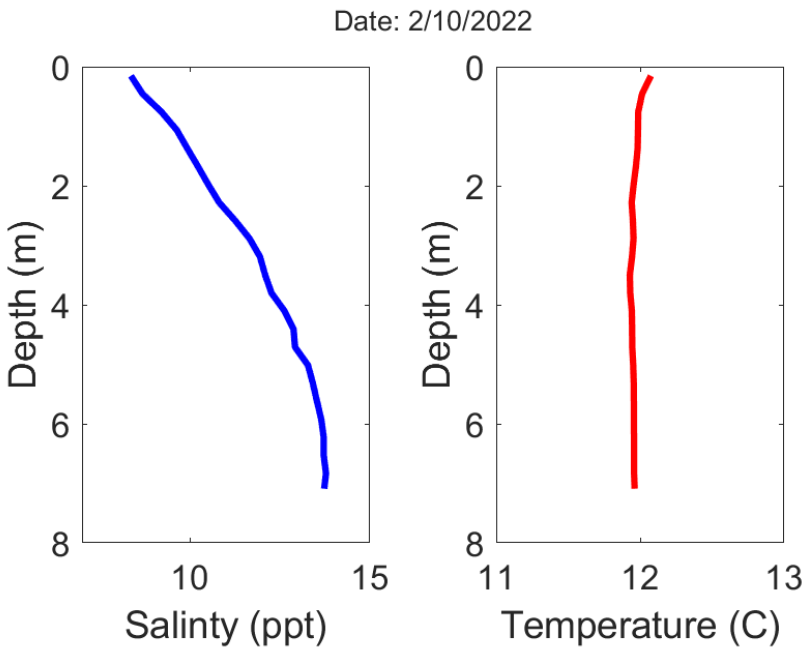

Figure D-3: Measured salinity and temperature profiles for CTD cast: 2022210958.

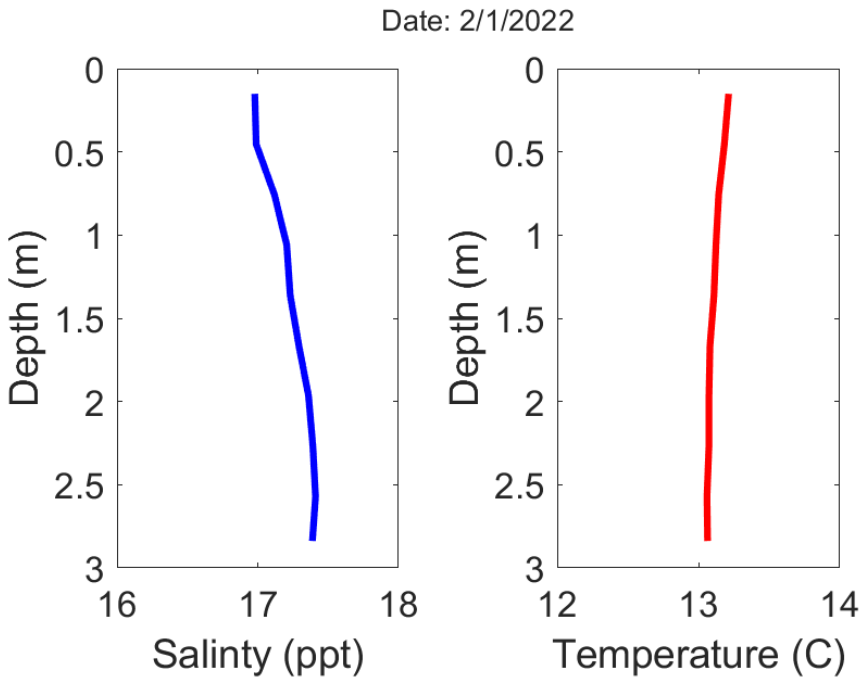

Figure D-4: Measured salinity and temperature profiles for CTD cast: 2022211032.

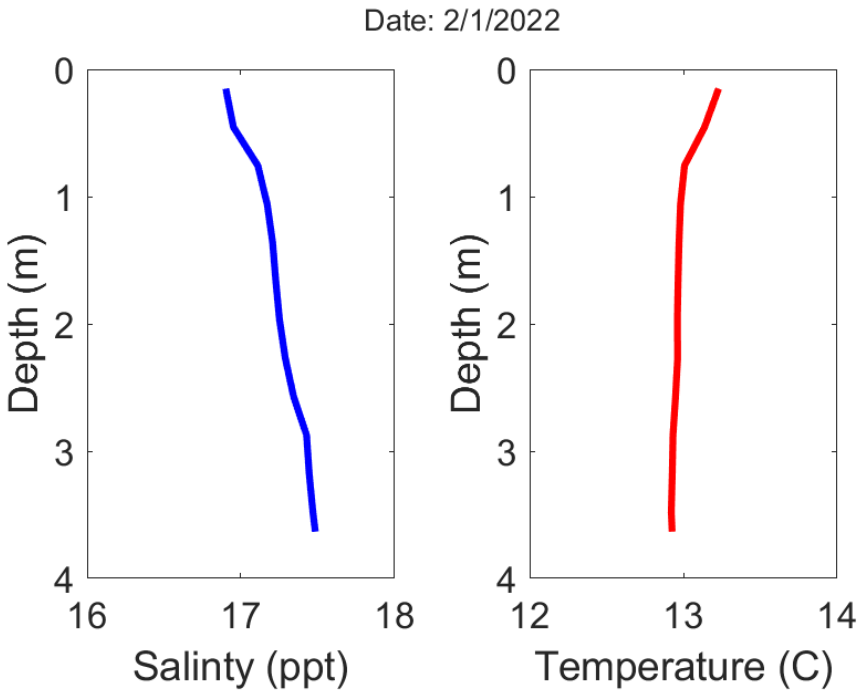

Figure D-5: Measured salinity and temperature profiles for CTD cast: 2022211041.

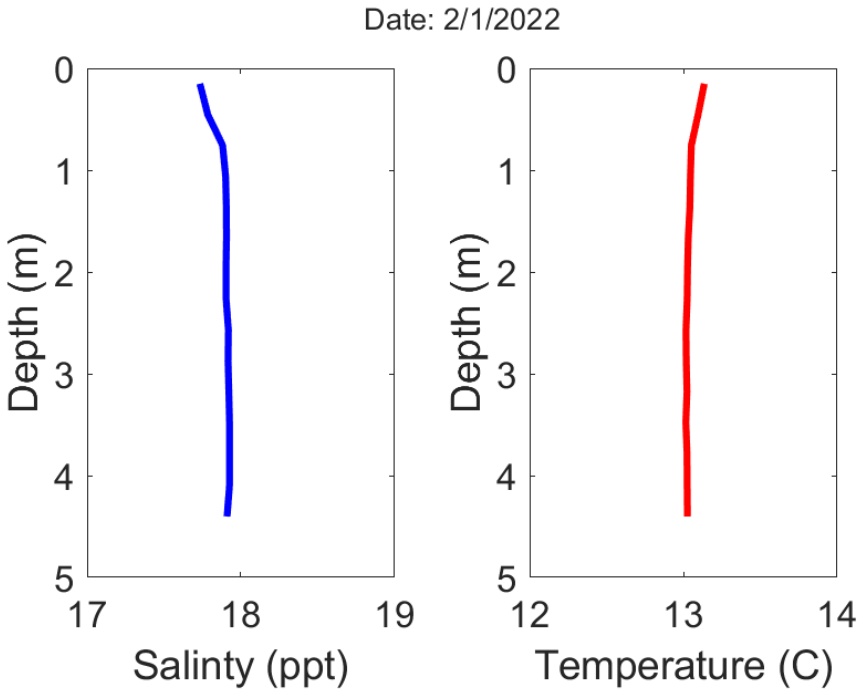

Figure D-6: Measured salinity and temperature profiles for CTD cast: 2022211124.

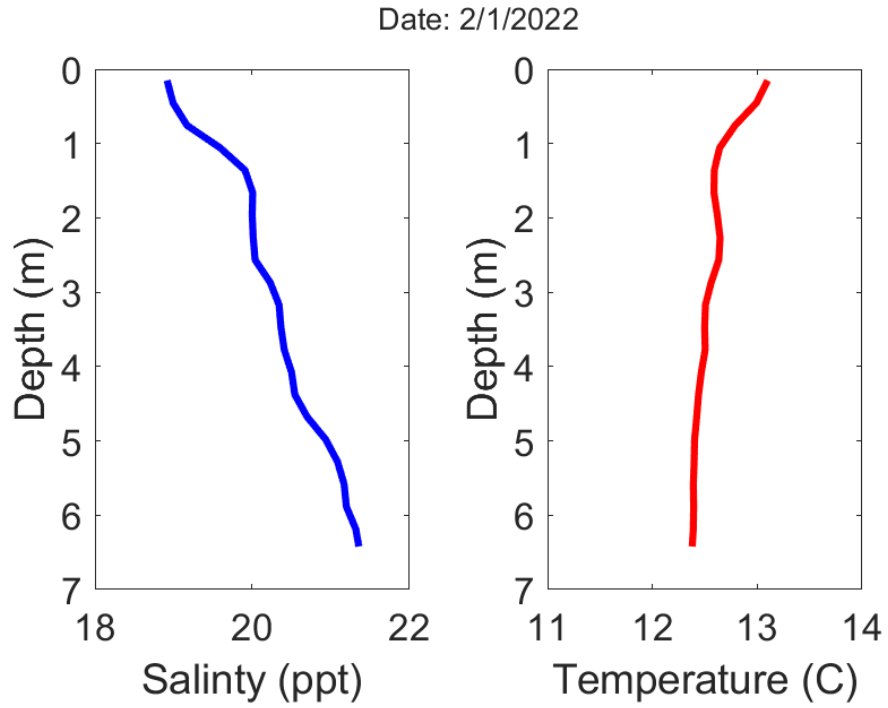

Figure :D-7: Measured salinity and temperature profiles for CTD cast: 2022211253.

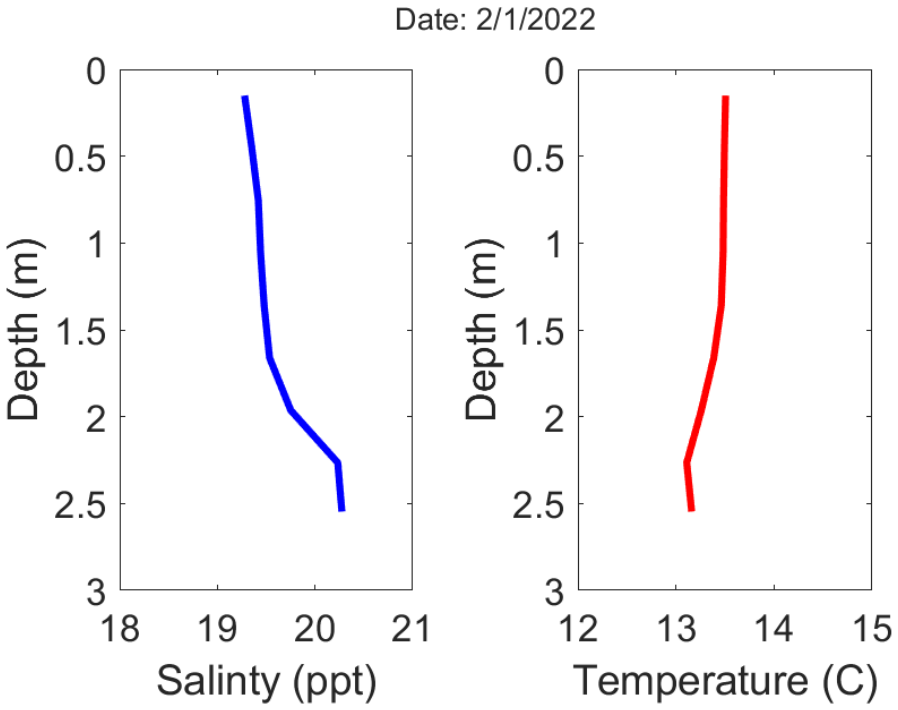

Figure D-8: Measured salinity and temperature profiles for CTD cast: 2022211335.

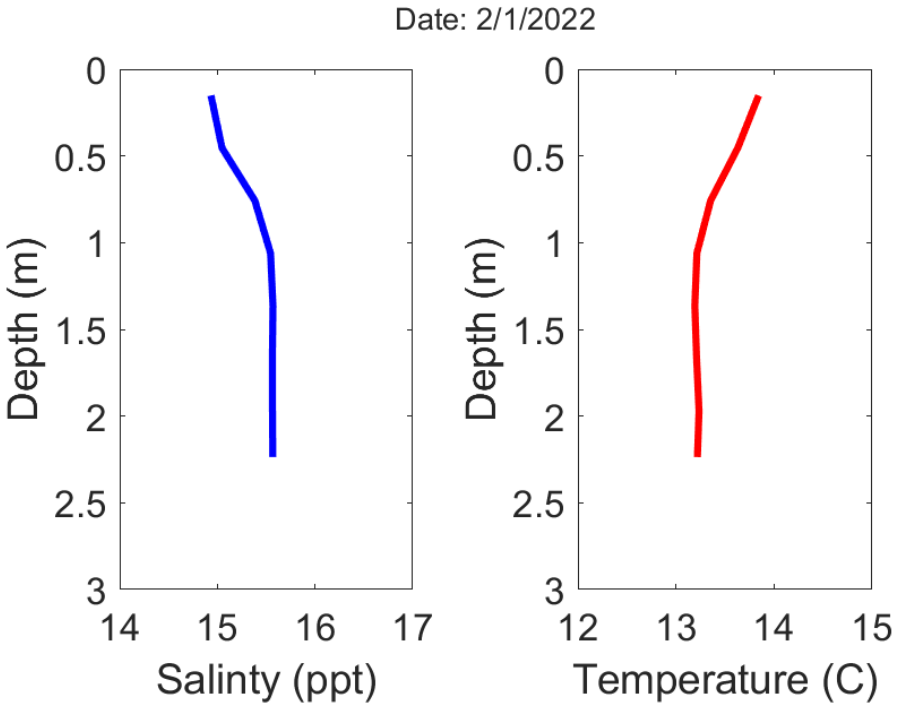

Figure D-9: Measured salinity and temperature profiles for CTD cast: 2022211450.

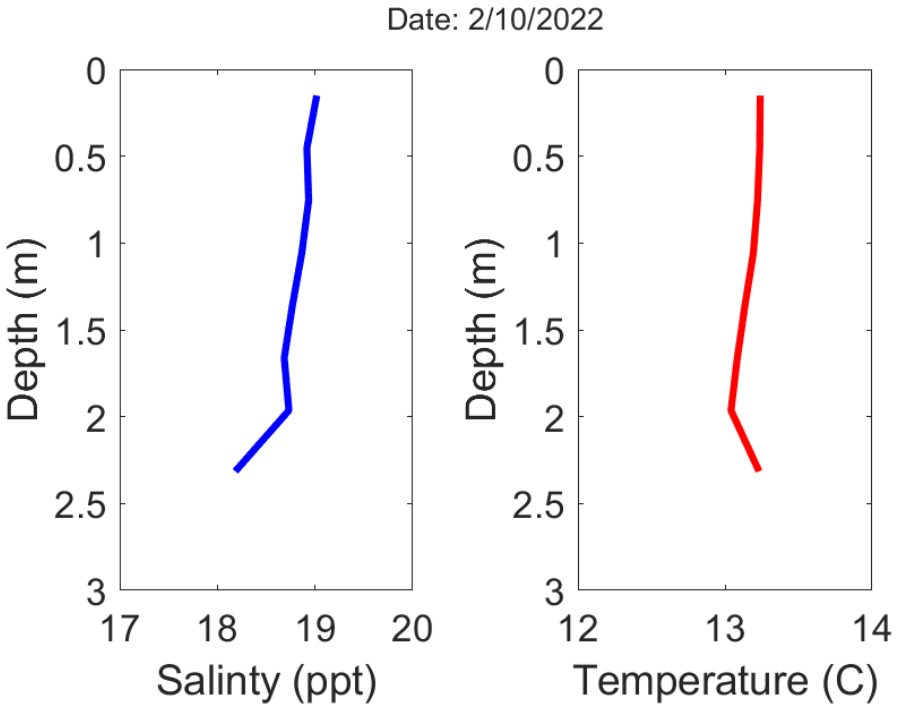

Figure D-10: Measured salinity and temperature profiles for CTD cast: 20222101335.

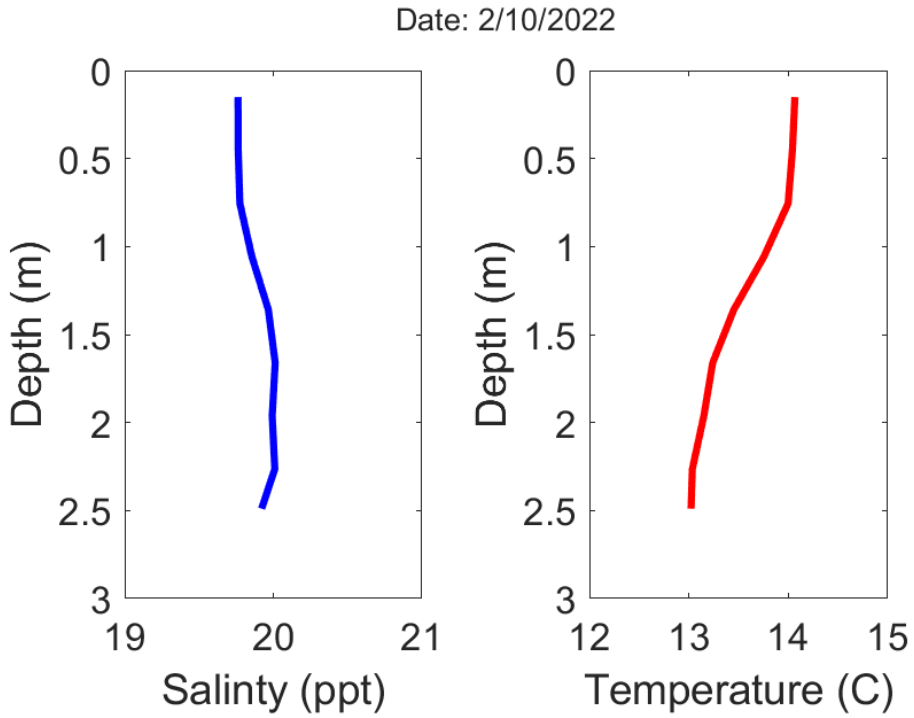

Figure D-11: Measured salinity and temperature profiles for CTD cast: 20222101636.

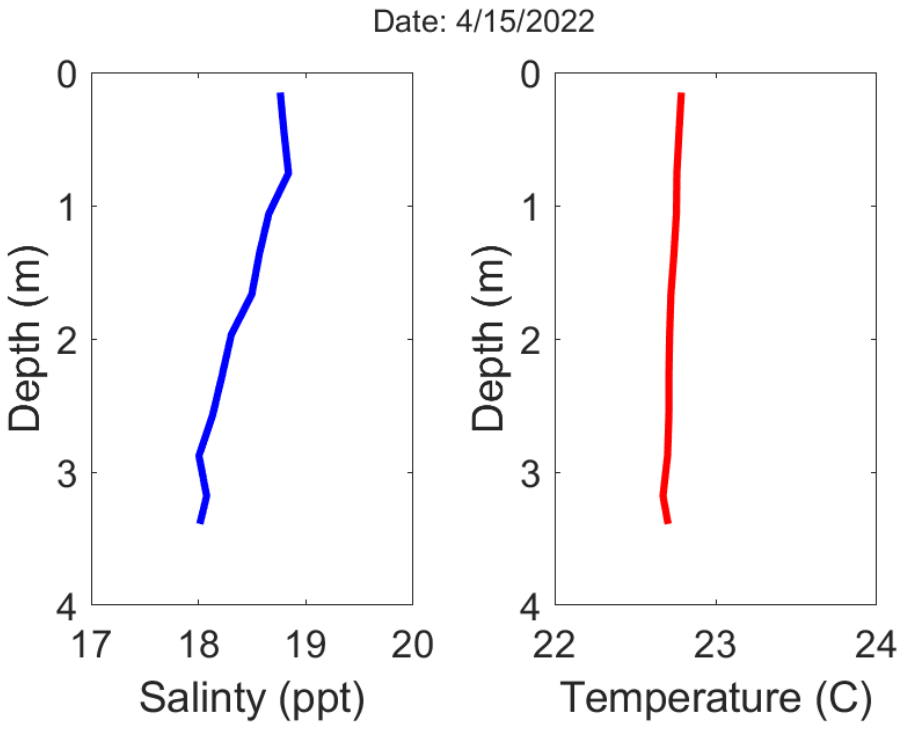

Figure D-12: Measured salinity and temperature profiles for CTD cast: 20224151426.

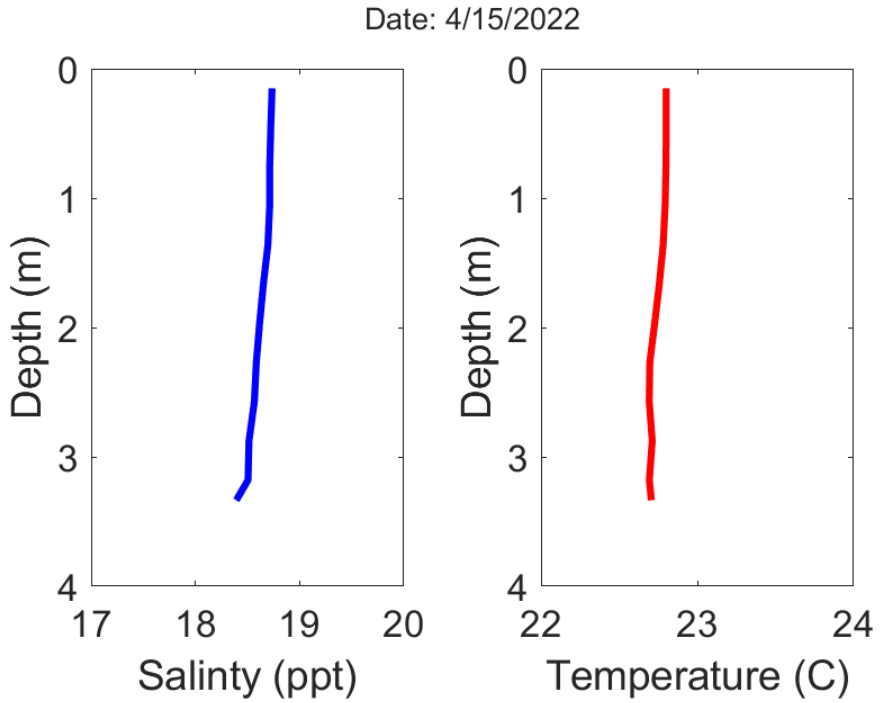

Figure D-13: Measured salinity and temperature profiles for CTD cast: 20224151428.

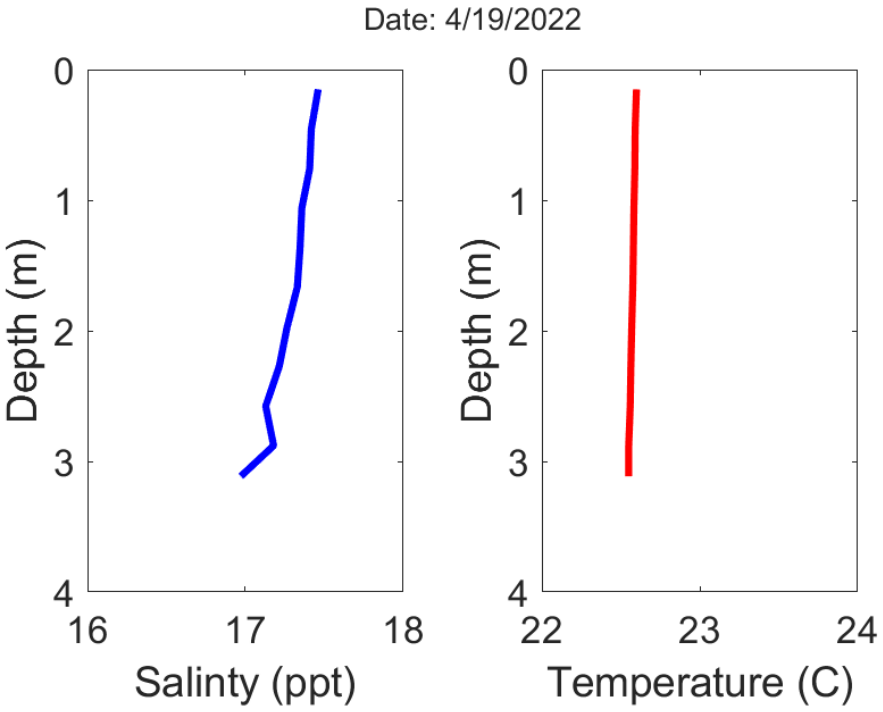

Figure D-14: Measured salinity and temperature profiles for CTD cast: 20224191212.

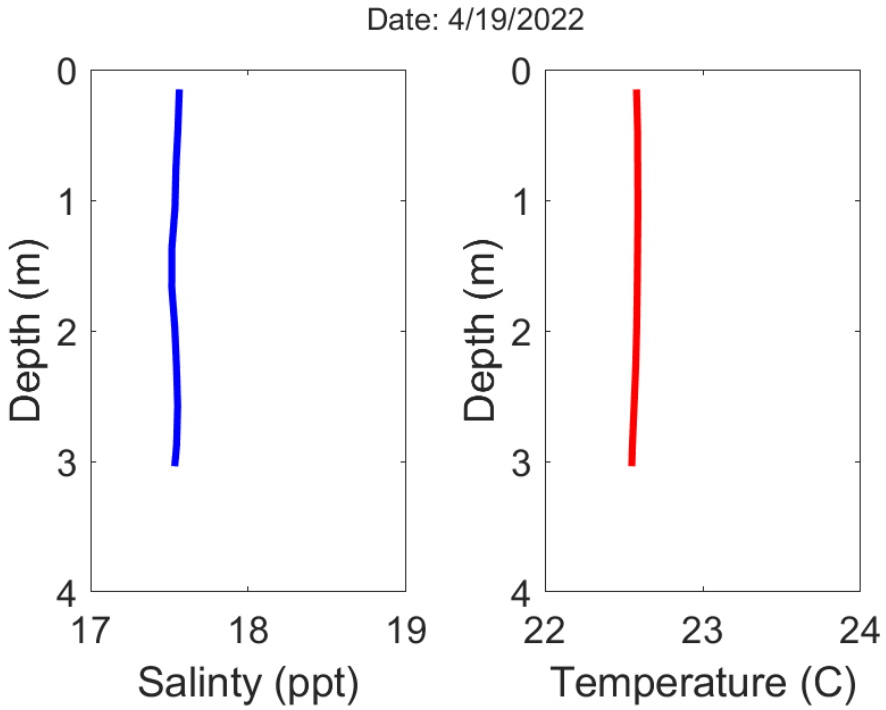

Figure D-15: Measured salinity and temperature profiles for CTD cast: 20224191216.

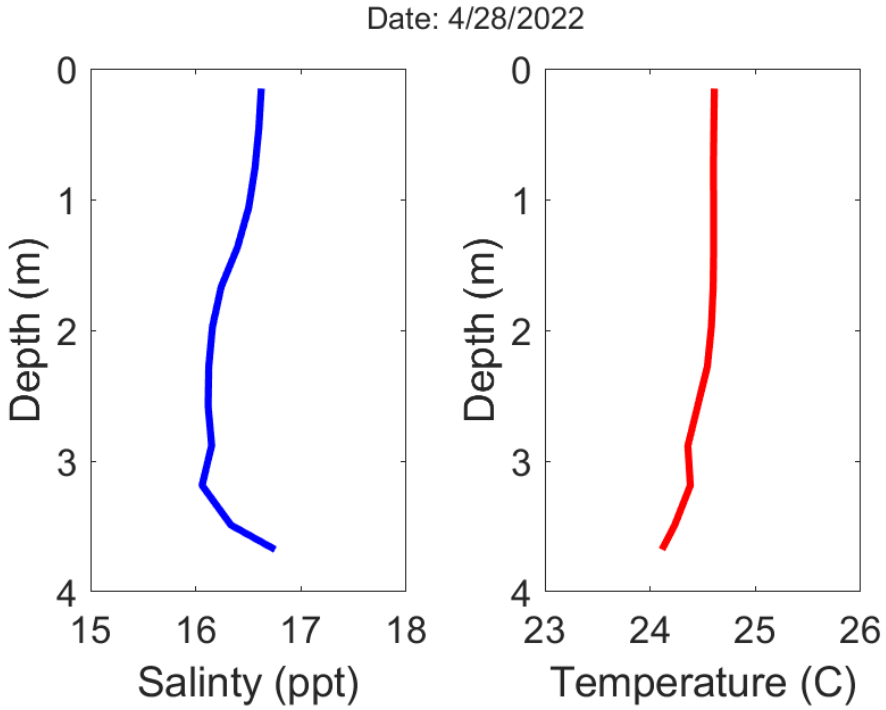

Figure D-16: Measured salinity and temperature profiles for CTD cast: 20224281218.

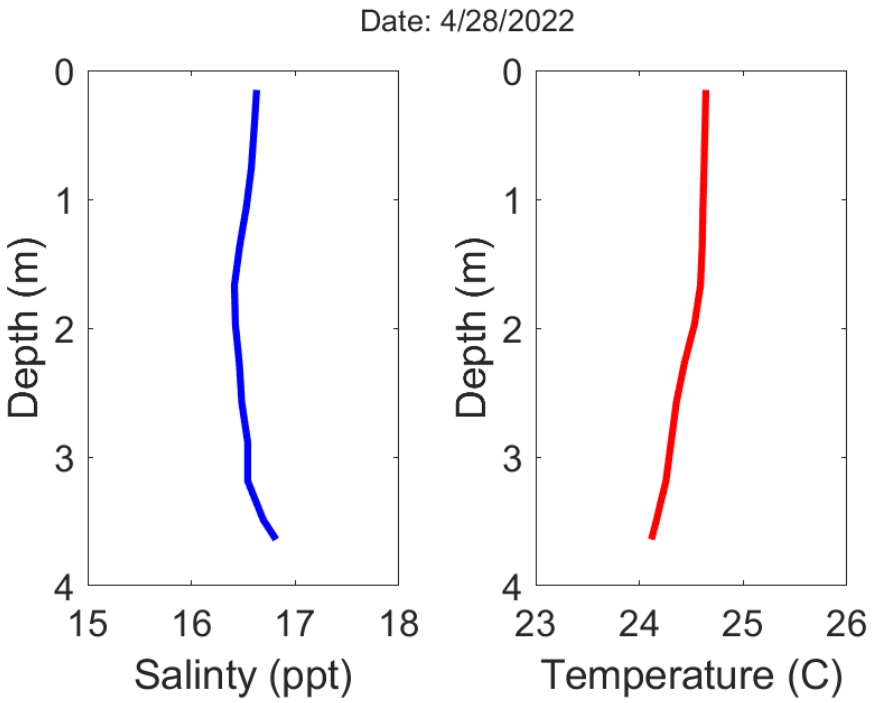

Figure D-17: Measured salinity and temperature profiles for CTD cast: 20224281219.

14 Appendix E: Hurricane Harvey Sediment

Table E-1: Changes in Hurricane Harvey sediment deposit thickness in Galveston Bay

Sampling Station Name	Latitude	Longitude	Sediment layer thickness 2017/18 (cm)	Difference in sediment layer thickness 2021 (cm)
Upper Galveston Bay				
Harv-1	29.55485	-94.966533	14.5	-2.6
Harv-C10	29.55425	-94.994967	22	-3.3
Harv-17	29.623883	-94.929383	12	0
Harv-7B	29.557	-94.924667	9	-0.4
C18	29.660383	-94.990983	14.4	-1
Trinity Bay				
Harv-C-09	29.637883	-94.804183	18.6	-2
Harv-05	29.609833	-94.830467	14.6	-5.5
Harv-7A	29.577817	-94.902633	9.1	-4.6
TB-D2	29.695883	-94.7746	20	-2
Harv 16	29.620083	-94.901333	10.4	-2.1
Harv-06	29.586867	-94.864683	6	-6
Harv-8	29.552933	-94.97495	14	-1.5
C18A	29.6604	-94.991017	14	-1
C22	29.739	-95.038083	21.5	-6.5
DB-12	29.392833°	-94.852333°	15.5	-10.5
DB-11	29.414333°	-94.854767°	16.5	-4.7
DB-10	29.435150°	-94.858483°	17	-1
DB-9	29.446667°	-94.859517°	8.4	-3
DB-8	29.457133°	-94.881867°	12.2	-1.5
DB-14	29.487167°	-94.883383°	14.5	-8.1
EB-05	29.403117°	-94.791383°	21.5	-7.7
EB-06	29.456617°	-94.812350°	13	-8.4
EB-07	29.507500°	-94.828267°	31.5	-14